Earthquake source characterization through seismic observations and numerical modeling

Thesis by
Semechah K. Y. Lui

In Partial Fulfillment of the Requirements for the
degree of
Doctor of Philosophy

Caltech

CALIFORNIA INSTITUTE OF TECHNOLOGY
Pasadena, California

2017
Defended October 26, 2016

ACKNOWLEDGEMENTS

The acknowledgments is perhaps the hardest part of this thesis, as I find it difficult to put my gratitude into words. This work would not have been possible without a lot of people.

First and foremost, my sincere gratitude goes to my research advisers, Don Helmberger and Nadia Lapusta. Don gave me a warm welcome to the world of seismology. Even until this day, I am inspired by his sharpness in generating countless research ideas and asking interesting questions. Sometimes I went into his office with several questions, and came out with even more. Nonetheless, I have learned a lot from our meetings. Don also showed tremendous support and encouragement through the ups and downs of doing research. I will truly miss our discussion time, his wittiness, and his warm smile. Nadia motivates me to strive to be a diligent researcher. She is an excellent teacher, who understands my confusion even before I can articulate it clearly, and her clarity in explaining complicated physics is something I admire. I thank her for her willingness to spend long hours discussing my research amid her busy schedule. I am always grateful for her help and advice.

I owe my special thanks to my undergraduate research adviser, Eric Hetland, who took me step by step into the world of research. I am grateful for his patience and trust in me when I started as a clueless research assistant in my sophomore year. I would not have made it to graduate school without his encouragement and guidance all along.

I also thank other members in my thesis advising committee, Jean-Paul Ampuero, Jean-Philippe Avouac, Rob Clayton, and Victor Tsai, for the time they dedicated to my thesis and its progress. Many others have been my research mentors and collaborators on various projects. I thank Zhongwen Zhan, Shengji Wei, Robert W. Graves, Xiangyan Tian, Junle Jiang, Ting Chen, and Yihe Huang for their insightful advice and discussions.

Life in the SeismoLab has been enjoyable. I am fortunate to enter Caltech in Fall 2011 with a wonderful cohort group - Asaf Inbal, Bryan Riel, Chris Rollins and Stephen Perry. The coursework in my first year would have been much harder without them. I thank Bryan and Steve especially for being great and supportive friends. We had a lot of fun working together on several SeismoLab service duties. I also thank my former and current officemates - Caitlyn Murphy, Laura Alisic,

Ting Chen, Jeff Thompson, Franklin Koch, Yiran Ma, Voonhui Lai, Jorge Castillo Castellanos and Zhichao Shen - for all the intellectual discussions, fun chats, and yummy snacks that we share, which make SM362 a friendly and productive place to work in. I would also like to extend my gratitude to the administrative staff, Donna, Priscilla, Kim, Rosemary, and Sarah, who are always caring and helpful.

Outside of school, the Chinese Bible Missions Church is my second home in Los Angeles. I thank a lot of brothers and sisters for being great role models and for adding so much color to my life here in Los Angeles. Many of them have welcomed and treated me as part of their families. I will miss our time in worship practices, fellowship programs, Bible study sessions, discipleship training, Sunday school lessons, and simply hanging out. I am grateful that God has brought us together in this journey of Faith.

I would also like to thank VaiMan & Vennis Lei, and Amy & Joseph Ho, for taking good care of me throughout my graduate studies here. Nick & Cheri Lam, and Joey Fung are wonderful friends and mentors during difficult times. I am thankful for the precious friendships that we share.

My heartfelt gratitude goes to my family - Dad, Mom, and my sister Ji - who are my anchors to help me stay grounded. I thank them for their support in my decision to study abroad and for sending their unfailing love across the Pacific over the past nine years. Ji is the best sister one could ask for and my role model in life.

Lastly, I thank Spike, my fiancé and my best friend. The past five years have not been easy when we were 2500 miles apart. Through the many ups and downs, I am forever grateful for his love, patience, understanding and forgiving heart to persevere and journey on.

ABSTRACT

In this thesis, I present a series of works on the characterization of source properties and physical mechanisms of various small to moderate earthquakes through both observational and numerical approaches. From the results, we find implications on a broader scheme of topics relating to larger earthquakes, shear zone structure, frictional properties of faults, and seismic hazard assessment.

Part I consists of two studies using waveform modeling. In Chapter 2, we present an in-depth study of a series of intraslab earthquakes that occurred in a localized region near the downdip edge of the 2011 M_w Tohoku-Oki megathrust earthquake. By refining source parameters of selected events, simulating their rupture properties and comparing their mechanisms to stress changes caused by the main shock in the region, we are able to identify the true rupture plane and the reactivation of a subducted normal fault, enhancing our understanding on the downdip shear zone. In Chapter 3, based on similar techniques, we further develop a systematic methodology to perform fast assessments on important source properties as an earthquake occurs. For two M_w 4.4 earthquakes in Fontana, moment magnitude and focal mechanism can be accurately estimated with 3 to 6 s after the first P-wave arrival, while focal depth can be constrained upon the arrival of S waves. Rupture directivity can also be determined with as little as 3 seconds of P waves. This study opens the opportunity to predict ground motions ahead of time and can potentially be useful for Earthquake Early Warning.

Part II involves the modeling of seismic source properties and physical mechanisms of interacting earthquakes in dynamic rupture simulations. In particular, we focus on small repeating earthquake sequences that trigger one another. In Chapter 4, we quantify the relative importance of physical mechanisms that contribute to earthquake interaction and identify that the stress change caused by postseismic slip is the dominating factor. Our findings introduce the possibility to constrain frictional properties of the fault based on earthquake interactions. We further apply this working model in Chapter 5 to reproduce the actual interacting repeating sequences in Parkfield. We are able to identify possible physical mechanisms that cause the inferred high stress drops of these repeating events, as well as reproduce their synchronized seismic cycles. Results from our simulations are consistent with the observed scaling relation between the recurrence time interval and the seismic moment of these events. Our findings indicate that the difference between the observed and the theoretical scaling relations can be explained by the significant aseismic slip in the rupture area.

PUBLISHED CONTENT AND CONTRIBUTIONS

Lui, Semechah KY, Don Helmberger, Shengji Wei, Yihe Huang, and Robert W Graves (2015). “Interrogation of the Megathrust Zone in the Tohoku-Oki Seismic Region by Waveform Complexity: Intraslab Earthquake Rupture and Reactivation of Subducted Normal Faults”. In: *Pure and Applied Geophysics* 172.12, pp. 3425–3437. DOI: `10.1007/s00024-015-1042-9`. URL: `http://dx.doi.org/10.1007/s00024-015-1042-9`.

Lui and Helmberger co-designed the study. Lui generated all the 1D synthetic seismograms, analyzed both the 1D and 3D velocity models, performed seismic waveform inversions and the analysis on earthquake rupture properties, and wrote the manuscript. Graves and Wei generated all the 3D synthetic seismograms. Huang contributed to calculating the regional stress change. All authors contributed to interpreting the results. Lui and Helmberger finalized the manuscript.

Lui, Semechah KY, Don Helmberger, Junjie Yu, and Shengji Wei (2016). “Rapid Assessment of Earthquake Source Characteristics”. In: *Bulletin of the Seismological Society of America* 106.6, in press. DOI: `10.1785/0120160112`. URL: `http://dx.doi.org/10.1785/0120160112`.

Lui and Helmberger co-designed the study. Lui performed all the seismic waveform inversions and directivity analysis for the targeted earthquakes in Fontana, and wrote the draft of the manuscript. Yu and Wei contributed to the preliminary studies on the earthquakes in Chino Hills and in Brawley. Both Lui and Helmberger contributed to interpreting the results and finalizing the manuscript.

Lui, Semechah KY and Nadia Lapusta (2016). “Repeating microearthquake sequences interact predominantly through postseismic slip”. In: *Nature Communications* 7, p. 13020. DOI: `10.1038/ncomms13020`. URL: `http://dx.doi.org/10.1038/ncomms13020`.

Lui and Lapusta co-designed the study. Lui performed the numerical simulations, analyzed the results, produced Figures, and wrote the draft of the manuscript. Both Lui and Lapusta contributed to interpreting the results and finalizing the manuscript.

TABLE OF CONTENTS

Acknowledgements iii
Abstract v
Published Content and Contributions vii
Table of Contents viii
List of Illustrations x
List of Tables xiii
Nomenclature xiv
Chapter I: Introduction 1
  1.1 Earthquake characterizations through seismic observations 2
  1.2 Numerical simulations of earthquake physics 3
  1.3 References 4
Chapter II: Interrogation of the megathrust zone in the Tohoku-Oki seismic region by waveform complexity: intraslab earthquake rupture and reactivation of subducted normal faults 6
Abstract 7
  2.1 Introduction 8
    2.1.1 Background: Complexity of the Tohoku-Oki Seismic Region 8
    2.1.2 Overview of Our Study 10
  2.2 Methods and Results 11
    2.2.1 Validity of 1D Seismic Velocity Models 11
    2.2.2 Source Mechanism and Rupture Characteristics of Selected Intraslab Events 14
    2.2.3 Intraslab Thrust Events and Stress Change from the Mw 9.1 Main Shock 19
  2.3 Discussion 20
  2.4 Conclusion 22
  2.5 Appendix A: Generating Empirical Green's Functions 24
  2.6 Appendix B: Supplementary Information 25
  2.7 References 34
Chapter III: Rapid Assessment of Earthquake Source Characteristics 37
Abstract 38
  3.1 Introduction 39
    3.1.1 Small earthquakes as useful resources 39
    3.1.2 Data from earthquakes near Fontana, CA as a test case . . . 40
  3.2 Methodology 42
  3.3 Analysis and Results 44
    3.3.1 Real-time assessment of source parameters 44
    3.3.2 Assessing rupture properties 46
  3.4 Discussion 48

3.4.1 Predicting the effect of directivity at farther stations 49
3.4.2 Implications for earthquake early warning and Shake Map . 50
3.4.3 Impact of large earthquakes 51
3.5 Conclusion 53
3.6 Appendix A: Supplementary Information 54
3.7 References 62
Chapter IV: Repeating microearthquake sequences interact predominantly through postseismic slip 64
Abstract 65
4.1 Introduction 66
4.2 Results 67
4.2.1 Simulations of repeating earthquake sequences 67
4.2.2 Strong earthquake interaction 67
4.2.3 Dominance of postseismic stress change 69
4.3 Discussion 70
4.4 Appendix A: The Rate-and-State Fault Model 78
4.5 Appendix B: Supplementary Information 80
4.6 References 90
Chapter V: Modeling the high stress drops and the interactions of the repeating microearthquakes in Parkfield 94
Abstract 95
5.1 Repeating earthquake sequences in Parkfield 96
5.2 Methodology: Modeling the San Francisco and Los Angeles repeaters 99
5.2.1 Fault frictional resistance 99
5.2.2 Choosing VW patch sizes and characteristic slip values . . . 102
5.2.3 Reproducing higher source stress drops 102
Model 1: Enhanced coseismic weakening 103
Model 2: Elevated normal stress on the VW patch 104
5.3 Simulations with a single VW patch 105
5.3.1 Model M1 with TP 105
5.3.2 Model M2 with ENS 107
5.3.3 Model M3 with both ENS and TP 107
5.3.4 Variability due to aseismic slip and smaller seismic events . 108
5.3.5 Scaling relation between T_r and M_o 113
5.4 Simulations with two velocity-weakening patches 115
5.4.1 Effect of interactions among VW patches 116
5.4.2 Effect of frictional properties of the creeping segment 121
5.5 Conclusion 125
5.6 References 130
Chapter VI: Conclusion 137
6.1 Summary 137
6.2 Outlook 138
6.2.1 Implications on earthquake scaling 138
6.2.2 Spatiotemporal heterogeneity of fault properties 139

LIST OF ILLUSTRATIONS

Number *Page*

2.1 Overview of the study region. 9
2.2 Earthquakes at the downdip edge of the Tohoku-Oki rupture region. . 10
2.3 Comparison between 1D and 3D synthetic waveforms of event E1. . . 13
2.4 Timing shift and cross-correlation between data and 1D synthetics waveform. 14
2.5 Synthetic waveform comparison of event E1 generated from two different 3D velocity models. 15
2.6 Comparison of focal mechanisms from CAP inversion. 16
2.7 Rupture directivity as shown from waveform data. 17
2.8 Modeling rupture directivity using the empirical Green's function approach. 18
2.9 Stress change in the ruptured region due to the M_w 9.1 mainshock. . . 20
2.10 Comparison of the difference in time shift values of E1 and E2 assuming different epicentral locations. 22
2.B1 Waveform inversion with frequency bands up to 0.05 Hz. 25
2.B2 Waveform inversion with frequency bands up to 0.1 Hz. 26
2.B3 Waveform inversion with frequency bands up to 0.25 Hz. 27
2.B4 Waveform inversion with frequency bands up to 1 Hz. 28
2.B5 Detailed analysis result of CAP inversion. 29
2.B6 Comparison of E1 broadband displacement data and EGFs at two of the nearest stations HRO and KSN. (vertical and tangential components respectively) 30
2.B7 Comparison of E1 broadband velocity data and EGFs at two of the nearest stations HRO and KSN (tangential and vertical components respectively). 31
2.B8 Final slip and static stress drop of the main event. 32
3.1 Overview of the study region of this project near the city of Fontana located near the San Andreas Fault. 40
3.2 Preliminary test on the 2012 Brawley event. 41
3.3 Significant difference in energy content for earthquakes at different focal depths. 42

3.4 Stations near the epicenters are selected for rapid assessment of source parameters. 45
3.5 CAP allows accurate and fast characterization of moment magnitude, focal mechanism and depth. 46
3.6 Directivity observed from difference in amplitude ratio of waveform across all azimuths. 47
3.7 Predicting rupture directivity using incoming P-wave. 48
3.8 Sensitivity test of waveform at different frequency bands. 49
3.9 We can predict the amplitude of S-wave arrivals based on the P-wave directivity analysis. 50
3.10 Simulating Green's functions of larger earthquakes using the EGF approach. 52
3.A1 Preliminary study on the 2008 Chino Hills earthquake. 54
3.A2 Waveform recorded at stations within the LA Basin. 55
3.A3 The study on the Inglewood M_w 4.6 earthquake by Luo et al (2010). . 56
3.A4 Waveform inversion of the two events using the whole network. . . . 57
3.A5 Small event can be used as EGFs for studying directivity. 58
3.A6 Detailed results of the directivity analysis with 3 s of incoming P wave. 59
3.A7 Validating the ground-motion prediction test with the EGF approach. 60
3.A8 Rayleigh wave prediction for the same four stations. 61
4.1 Interaction of two repeating earthquake sequences in a rate-and-state fault model. 74
4.2 Exploring the extent of interaction. 75
4.3 Different types of stress changes induced on the triggered VW patch. 76
4.4 Effect of the VS region on the interaction. 77
4.B1 Cumulative slip along the fault through time. 80
4.B2 Selecting initial conditions for simulations that allow us to quantify the potential interaction between the repeating sequences. 81
4.B3 Example of initial conditions on the fault. 82
4.B4 Comparison of the single-patch and two-patch simulations 83
4.B5 Interaction of two VW patches - Case 1. 84
4.B6 Interaction of two VW patches - Case 2. 85
4.B7 Behavior of postseismic creep on faults with different velocity-strengthening friction properties $(a-b)_\mathrm{VS}$. 86
4.B8 Comparing the extent of interaction ζ as defined in the main text for VW patches with different initial condition. 86

4.B9 Similar to Figure 4.B8, with a different definition of ζ 87
4.B10 Interaction of two VW patches - Case 3. 88
5.1 Repeating earthquake sequences on the portion of the Parkfield segment of the San Andreas Fault. 97
5.2 Fault properties in M1 and M2. 104
5.3 Simulation results for (a) M1-b, (b) M2-b, and (c) M2-d with $(a-b)_{\mathrm{VS}}$ = 0.008. 106
5.4 comparison of the ratio of seismic to aseismic slip in different recurrence periods in M1-b. 109
5.5 Effect of interseismic events on the repeating sequence in M2-b. . . . 110
5.6 comparison of the ratio of seismic to aseismic slip in different recurrence periods in M2-b. 112
5.7 Comparison of the average shear stress on the VW patch in M1 and M2 113
5.8 T_{r} vs M_{o} for the repeating events in M1, M2, and M3. 114
5.9 Example of model set up for simulating the SF and LA repeating sequences. 116
5.10 Example of the interaction between the SF and LA events, from M1-double with $(a-b)_{\mathrm{VS}}$ = 0.004. 117
5.11 Interactions between the SF and LA patch in models M1-double and M2-double, with $(a-b)_{\mathrm{VS}}$ = 0.004. 119
5.12 Comparison of the interaction among VW regions between single-patch and double-patch cases. 120
5.13 Source properties of the repeaters in models with a larger extent of spatial heterogeneity. 121
5.14 Another example illustrating the effect of spatial heterogeneity on faults. 122
5.15 Dependence of the postseismic creep on the frictional properties of the VS region. 123
5.16 Suppression of the postseismic creep on a strongly velocity-strengthening segment with $(a-b)_{\mathrm{VS}}$ = 0.032. 124
5.17 Frictional properties of the creeping segment significantly affect the source properties of the repeaters. 125
5.18 Frictional properties of the creeping region affect the average stress drop of the repeating sources. 126

LIST OF TABLES

Number *Page*
2.B1 1D crustal model for the Tohoku-Oki region studied. 32
2.B2 Result of directivity simulations based on displacement data 33
2.B3 Result of directivity simulations based on velocity data 33
3.A1 1D crustal model for the Southern California region studied 61
4.A1 Parameters of Our Simulations 79
4.B1 Summary of the eventual event pattern for a range of VW patch sizes d and initial conditions. 89
5.1 Fault model parameters used for all simulations 101
5.2 Hydrothermal properties of the VW patch in M1 104
5.3 Fault parameters used in M1 and M2 and properties of the reproduced seismic sources. 106
5.4 Comparison between the repeating sequences reproduced in M2-e and M3. 108
5.5 Source properties of the main repeating events in models M1-double and M2-double. 118

NOMENCLATURE

Directivity. Direction of rupture on a fault during an earthquake.

Fault strength. The ability of a fault to withstand an applied shear stress.

Focal mechanism. Fault-plane solution describing the deformation in the source region that generates the resulting seismic waves.

Moderate earthquake. $5 \leq M_\mathrm{w} \leq 7$.

Pnl waves. The entire wavetrain between P and S waves.

Rise time. Local duration of slip during an earthquake.

Slip. The relative displacement at a given position on the fault.

Small earthquake. $M_\mathrm{w} \leq 5$.

Stress drop. The difference in shear stress on a ruptured fault before and after an earthquake.

Chapter 1

INTRODUCTION

The earliest earthquakes with descriptive information can be traced back to over 3000 years ago. Throughout history, the Earth has demonstrated its dynamic nature. Numerous records of damages caused by the intense shaking can be found in the literature, with events spanning a wide range of magnitudes (M_{w}) and occurring in different tectonic settings and at unpredictable times. In the ancient days, people relied on creative stories to explain the sudden movements of the Earth's crust, including a giant twitchy catfish named Namazu in Japan, and the angry Poseidon, the god of the sea in Greece. The true natural cause of earthquakes has long been a mystery until the 18^{th} century.

In modern days, technological advancement has allowed seismologists high-resolution seismic wave observation by broadband seismometers, increasing our scientific understanding of earthquake processes. Nonetheless, due to the complexity of seismic sources, as well as their intricate interplay with the Earth's heterogeneous structure, scientists are continuously surprised by what happens in nature. For example, the largest seismic slip of the Tohoku-Oki M_{w} 9.1 megathrust earthquake actually occurred close to the trench where stable creeping was expected (Ide et al., 2011; Loveless and Meade, 2010; Simons et al., 2011; Wei et al., 2012). Also, the reason behind the absence of great historic earthquakes on the southern San Andreas Fault in California remains uncertain (Fialko, 2006). These examples point to the fact that earthquake physics is still a tough nut to crack.

Ultimately, the goal is to better understand the seismic hazard and physics of larger destructive events in order to develop a physics-based hazard assessment and to alleviate damage and loss from earthquakes. To that end, continuous effort in developing accurate characterizations of mega-earthquakes and the physics behind them is essential. However, their infrequent occurrence and uniqueness in rupture complexity can also be barriers to a thorough understanding of the phenomena. On the other hand, smaller earthquakes occur much more frequently and provide a large pool of data to help shed light on the broader scheme of studying earthquakes and the structure of the Earth. For example, what can we learn from smaller earthquakes about local structures and stress state? For earthquake early warning, how much can we characterize about an earthquake as it happens, and how fast can we do it? Can smaller earthquakes help us constrain the maximum size of earthquakes that can potentially happen in a seismogenic zone? Can one predict the source behavior of future large earthquakes by studying small events in the region? Can small earthquakes tell us the controlling factors for slip and rupture on a fault?

The focus of this thesis is on various observations of small to moderate earthquakes in subduction zones and on transform faults, with moment magnitude (M_w) between 1.5 and 6.5. Due to generally insufficient seismic data resolution and azimuthal coverage, it has been challenging to characterize smaller earthquake sources, and so they are usually regarded as simple radially symmetric rupture at a constant rupture velocity (Brune, 1970; Eshelby, 1957; Madariaga, 1976). In contrast, the ruptures of larger earthquakes ruptures are found to be more complex, often propagate in a unilateral fashion (Henry and Das, 2001; Mai et al., 2005; McGuire et al., 2002). In the past, however, a limited number of studies have shown that small events do have more complicated source processes than typically assumed (Boatwright, 2007; Domański et al., 2002). Fortunately, the rapid densification of regional and global seismic networks and the advancement of computational resources in recent years enable integrated approaches to study the physics of earthquakes, as well as making detailed analysis of small earthquakes possible. On one hand, high-resolution waveform modeling allows in-depth understanding of the kinematics of source processes. On the other, recently developed dynamic rupture simulations consider the effect of seismic wave interactions and are capable of producing realistic rupture behavior that can be compared to observations, providing insights into the fundamental physics that drives what we see on real faults. Furthermore, numerical modeling also bridges the gap between tiny laboratory earthquakes and megaearthquakes ($M_\mathrm{w} > 9$) in nature.

In the following chapters, we present a series of studies that exemplify the utilization of (I) observational and (II) numerical approaches to characterize small to moderate earthquake sources in various tectonic settings and their driving physics. We aim to determine from the wealth of data what smaller earthquakes can tell us about tectonics and larger earthquakes.

1.1 Earthquake characterizations through seismic observations

Part I of this thesis investigates earthquake characterization through an observational approach. We demonstrate in two case studies in systematic ways to model seismic waves in order to accurately and efficiently constrain the source and rupture properties.

Chapter 2 illustrates how source properties can be useful in delineating local crustal structures and verifying the state of stress in the region. Here we focus on a group of moderate earthquakes (M_w 4.5 to 6.5) that occurred after the 2011 M_w 9.1 Tohoku-Oki megathrust event on the downdip edge of the ruptured area. Using broadband waveform modeling, we refine their source parameters, including their focal mechanisms, focal depths, and rupture properties, such as direction and dimension. We discover that these events align in a narrow strip inside the subducting slab, which is potentially the result of the reactivation of a subducted normal fault. Through resolving the rupture properties of these intraslab earthquakes, the orientation of this fault can be determined. Furthermore, focal mechanisms of these events are also shown to have a causal relationship with the stress change caused by the mainshock. This study highlights the importance of precise source properties in uncovering the features and evolution of the background tectonic region.

In Chapter 3, we investigate the potential of rapid and accurate source characterization and its implications in the field of Earthquake Early Warning (EEW). The tectonic setting here changes from a subduction zone to a mature transform fault system. With several small events (M_w 3-4.5) in Fontana, California, we introduce a methodology in which source and rupture properties can be constrained within as little as 3 seconds of the arriving seismic waves, which provides valuable information for the prediction of the associated ground motion in broader regions from the epicenter. We also demonstrate how one can effectively calculate the potential ground motion of a larger event using past events in the same location via empirical Green's functions. This study highlights the importance of establishing efficient source characterization for hazard assessment and response.

1.2 Numerical simulations of earthquake physics

Motivated by intriguing observations, in Part II, we use dynamic fault simulations to study seismic sources and their supporting physics, with a particular focus on earthquakes that interact with one another. To this end, we explore the cause of earthquake triggering, based on a dynamic rupture model governed by rate-and-state friction laws.

In Chapter 4, our model consists of two repeating earthquake sequences embedded in a creeping fault, and we quantitatively compare several types of stress transfer that occur between the repeating events. One major finding is that postseismic creep dominates the interaction in the models. Because of this, earthquake triggering in our model also occurs at distances much larger than typically assumed. Since the behavior of postseismic creep depends heavily on the frictional properties of the fault on which it propagates, these findings further emphasize the importance of source characterization in constraining properties of creeping segments.

Lastly, in Chapter 5, we integrate results from Chapter 4 with field observations by applying the fault model to reproducing the interacting microearthquakes found on the Parkfield creeping segment of the San Andreas Fault. Apart from the unique interacting seismic pattern in previous studies, these repeaters are also characterized by anomalous source properties, such as high stress drops on the order of 30 to 60 MPa. We show that dynamic rupture simulations are able to provide an explanation for the phenomena. The high stress drops can be reproduced in a rate-and-state fault model when additional factors are present on the velocity-Weakening patches; two possibilities are thermal pressurization of pore fluids and locally elevated normal stress. Our results show that the variability of the source properties and the interactions of these repeaters, as well as their observed scaling between recurrence time T_{r} and seismic moment M_{o}, are due to the occurrence of substantial aseismic slip on the velocity-weakening patches. We also discuss the effect of frictional properties of the creeping region on both the behavior of postseismic slip and the source properties of these repeaters.

Chapters 2 to 4 of this thesis are published in peer-reviewed journals, while Chapter 5 will be submitted for publication with additional modeling results.

1.3 References

Boatwright, John (2007). "The persistence of directivity in small earthquakes". In: *Bulletin of the Seismological Society of America* 97.6, pp. 1850–1861. DOI: `10.1785/0120050228`. URL: `http://dx.doi.org/10.1785/0120050228`.

Brune, James N. (1970). "Tectonic stress and the spectra of seismic shear waves from earthquakes". In: *Journal of Geophysical Research* 75.26, pp. 4997–5009. ISSN: 2156-2202. DOI: `10.1029/JB075i026p04997`. URL: `http://dx.doi.org/10.1029/JB075i026p04997`.

Domański, B, SJ Gibowicz, and P Wiejacz (2002). "Source time function of seismic events at Rudna copper mine, Poland". In: *The Mechanism of Induced Seismicity*. Springer, pp. 131–144. DOI: `10.1007/PL00001247`. URL: `http://dx.doi.org/10.1007/PL00001247`.

Eshelby, John D (1957). “The determination of the elastic field of an ellipsoidal inclusion, and related problems”. In: *Proceedings of the Royal Society of London A: Mathematical, Physical and Engineering Sciences*. Vol. 241. 1226. The Royal Society, pp. 376–396. DOI: `10.1098/rspa.1957.0133`. URL: `http://dx.doi.org/10.1098/rspa.1957.0133`.

Fialko, Yuri (2006). “Interseismic strain accumulation and the earthquake potential on the southern San Andreas fault system”. In: *Nature* 441.7096, pp. 968–971. DOI: `10.1038/nature04797`. URL: `http://dx.doi.org/10.1038/nature04797`.

Henry, C and S Das (2001). “Aftershock zones of large shallow earthquakes: fault dimensions, aftershock area expansion and scaling relations”. In: *Geophysical Journal International* 147.2, pp. 272–293. DOI: `10.1046/j.1365-246X.2001.00522.x`. URL: `http://dx.doi.org/10.1046/j.1365-246X.2001.00522.x`.

Ide, Satoshi, Annemarie Baltay, and Gregory C Beroza (2011). “Shallow dynamic overshoot and energetic deep rupture in the 2011 Mw 9.0 Tohoku-Oki earthquake”. In: *Science* 332.6036, pp. 1426–1429. DOI: `10.1126/science.1207020`. URL: `http://dx.doi.org/10.1126/science.1207020`.

Loveless, John P. and Brendan J. Meade (2010). “Geodetic imaging of plate motions, slip rates, and partitioning of deformation in Japan”. In: *Journal of Geophysical Research: Solid Earth* 115.B2. B02410, n/a–n/a. ISSN: 2156-2202. DOI: `10.1029/2008JB006248`. URL: `http://dx.doi.org/10.1029/2008JB006248`.

Madariaga, Raul (1976). “Dynamics of an expanding circular fault”. In: *Bulletin of the Seismological Society of America* 66.3, pp. 639–666.

Mai, P Martin, P Spudich, and J Boatwright (2005). “Hypocenter locations in finite-source rupture models”. In: *Bulletin of the Seismological Society of America* 95.3, pp. 965–980. DOI: `10.1785/0120040111`. URL: `http://dx.doi.org/10.1785/0120040111`.

McGuire, Jeffrey J, Li Zhao, and Thomas H Jordan (2002). “Predominance of unilateral rupture for a global catalog of large earthquakes”. In: *Bulletin of the Seismological Society of America* 92.8, pp. 3309–3317. DOI: `10.1785/0120010293`. URL: `http://dx.doi.org/10.1785/0120010293`.

Simons, Mark et al. (2011). “The 2011 magnitude 9.0 Tohoku-Oki earthquake: Mosaicking the megathrust from seconds to centuries”. In: *science* 332.6036, pp. 1421–1425. DOI: `10.1126/science.1206731`. URL: `http://dx.doi.org/10.1126/science.1206731`.

Wei, Shengji, Robert Graves, Don Helmberger, Jean-Philippe Avouac, and Junle Jiang (2012). “Sources of shaking and flooding during the Tohoku-Oki earthquake: A mixture of rupture styles”. In: *Earth and Planetary Science Letters* 333, pp. 91–100. DOI: `10.1016/j.epsl.2012.04.006`. URL: `http://dx.doi.org/10.1016/j.epsl.2012.04.006`.

Chapter 2

INTERROGATION OF THE MEGATHRUST ZONE IN THE TOHOKU-OKI SEISMIC REGION BY WAVEFORM COMPLEXITY: INTRASLAB EARTHQUAKE RUPTURE AND REACTIVATION OF SUBDUCTED NORMAL FAULTS

Lui, Semechah KY, Don Helmberger, Shengji Wei, Yihe Huang, and Robert W Graves (2015). "Interrogation of the Megathrust Zone in the Tohoku-Oki Seismic Region by Waveform Complexity: Intraslab Earthquake Rupture and Reactivation of Subducted Normal Faults". In: *Pure and Applied Geophysics* 172.12, pp. 3425–3437. DOI: `10.1007/s00024-015-1042-9`. URL: `http://dx.doi.org/10.1007/s00024-015-1042-9`.

ABSTRACT

Results from the 2011 M_w 9.1 Tohoku-Oki megathrust earthquake display a complex rupture pattern, with most of the high-frequency energy radiated from the downdip edge of the seismogenic zone and very little from the large shallow rupture. Current seismic results of smaller earthquakes in this region are confusing due to disagreements among event catalogs on both the event locations ($>$ 30 km horizontally) and mechanisms. Here we present an in-depth study of a series of intraslab earthquakes that occurred in a localized region near the downdip edge of the main shock. We explore the validity of a 1D velocity model and refine earthquake source parameters for selected key events by performing broadband waveform modeling combining regional networks. These refined source parameters are then used to calibrate paths and further simulate secondary source properties, such as rupture directivity and fault dimension. Calculation of stress changes caused by the main event indicate that the region where these intraslab events occurred are prone to thrust events. This group of intraslab earthquakes suggest the reactivation of a subducted normal fault, and are potentially useful in enhancing our understanding on the downdip shear zone and large outer-rise events.

2.1 Introduction

2.1.1 Background: Complexity of the Tohoku-Oki Seismic Region

The M_w 9.1 Tohoku-Oki earthquake in 2011 devastated the Northeast coastline of Japan. Analysis of various data sets (i.e. regional and teleseismic broadband seismographic net- works, geodetic networks, ocean-bottom measurements, etc.) demonstrates a unique and complex rupture pattern which indicates varying mechanical and frictional properties along the thrust zone (Fujiwara et al., 2011; Ide et al., 2011; Ito et al., 2011; Simons et al., 2011; Wei et al., 2012; Yue and Lay, 2011). Especially intriguing is the difference of frequency content in radiated energy emanating from various parts of the rupture zone. Huang et al., (2012) show that the high-frequency radiations in the deeper part are at least partially caused by asperities that have hosted earthquakes before, but the exact mechanism that has caused the variation of such energy concentration is currently unclear. Since the mainshock, the region has also experienced a sharp increase in seismic aftershock activity. These seismic events span a wide range in size and depth. Current national and international earthquake catalogs rely mainly on travel-time data to determine origin time and spatial location. Unfortunately, their results often do not agree, where the hypocentral locations of earthquakes reported by different networks can vary by over 20 km laterally, and by over 10 km vertically depending on the catalog (Zhan et al., 2012). Furthermore, due to the lack of regional stations on the Pacific side, the resolution decreases with distance from the Japan coast. Such discrepancy creates difficulty in constructing a coherent picture of the thrust zone.

Among the numerous aftershocks, there are a number of earthquakes that occurred along the downdip region of the rupture zone (Figure 2.1). Long-period source inversions by the National Research Institute for Earth Science and Disaster Prevention (NIED) placed them at a depth greater than 40 km. According to the slab models used in the JMA catalog and proposed by Zhan et al., (2012), such focal depths place these seismic events below the slab interface. Despite varying magnitudes, their focal mechanisms , as well as their arriving SV and SH pulses, are similar to one another (Figure 2.2). In an earlier study by Kato and Igarashi, (2012), a group of downdip compressional earthquakes localized off the coast of Miyagi, Iwate, and Fukushima is also delineated, and is generally believed to be an outcome of the static stress increase generated by abrupt slip termination during the main shock (Lin and Stein, 2004). The source mechanism and rupture characteristics of these intraslab events are of interest because they occurred beneath the megathrust interface where an interesting energy radiation pattern was observed during the mainshock. Within

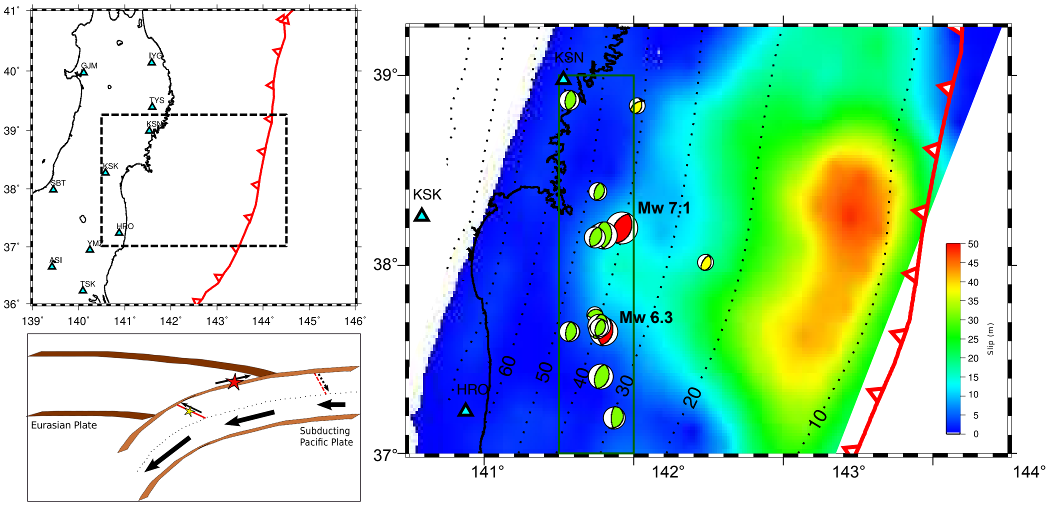

Figure 2.1: *Overview of the study region.* (Top left) Map of the Tohoku-Oki region. Dashed rectangular box is the area of the map shown on the right. (Right) Seismic events in the region 141.5 to 142E and 37 to 39N. Focal mechanisms marked in red represent the M_{w} 7.1 aftershock and E1 (2011/08/19, M_{w} 6.3) analyzed in this study. FM marked in green are other seismic events with similar strike, dip and hypocenter depth to the two larger events. FM in yellow are similar events found outside of the rectangular region. Triangles in cyan are the three closest F-net stations to E1. The color scale represents the slip distribution of the M_{w} 9.1 main shock in 2011 (Wei et. al., 2012). Dotted lines are the slab contours. (Bottom left) Schematic diagram illustrating the formation of normal fault in the outer rise region which later undergoes subduction and reactivation after the M_{w} 9.1 Tohoku-Oki event.

this group of intraslab earthquakes, the largest is a M_{w} 7.1 aftershock that occurred on April 7, 2011, a month after the M_{w} 9.1 earthquake. Based on detailed seismic tomographic estimation of the 3D velocity structure, Nakajima et al., (2011) identified a low-velocity zone in the focal zone of this aftershock. Therefore, this event was hypothesized as a possible reactivation of a buried hydrated normal fault that was formed in the outer-rise region prior to subduction (Figure 2.1 inset). Ohta et al., (2011) also proposed a coseismic displacement model for the same aftershock using regional high-rate GPS data. With a non-linear inversion approach, they estimated a rectangular fault with uniform slip. Even though the results indicated intraslab earthquake characteristics, it was difficult to identify the true rupture plane because the displacement at each GPS site shows similar pattern on the land for both nodal planes. Based on the southward dipping alignment of the aftershock pattern, both Nakajima et al., (2011) and Ohta et al., (2011) considered this event to have occurred on the east-dipping fault plane.

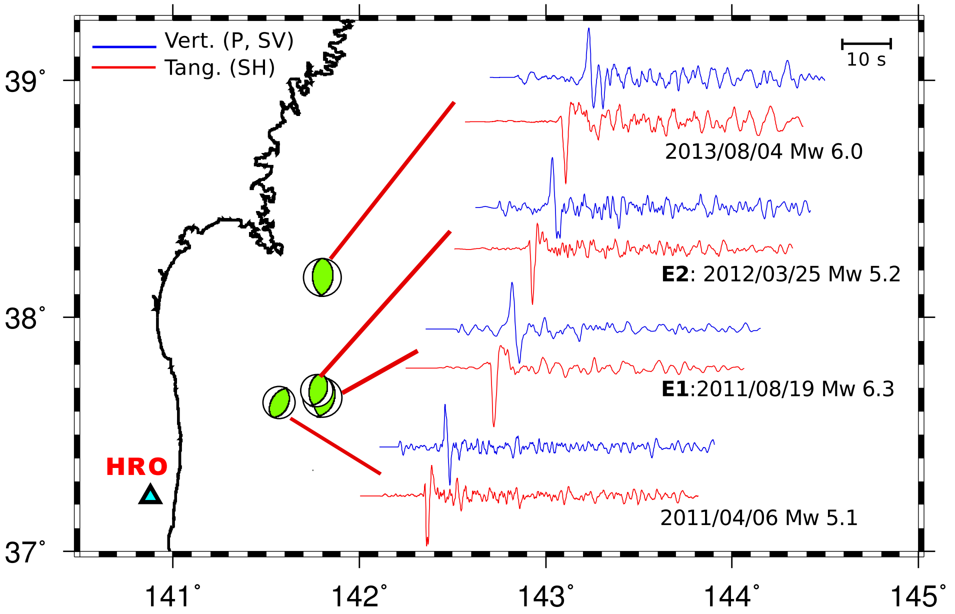

Figure 2.2: *Earthquakes at the downdip edge of the Tohoku-Oki rupture region.* These seismic events have displayed very similar focal mechanism and waveform complexity. Waveform (in velocity) shown here are examples recorded by the F-net station HRO: (blue) vertical component showing the behavior of P and SV phases,(red) tangential component showing the behavior of SH phase. Note the similarity in recording from events labeled E2 and E1.

These intriguing observations, as well as the lack of a comprehensive understanding of these intraslab events, have prompted us to investigate this group of earthquakes. In particular, we explore the scope of details that we can extract from existing data, and, by modeling these intraslab events, we test the hypothesis of weakened zones present inside the slab. We also study their correlation with shear stress change in the region caused by the mainshock.

2.1.2 Overview of Our Study

In order to study the structure of the shear zone and to resolve the source properties of these earthquake in local scale, it requires the analysis of broadband data recorded by regional seismic stations. Therefore we first focus on the validation of seismic velocity models. In particular, we evaluate how well a simplified 1D velocity model can represent the heterogeneous 3D Earth. Based on another aftershock in the downdip region with well-determined source parameters, such detailed comparison allows us to establish which station paths are 1D-like. With validated velocity models for these selected stations, we then explore the possibility of modeling the rupture characteristics of intraslab events, particularly in order to identify the true rupture plane. This section focuses on two intraslab earthquakes within the group, one of which, occurred on August 19, 2011 with M_w 6.3 (named E1, Figure 2.2), while the other occurred seven months later on March 25, 2012 with M_w 5.2 (named E2). According to the JMA catalog, these two earthquakes have almost identical hypocenters, with a lateral separation of less than 4 km and a 1.8-km difference in depth. Their seismic waveform data also have very similar shapes and frequency content as displayed in Figure 2.2. Thus, there is strong evidence indicating that the two earthquakes have occurred at almost the same hypocenter location with similar focal mechanism, but with a difference in moment magnitude. Looking closely at both sets of data, we discover suggestive features of E1 rupturing unilaterally. To verify our hypothesis, E2 is used as the empirical Green?s functions to simulate E1 (Hartzell, 1978). Using Taylor-series expansion in time domain, E1 is modeled as the summation of a line of point sources (Song and Helmberger, 1996). This search procedure allows the determination of the focal plane on which the earthquake occurred, and gives a robust estimation of fault finiteness. These results, together with the other intraslab events in the region with similar mechanisms, suggests a line of weakness at least 150 km long, which is consistent with the estimation in an earlier study by Kato and Igarashi, (2012).

As an extension from our modeling result, in the last part of the paper, we address the effect of shear stress change caused by the mainshock. While previous studies focus mostly on the shear stress change in the regional scale (Kato et al., 2011; Toda et al., 2011), we study locally the area beneath the downdip edge of the main shock rupture region in order to verify the causal relationship between these intraslab events and the megathrust. Without assuming specific fault geometries or friction coefficients, we evaluate faulting mechanisms that are possible in this location.

2.2 Methods and Results

2.2.1 Validity of 1D Seismic Velocity Models

In general, the Earth at teleseismic distances is assumed to be a 1D layered structure, which has velocity varying with depth and does not contain any subducted slab structures, though in reality it is far more complex. In particular, the Japan region involves a complicated tectonic setting, with several tectonic plates, as well as multiple sedimentary basins on land and offshore. With the accessibility to the enormous data set from several major regional seismic networks in Japan, we possess ample resources to characterize waveforms that provide information on earthquake source parameters and rupture properties. Since our emphasis is the detail of the intraslab events in a localized megathrust zone, we begin with testing the validity of 1D velocity model (Table 2.B1) by comparing data with 1D and 3D waveform synthetics respectively. In this particular study region, we focus on regional data collected from seismic networks in Japan (F-net, K-net and Kik-net), with most stations within 500 km from the earthquake sources. Here the 3D Japan Integrated Velocity Structure Model (JIVSM; Koketsu et al., 2008) is used, which includes a slab structure. We apply the staggered-grid finite difference technique to model 3D wave propagation (Graves, 1996), with a grid spacing of 0.4 km and synthetic waveform frequency up to of 0.25 Hz. Focal mechanism inversions in this part of the study is done with the 1D Cut-and-Paste (CAP) method, which has the advantage of performing inversion on selected portions of Pnl and surface waves with timing shifts allowed among segments (Zhao and Helmberger, 1994; Zhu and Helmberger, 1996). We performed a detailed comparison between the synthetic waveforms generated with a 1D velocity model and those with 3D velocity models in order to consolidate station paths that are 1D-like.

The comparison between 1D and 3D synthetics for these paths indicates that within this proximal distance, 1D velocity structure surprisingly has as good resemblance of the real Earth just as the 3D model (Figure 2.3). The 3D synthetics are systematically shifted to arrive earlier by 2 seconds, which implies a generally faster 1D medium. Nonetheless, for synthetic seismograms filtered up to 0.25 Hz, major features such as the SV arrival are captured by both 1D and 3D models. For regional stations within 200 km that have high cross correlations (cc) between 3D synthetics and data, comparison between 1D synthetics and data also show similar results (Figure 2.4). Disregarding the systematic 2-second shift of 3D synthetics, both models have comparable time shifts values. Note that the 3D synthetics still contain an additional bias relative to the 1D synthetics, i.e. more yellow on average. However, much of the difference between 1D and 3D appears to be caused by the shallow structure, in that data from stations to the northwest are quite late (green) for 1D synthetics while slightly early (gold) for the 3D model. This feature can be expected based on shallow structures embedded in the 3D models, i.e. see Figure S13 of Wei et al., (2012). This comparison is complicated for several reasons: (1) origin times and locations are fixed by the seismic model, (2) the fits displayed are sometimes different for stations where 3D models have strong effects on SV arrivals, and (3) directivity effects are affected by the structure as discussed later. Besides 1D and 3D comparison, we further analyze the similarities among synthetics of different 3D velocity models. Two models are used here - JIVSM and another 3D velocity model from NIED

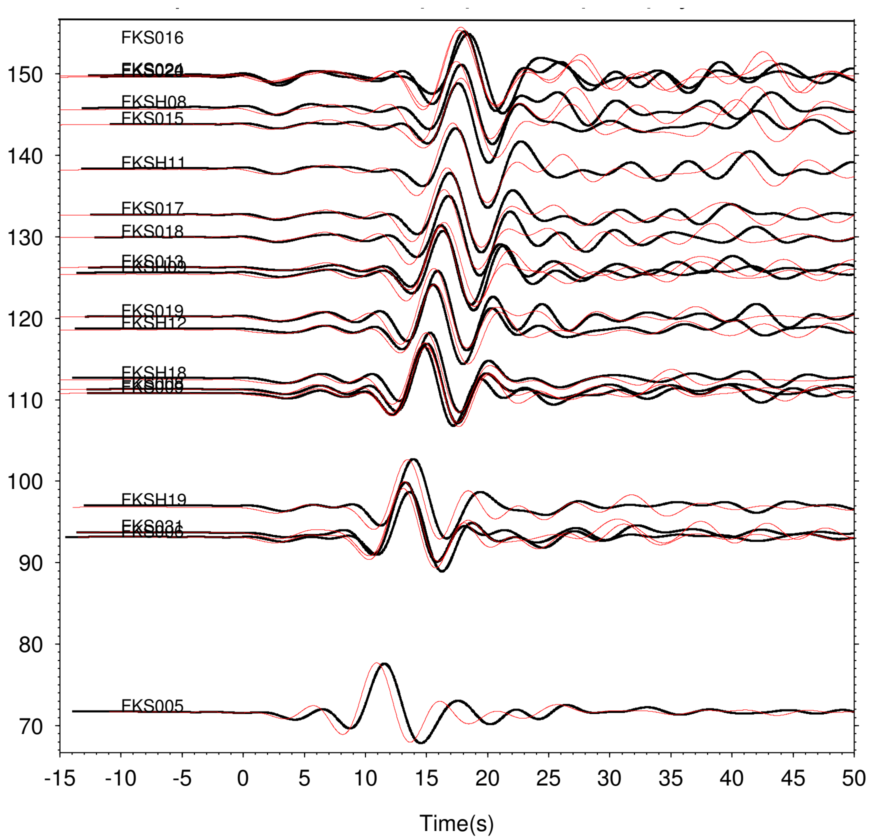

Figure 2.3: *Comparison between 1D (marked in red) and 3D (marked in black) synthetic waveforms of event E1.* Vertical velocity waveform is shown here. Stations selected are between the azimuthal range of 240° and 270°, at the nearest distances. A bandpass filter with cutoff frequencies 0.03 and 0.25 Hz is applied to the synthetics. Also, waveforms in the plot are normalized and the 3D synthetics are systematically shifted to arrive earlier by 2 seconds.

with no subducting slab structure. Results indicate that within 100 km from the epicenter, synthetics generated with the velocity model without a subducting slab are similar to those generated with velocity model having a subducting slab (Figure 2.4 and 2.5). There is also a difference in the wave amplitude of the synthetics. 1D synthetics at stations within an epicentral distance of 300 km have higher waveform amplitudes than 3D synthetics. This can be explained by the shallow crust in the 3D (JIVSM) velocity model consisting of less consolidated materials. In general, when compared to the data, 3D synthetics at this epicentral distance range also have more similar amplitude than 1D synthetics, but the discrepancy decreases with increasing epicentral distance.

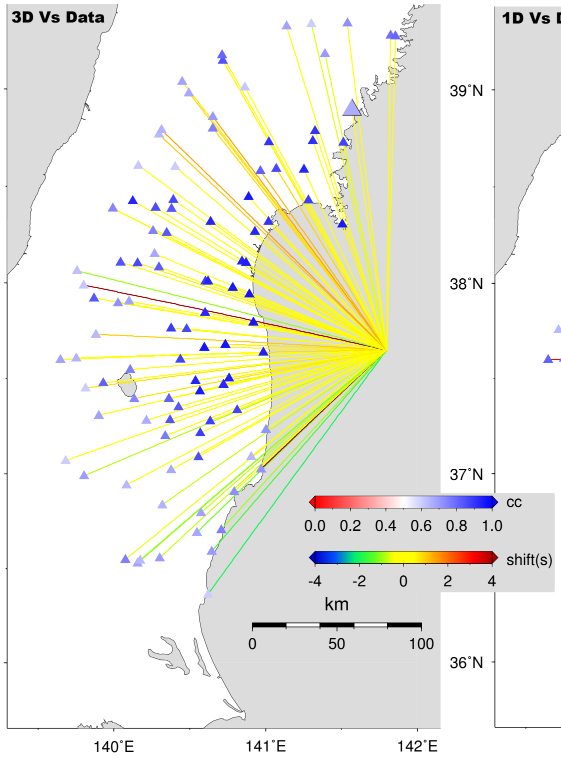

Figure 2.4: *Timing shift and cross-correlation between seismic data and 1D synthetics waveform.* (Left) Stations (triangles) are colored by the cross-correlation coefficients (cc) between 3D synthetics and waveform data (vertical component) of event E1. Only stations with > 70% cc values are plotted. Colored lines indicate time-shift value to align the data and synthetics, ranging from -4 to 4 seconds, with positive value representing faster synthetics. (Right) Similar to figure on the left, except that this is showing the cross-correlation between 1D synthetics and waveform data.

Lastly, a direct comparison is made between the 1D and 3D synthetics by running 1D CAP inversions with 3D synthetics as data. A substantial number of stations have cc > 70% for significant phases (P and S). Given such results, we are confident in using the 1D CAP results in our following analysis.

2.2.2 Source Mechanism and Rupture Characteristics of Selected Intraslab Events

We perform point-source inversions on two selected events, E1 and E2, and compare their focal mechanisms (Figure 2.6). Here we use CAP to perform inversion on waveforms from all F-net stations within an epicentral distance of 500 km. Results indicate that the CAP analysis can resolve not only similar focal mechanism as reported by JMA, but also very consistent focal mechanisms for waveform filtered

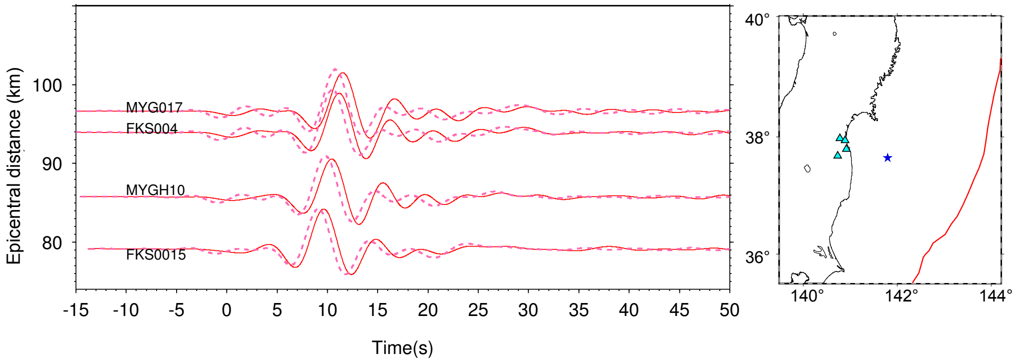

Figure 2.5: *Synthetic waveform comparison of event E1 generated from two different 3D velocity models.* (Left) Synthetic waveform comparison of event E1 generated from two different 3D velocity models. Solid lines represent the model with a subducting slab, while dotted lines represent model with no slab. (Right) Selected stations are within 100 km from the epicenter (cyan triangles), with azimuth between 270° and 300°. The blue star is the epicenter of E1.

at different frequency bands, even up to 1 Hz. This serves as a useful tool in studying complicated localized structures. Detailed inversion results are included in Figures 2.B1 to 2.B4. Furthermore, focal mechanisms for E2 and E1 resolved by JMA's F-net catalog based on long-period point source inversion are 186°/53°/77° and 183°/53°/81° (the three numbers represent strike/dip/rake) respectively, which are almost identical. Focal depths of E1 and E2, resolved by grid-search analysis with grid size of 1 km, are 53 and 50 km respectively (See Figure 2.B5a for error estimation). They are slightly shallower than F-net catalog's result, but the 3-km difference reinforces the idea that the two events are indeed in close proximity. Moreover, the time-shift values associated with the segments of the arriving P wave are also very similar between E1 and E2 (less than 2 s, Figure 2.6), which indicates a very short relative separation. This observation confirms the lateral separation of less than 4 km recorded by the JMA catalog, in which both epicenters are approximately 70 km to the east of the coastline and 180 km from the Japan Trench.

Given the almost identical hypocenter location and well-resolved source parameters, we are prompted to study the actual data in detail. In terms of frequency content, waves traveling to the south are almost identical for both earthquakes. On the other hand, for northern stations, E1 in general has lower frequency than does E2 (Figure 2.7a). It is clear that E1 has a wider arriving SV pulse than E2. Furthermore, there are distinctive differences in SH and SV amplitude ratio between stations

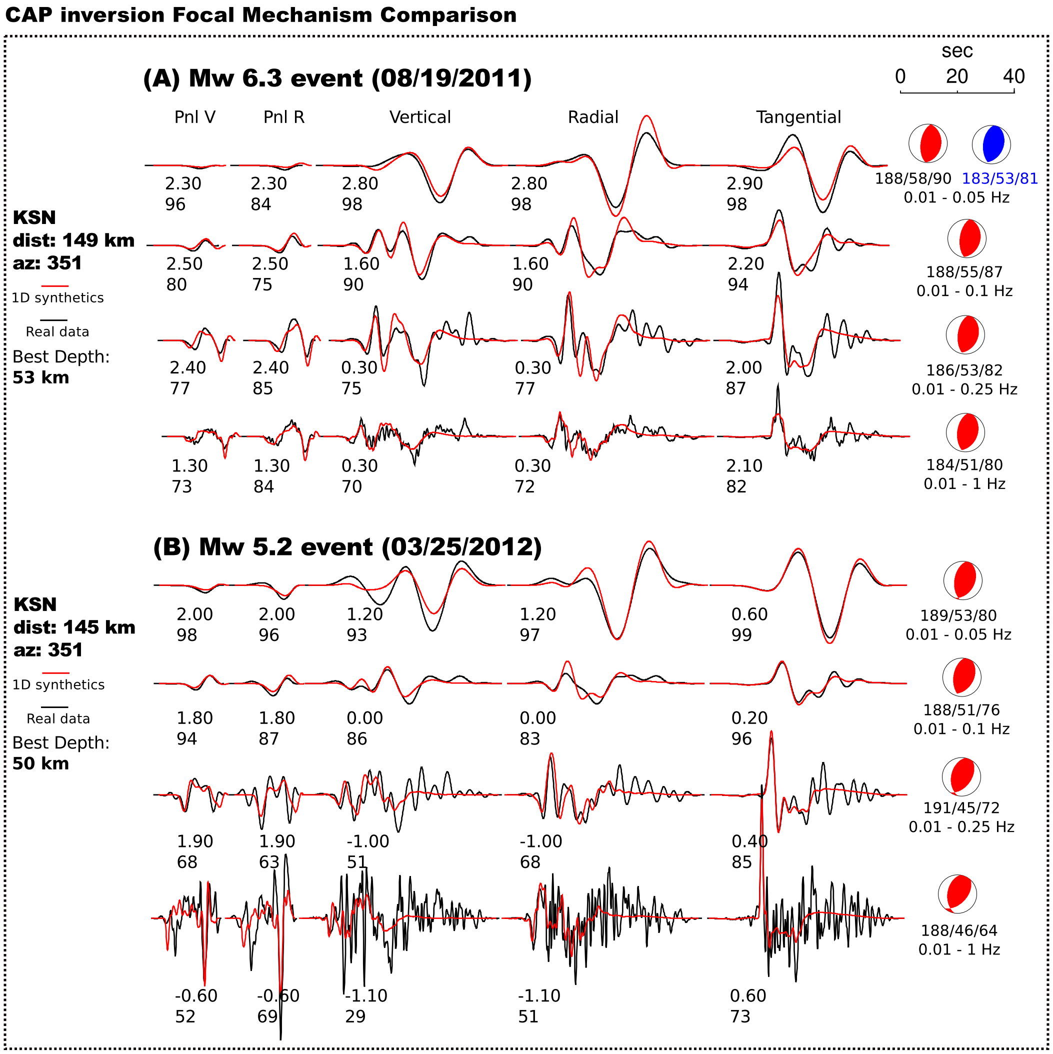

Figure 2.6: *Comparison of focal mechanisms from CAP inversion.* (a) CAP inversion of E1 waveform data (bandpass filter applied from top to bottom: up to 20s, 10s, 4s, and 1s) at F-net station KSN. Black lines are real data and red are 1D synthetics. Focal spheres in red are CAP results, and the one in blue is inversion result from JMA F-net catalog. The three-number sets indicate strike/dip/rake values. The two numbers below the waveforms are the relative time shift (top) and the cross correlation values (bottom). (b) CAP inversion of E2 waveform data at the same station, also up to 1s.

in opposite directions away from the epicenter. A comparison of SV amplitude ratio among all F-net stations displays an increasing trend from north to south (Figure 2.7b). Assuming both earthquakes being highly similar in nature, such observations strongly indicate directivity of E1 rupturing to the south. With both E1 and E2 being intraslab events, they could rupture on either of the focal planes. We therefore search for the actual rupture plane by using E2 to generate the Empirical

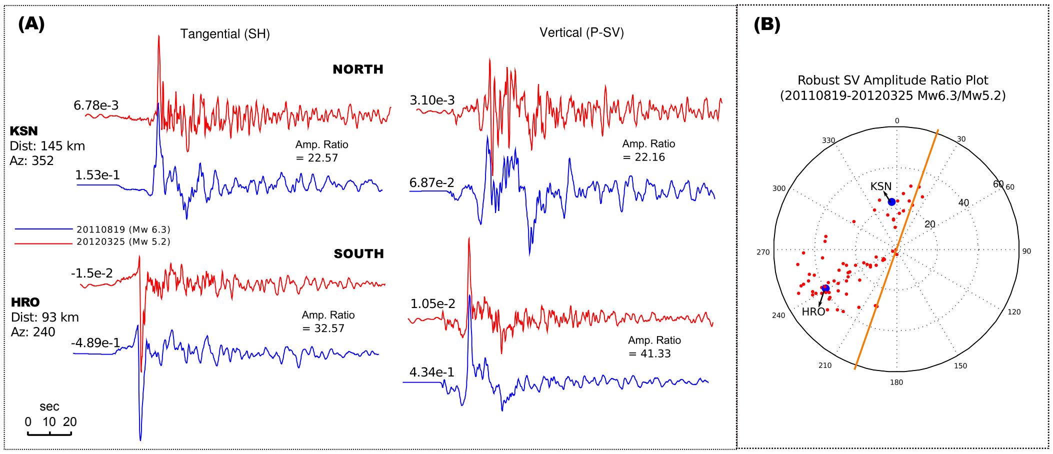

Figure 2.7: *Traces of rupture directivity from seismic data.* (A) Broadband waveform comparison (in displacement) for two similar earthquakes (E1 and E2) with an order of difference in M_w at the same two stations. KSN is a station to the north while HRO is a station to the south. E1 has signal in blue and E2 in red. Numbers stated in the beginning of the waveform are the displacement amplitudes (in cm). Amplitude ratios between the two events (SH on left column; SV on right column) are also shown. (B) Amplitude ratio of SV waves as a function of azimuth with each dot representing one station. Here the scale on the concentric circles is the amplitude ratio. Two stations in (A) are highlighted in blue. The orange line indicates the strike angle of E1.

Green's Functions (EGFs). The moment ratio between E1 (M_w 6.3) and E2 (M_w 5.2) is approximately 45. We therefore discretize the fault into a line of 45 elements, each represented as a point source of E2. Each point source position is then varied by a small time variance depending on their shift in horizontal and vertical direction from the original point source (see Appendix A). Assuming the two earthquakes began their rupture at the same spot, E1 can be treated as the summation over all elements. We simulate four simple scenarios, with rupture on each of the two auxiliary focal planes, directing to north or south respectively. The fault geometries are based on CAP inversion with data up to 0.25 Hz. Strike/Dip values are 186°/53° for plane 1 and 19°/37° for conjugate plane 2.

With fixed rupture direction and fault geometry, we search for a wide range of rupture velocity and rupture length to obtain the simulation with the lowest misfit error between E1 broadband data and the corresponding EGFs (Table 2.B2 and 2.B3). The misfit error is the summation of l_2 norm, weighted by their corresponding cc. Here we explore both displacement and velocity data and find consistent results, with the same best rupture velocity resolved and a rupture length difference of

1 km. Results indicate that E1 can be represented by 45 point sources, each 0.18 km apart, rupturing diagonally to the south on the plane dipping 37° to the east, with a rupture velocity at 4.5 km/s over a distance of 8 km (Figure 2.8). We

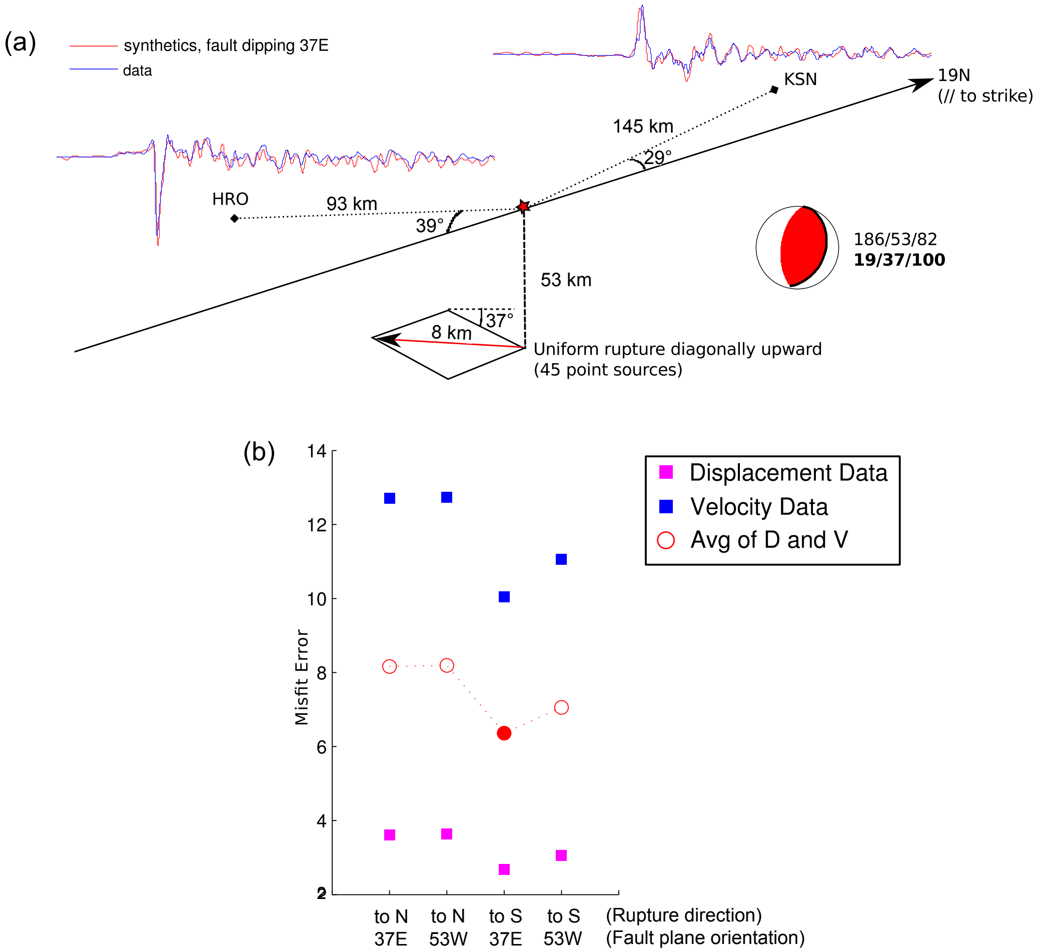

Figure 2.8: *Modeling rupture directivity using the empirical Green's function approach.* (a) Geometrical setting of the study on secondary source parameters: (Here we simulate E1 waveform (blue) using a summation of 45 point sources equivalent to E2, each with a small amount of time shift calculated using power series expansion based on general ray theory. Four rupture patterns are tested and the one with highest cross-correlation (cc) value between data and synthetic is shown, with estimated rupture direction and total rupture length. Focal mechanism of E1 is also shown here, with black line on the focal sphere indicating the preferred rupture fault plane. (b) Comparison of misfit error among four rupture simulations. Rupture toward the South on the fault plan dipping 37°E has the lowest average misfit error (filled red circle) for both displacement and velocity data. The misfit error is the l_2 norm weighted by their corresponding cc value. Detailed quantitative comparison is shown in Tables 1.B2 and 1.B3.

consider 4.5 km/s a reasonable rupture speed, given the event occurred inside the mantle where shear wave speed is 4.5 km/s or higher. Assuming a square rupture dimension with diagonal length of 8 km (~ 5.6 x 5.6 km^2), E1 has generated a slip of approximately 3 m. (For data and EGF comparisons of different station components, see Figures 2.B6 and 2.B7.)

2.2.3 Intraslab Thrust Events and Stress Change from the Mw 9.1 Main Shock

Since March 11, 2011, numerous studies have been focusing on the state of stress changes in the seismogenic zone (Hasegawa et al., 2011; Kato et al., 2011; Toda et al., 2011; Zhang et al., 2008). The series of intraslab events observed occurring along this long weakened zone inside the slab also seems to suggest a causal effect. With well resolved source mechanism and rupture characteristics of E1, we extend our study to explore whether the faulting of E1, or other intraslab thrusting events in neighboring region with similar mechanism, is directly related to the M_w 9.1 main shock. Here we calculate the static stress change induced by the slip of the mainshock. We use the slip distribution obtained by Huang et al., (2014), who in their simulation reproduce the final slip distribution model and stress drop of the main shock. Their result is consistent with the general final slip inferred for this earthquake (Figure 2.B8). With calculated stress drops and based on the Coulomb model, we model the differential stress ($\sigma 1$ - $\sigma 2$) caused by the megethrust rupture (Figure 2.9, top) to the surrounding area, where $\sigma 1$ and $\sigma 2$ are the maximum and minimum stresses in principal directions. The maximum shear stress ($\sigma 1$ - $\sigma 2$)/2 is concentrated at the portion of the megathrust approximately 90 km from the trench (0 km), which also coincides with the downdip end of the rupture plane in the model proposed by Wei et al., (2012).

The effect of maximum shear stress varies along area adjacent to the megathrust (Figure 2.9, bottom). Depending on locations relative to the megathrust, it favors different faulting mechanisms, so either normal and thrust events could possibly be triggered, both below and above the megathrust interface. Our analysis shows that the region between 0 and 5 km below the downdip tip of the interface is favorable for thrusting events (resolved as negative dip angles in the simulation) on fault dipping between 20° to 50°. The dip angles of the intraslab events discussed here lie well within this range. Our result is consistent with the hypothesis that this sequence of intraslab aftershocks, which possibly ruptured a continuous weakening zone inside the slab, are the results of the stress change induced by the main shock.

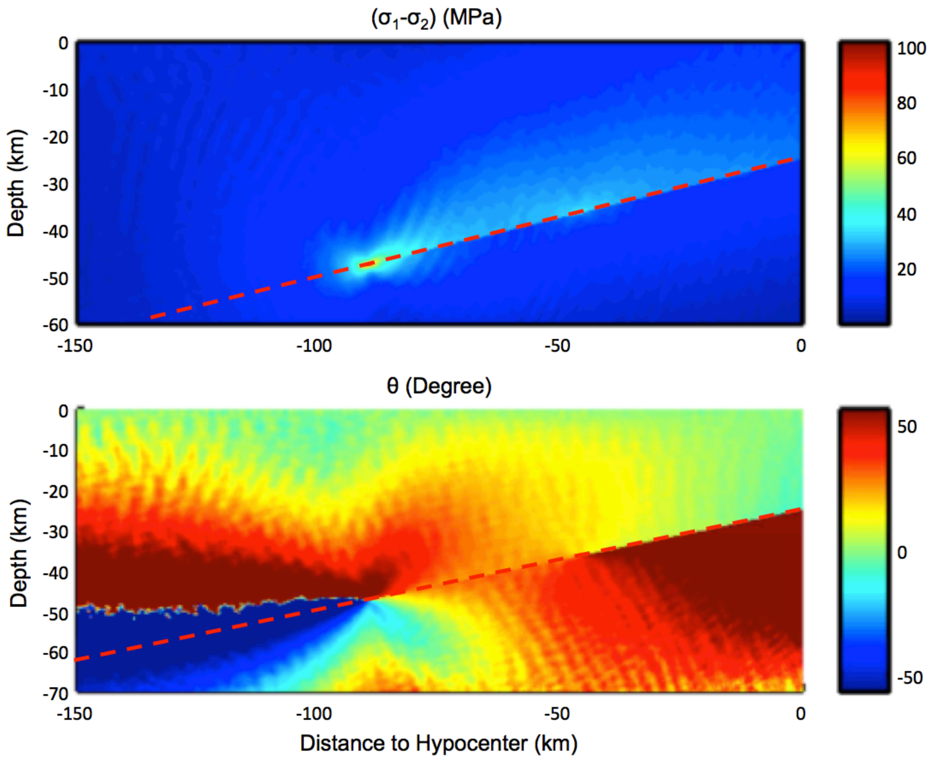

Figure 2.9: *Stress change of the region after the M_w 9.1 mainshock.* (Top) Differential stress ($\sigma 1$ - $\sigma 2$) caused by the M_w 9.1 earthquake to neighboring region. Huang et al. (2013) assumes a megathrust dipping 14° (dashed red line). (Bottom) Mechanism of earthquakes as a possible outcome produced by this differential stress. Positive (warm color) degrees imply normal faulting, while negative (cold color) degrees suggest thrust faulting.

2.3 Discussion

The epicenters of E1 and E2 are only 50 km south of the M_w 7.1 intraslab aftershock that took place on April 7, 2011. Within the region, there is also a series of events that possess focal depth within the intraslab range and fault-plane orientation similar to that of E1, with strike and dip values ±10°. Altogether, they form a narrow line of events between latitude 37° to 39° from north to south (Figure 2.1). Interestingly, intraslab events with such features are almost completely absent from neighboring area. Such events also did not exist in this region before the M_w 9.1 event. These evidence all point to the possibility that this group of earthquakes have occurred on a north-south striking fault dipping about 35° eastward, which is hypothesized to be a weak hydrated zone reactivated as a thrust fault after March 11, 2011 (Nakajima et al., 2011), spanning a distance of 150 km. Since the occurrence of the M_w 9.1 earthquake, numerous studies are prompted to study the physical mechanism of the megathrust that drives such unique rupture pattern. So far it has still proven very difficult to solve the problem. Given the intriguing coincidence that these intraslab events are located in close proximity to the source of high-frequency radiation during the main event, these intraslab earthquakes in the downdip area can be valuable assets in enhancing our understanding of this local region. Similar to the forward modeling technique implemented by Tan and Helmberger, (2010), our study also uses the EGF approach and simulates earthquake ruptures. We show that using two co-located seismic events, the details of fault rupture can be extracted. Assuming this group of intraslab earthquakes occur on the same continuous weakened zone, the dip angle resulted from our inversion (37°E) is in fact very similar to the estimates in studies that are based on the spatial distribution of aftershocks. Ohta et al., (2011) simulated the Mw 7.1 aftershock with the assumption of a fault plane dipping 35.3°E. Nakajima et al., (2011) discovered that the angle between this fault plane and the dip of the slab surface is approximately 60°. Among typical subduction models of this region, the slab at this particular distance from the trench is dipping about 35° westward. This implies that the fault plane on which E1 occurred is dipping about 35°E. These intraslab events are all located within 10 km from the plate interface, and thus it is important to resolve for the dimension and directivity of these ruptures in order to estimate the extent of disruption these smaller events can have on the megathrust shear zone. In fact, the high resolution of the directivity study can be a useful tool in refining the source locations, especially for earthquakes lacking azimuthal coverage of seismic stations. According to JMA, the epicentral location of the E1 and E2 are laterally separated by less than 4 km. Thus, using CAP inversion method, one should expect similar time shift between synthetics and data for both events. However, for waveform filtered up to 0.1 Hz, the resulting time shift of the S arrival differs by as much as 2.5 seconds between E1 and E2 (Figures 2.6 and 2.10a). Such a discrepancy does not necessarily imply incorrect epicenter locations. In particular, we find that in a long-period inversion, one should consider using the centroid location rather than the epicentral location. Hence we refine the centroid location based on the resolved rupture dimension, and the inversion result indicates a much smaller time shift difference between the two events (Figure 2.10b).

It is also interesting to address the origin of these weak lineate zones inside the slab. One possible explanation is that the earthquake is a reactivation of a buried fault formed at the outer rise of the trench as normal faulting prior to subduction. The fault is dipping 37°, which is approximately equivalent to a 60°-dipping normal fault given the slab at this position is subducting at 30° westward (see Figure 2.1 inset). Hence,

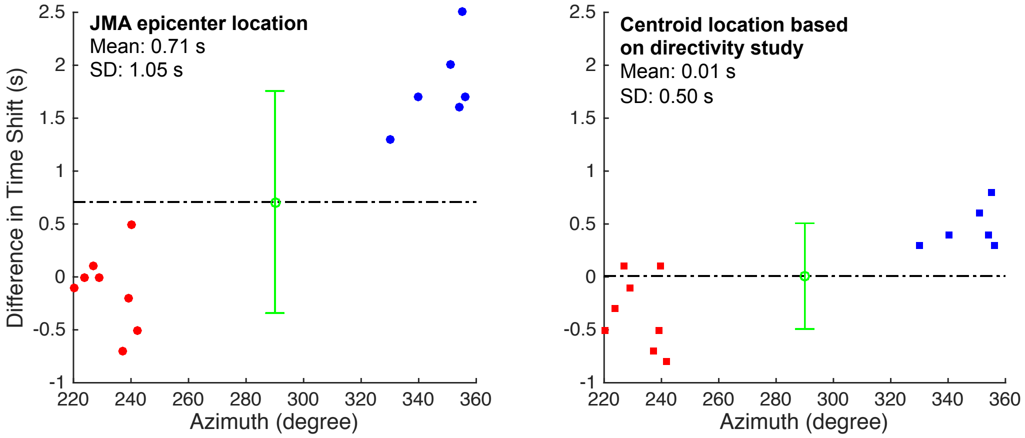

Figure 2.10: *Comparison of the difference in time shift values of E1 and E2 with different epicentral location.* Red and blue markers present stations with azimuths smaller and larger than 300deg, respectively. (Left) JMA location; (Right) new centroid location based on our directivity study. This illustrates that if we use the centroid location for long-period inversion, the difference in time shift is significantly lower.

the intraslab events on the fault may serve as useful tools in understanding historical and future outer rise events. The 1933 Sanriku earthquake is one of the several outer-rise earthquakes in the region that has been studied. The depth extend of this earthquake is not well resolved, but there is hypothesis that the rupture is a normal faulting on a 45°-dipping plane that ruptures the oceanic plate, with a dimension of 185 by 100 km^2 (Kanamori, 1971). This outer-rise event occurred over three decades after the 1896 Meiji-Sanriku underthrust earthquake in the region exactly adjacent to the 1896 rupture zone, and both earthquakes generated huge tsunamis. There are also other studies on similar doublets but with a much shorter time separation, in the scale of days (Ammon et al., 2008; Hino et al., 2009). Nonetheless, our current understanding for large outer rise events is still limited due to their sparse occurrences. Therefore studying the extent of subducted faults formed in the outer rise could provide a better understanding to this phenomenon and the potential risk of tsunami hazards in the area (Lay et al., 2011).

2.4 Conclusion

The unique rupture pattern of the Tohoku-Oki megathrust earthquake has prompted this study of the shear zone. We lay out a three-step study that focus on exploring the source and rupture mechanism of smaller aftershocks inside the subducting slab, which are beneath the downdip edge of the main shock rupture. Our results indicate that within 150 km proximity to epicentral location, 1D and 3D velocity model show comparable validity in modeling seismic events up to 1 Hz. Using a forward modeling approach with EGFs, we are able to simulate the rupture of a M_w 6.3 intraslab event and resolve the fault plane without relying on the spatial distribution of other aftershocks. The fault geometry and focal mechanism of this earthquake is also found to be the predicted outcome of the shear stress change caused by the main shock. Based on the resolved dip angle, together with other similar neighboring intraslab events, a weakened zone of up to 150 km is believed to have reactivated, which can be a long normal fault previously formed in the outer rise region. Further study on the downdip region through these intraslab events may shed light on understanding historical and future outer-rise events, as well as the potential cause of high-frequency energy radiation during the M_w 9.1 mainshock.

2.5 Appendix A: Generating Empirical Green's Functions

To generate empirical Green's Functions using E2, based on the generalized ray theory (Helmberger, 1983) the characteristic travel time of a generalized ray in a layered half-space is given by:

$$t_0 = p_0 r + \sum_i \eta_i d_i, \tag{2.1}$$

where r is the source-receiver distance, η_i the vertical slowness of the ray in each layer, and d_i the vertical distance of the ray segment in each layer. For two very close sources, the paths to the receiver will be highly similar in shape and differ only by a small time shift dt_0. This time variance (dt_0) can be approximated by using Taylor series expansion for t0 around the position of the point source (r, h).

$$dt_0 = \frac{\partial t_0}{\partial r} dr + \frac{\partial t_0}{\partial h} dh \tag{2.2}$$

$\partial t_0 / \partial r$ is essentially p_0, which is treated as a constant here. $\partial t_0 / \partial h = -\varepsilon \eta_s$, where ε = 1 for down-going rays and ε = -1 for up-going rays. η_s, which equals $[(1/v_s^2) - p_0^2]^{1/2}$, is the vertical slowness of the ray p_0 in the source region. The velocity in the source region is represented by v_s. p_0 and η_s in this study are numerical estimation from synthetics generated at different depths based on the 1D velocity model used for CAP inversion.

Here we assume E1 to be a finite-fault earthquake which is 45 times larger than E2 in moment magnitude. Thus, we discretize the rupture region into a line of 45 elements, each represented as an E2 point source. The total response ($R(t)$) of E1 at the receiver can then be represented by a summation of the 45 rays, each properly lagged in time according to the relative position from the reference point source.

$$R(t) = \sum_{i=1}^{45} E2_i(t - dt_{0i}) \tag{2.3}$$

Since we assume four rupture scenarios, diagonally northward and southward on the two auxiliary focal planes, there is a set of four empirical Green's Functions $R(t)$ generated, which is then compared with the data obtained to determine rupture directivity.

2.6 Appendix B: Supplementary Information

This section consists of a list of 8 supplementary figures and 3 tables.

Figures 2.B1-2.B4: Highlighted inversion results generated using the Cut-and-Paste (CAP) method based on the 1D velocity model shown in Table 1.B1. The ten stations selected are within an epicentral distance of 300 km. Figures 2.B1-2.B4 are inversions of the same set of stations with frequency bands up to 0.05, 0.1, 0.25, and 1 Hz respectively.

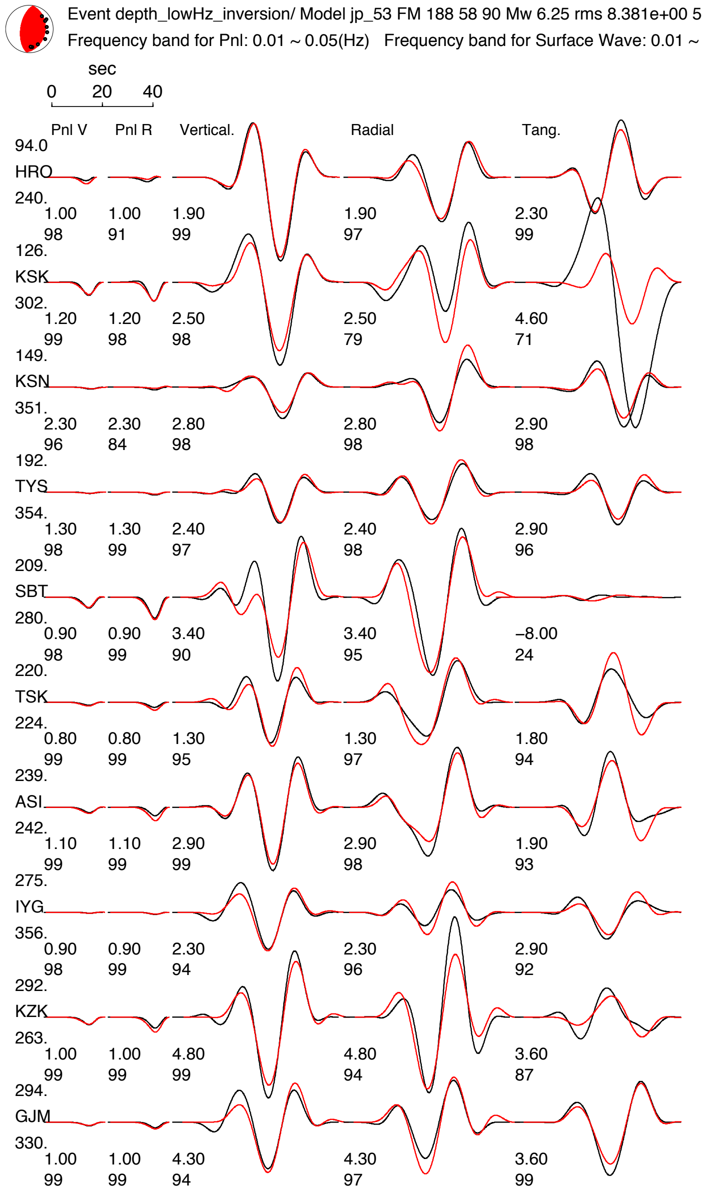

Figure 2.B1: Inversions of the same set of stations with frequency bands up to 0.05 Hz.

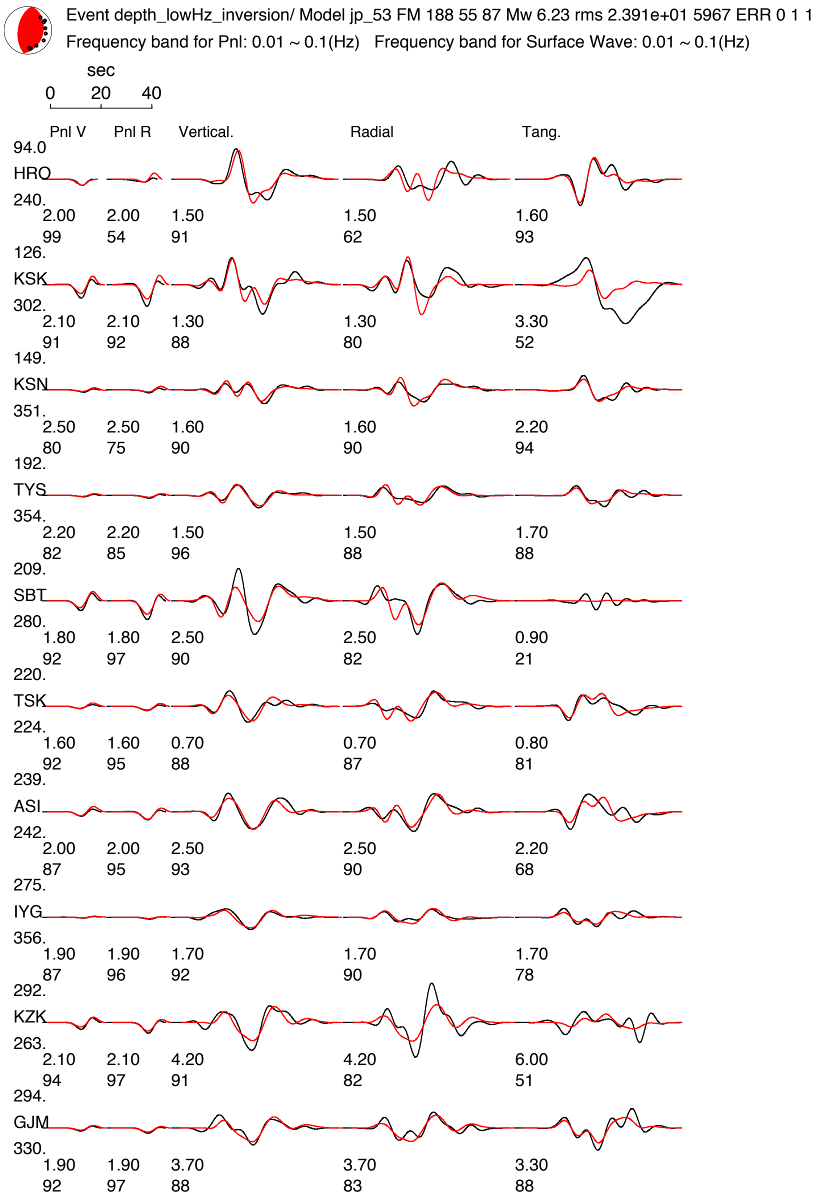

Figure 2.B2: Waveform inversion with frequency bands up to 0.1 Hz.

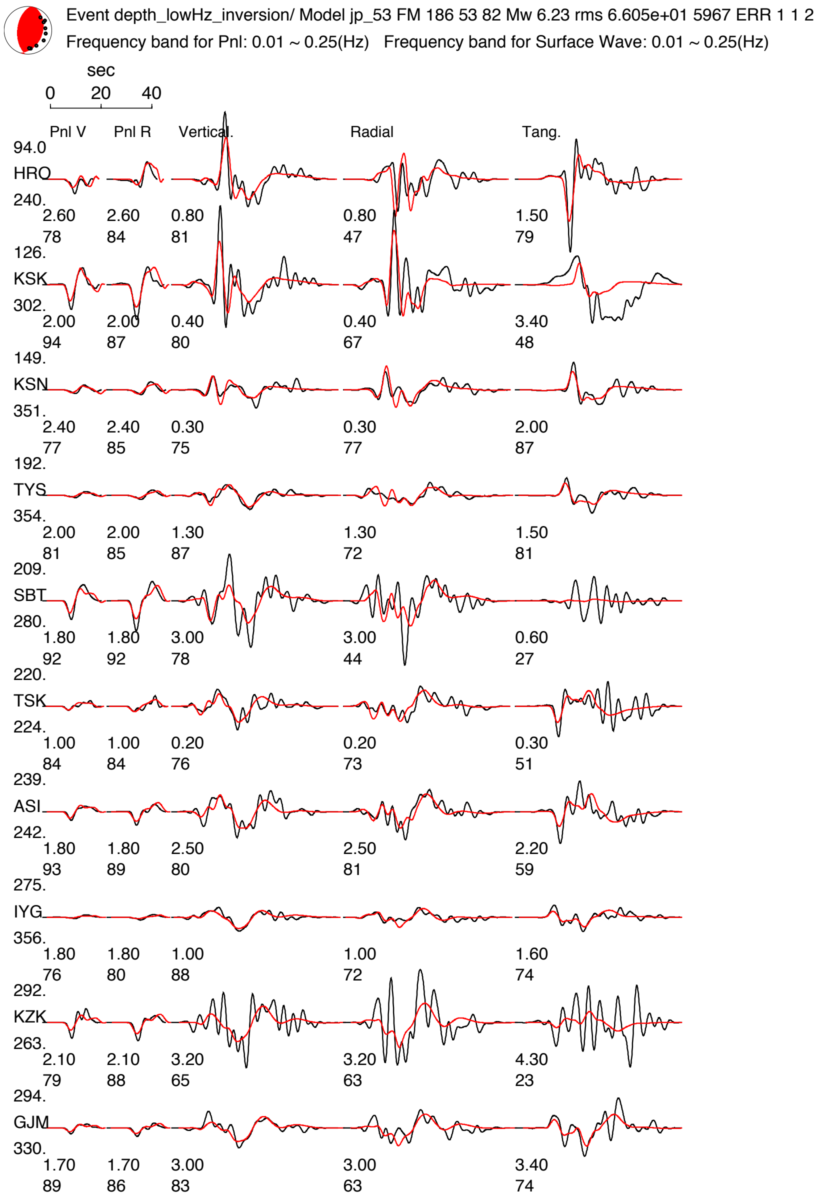

Figure 2.B3: Waveform inversion with frequency bands up to 0.25 Hz.

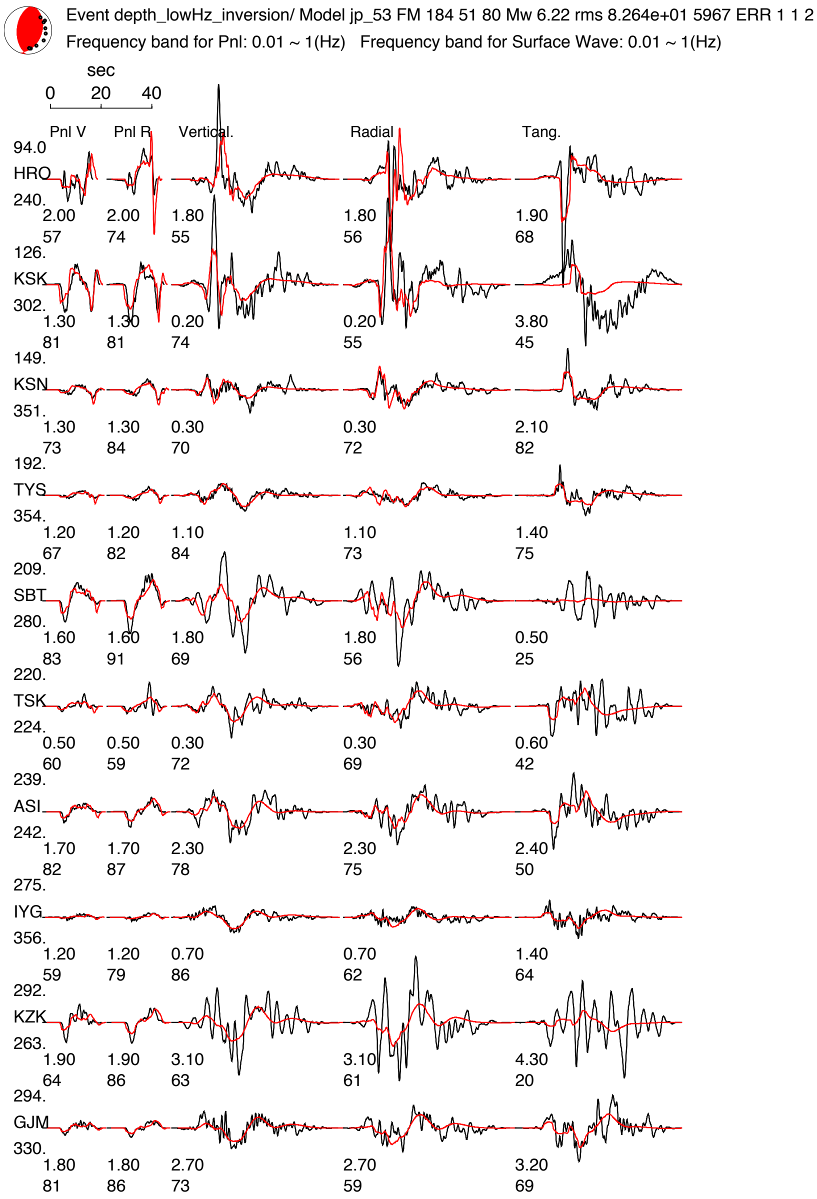

Figure 2.B4: Waveform inversion with frequency bands up to 1 Hz.

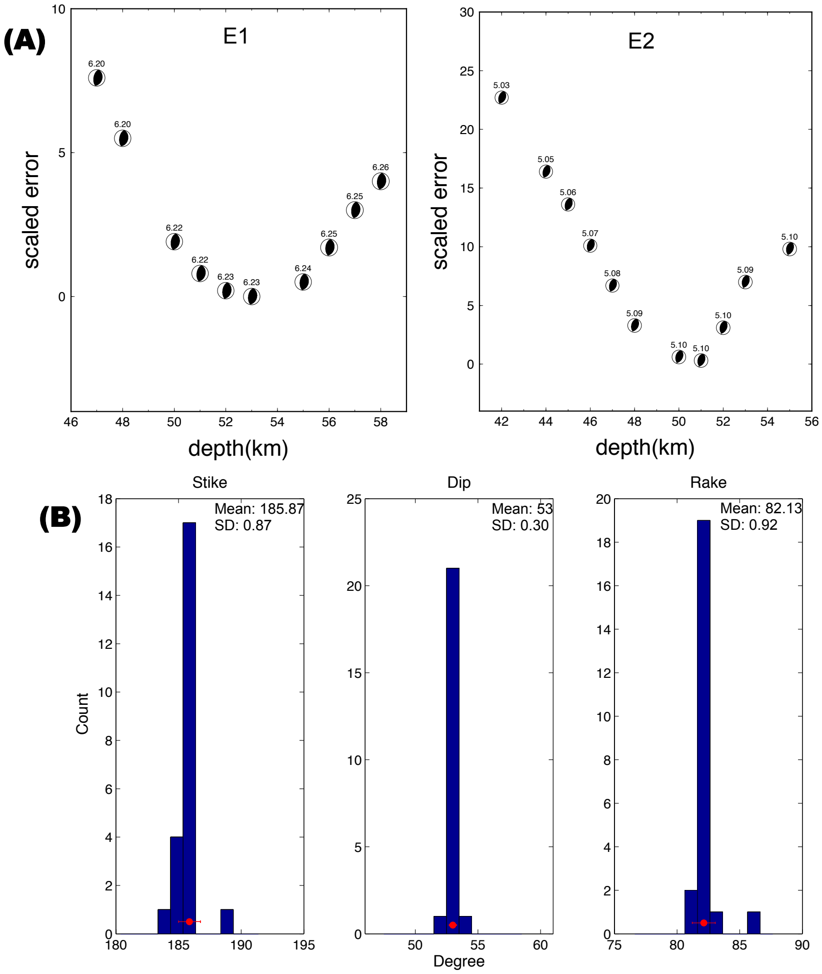

Figure 2.B5: *Detailed analysis result of CAP inversion.* (a) Fractional mismatch for the range of focal depths tested. Results indicate that 53 km and 50 km are the best focal depth determined for E1 and E2. (b) Bootstrapping analysis on stations selected for CAP inversion. Standard deviation of all three parameters ranges within 1.5°.

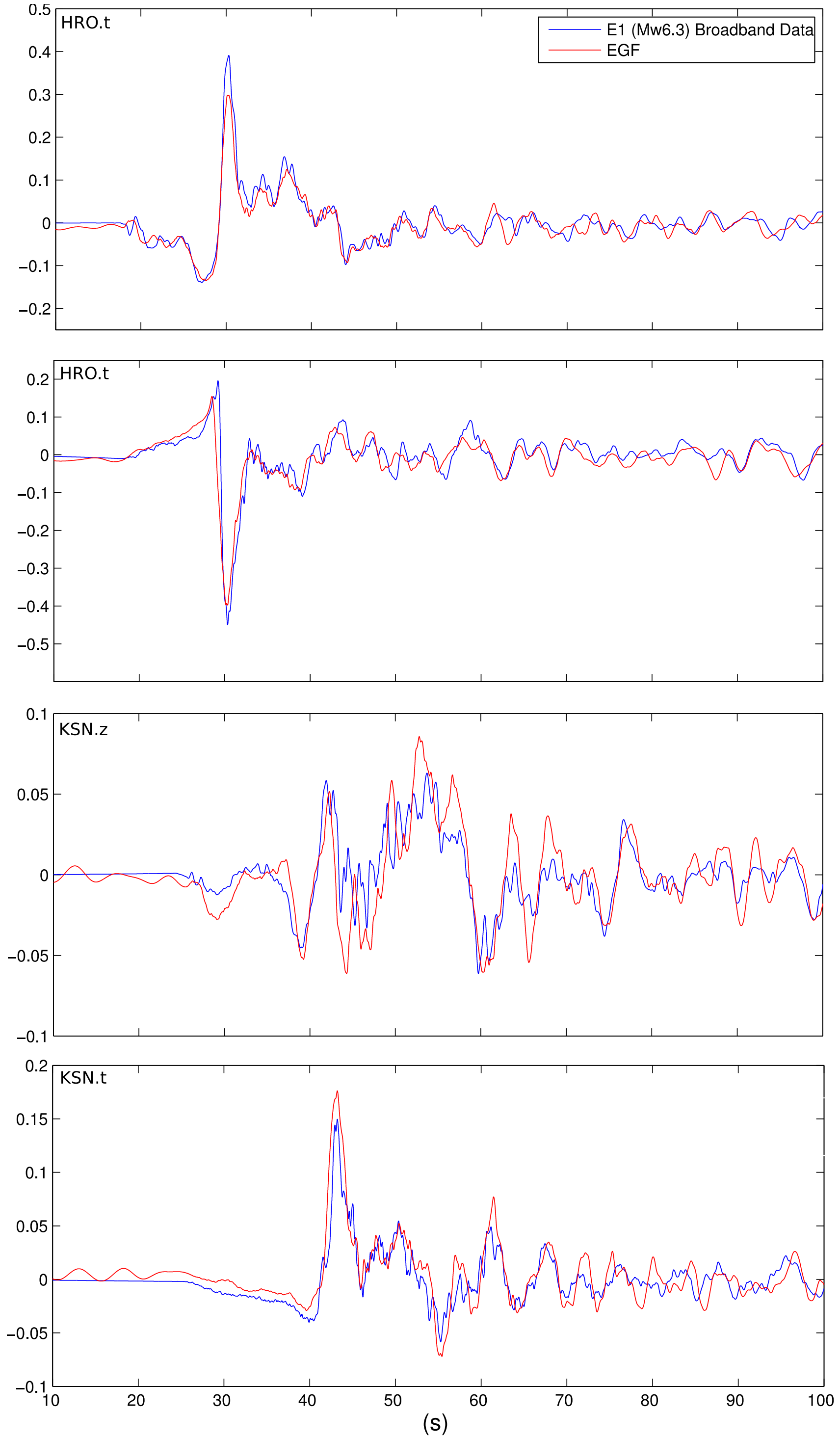

Figure 2.B6: *Comparison of E1 broadband displacement data and EGFs at two of the nearest stations HRO and KSN. (vertical and tangential components respectively)* (vertical and tangential components respectively). This is the rupture simulation with the lowest average misfit error (rupture length: 8 km, rupture velocity 4.5 km/s).

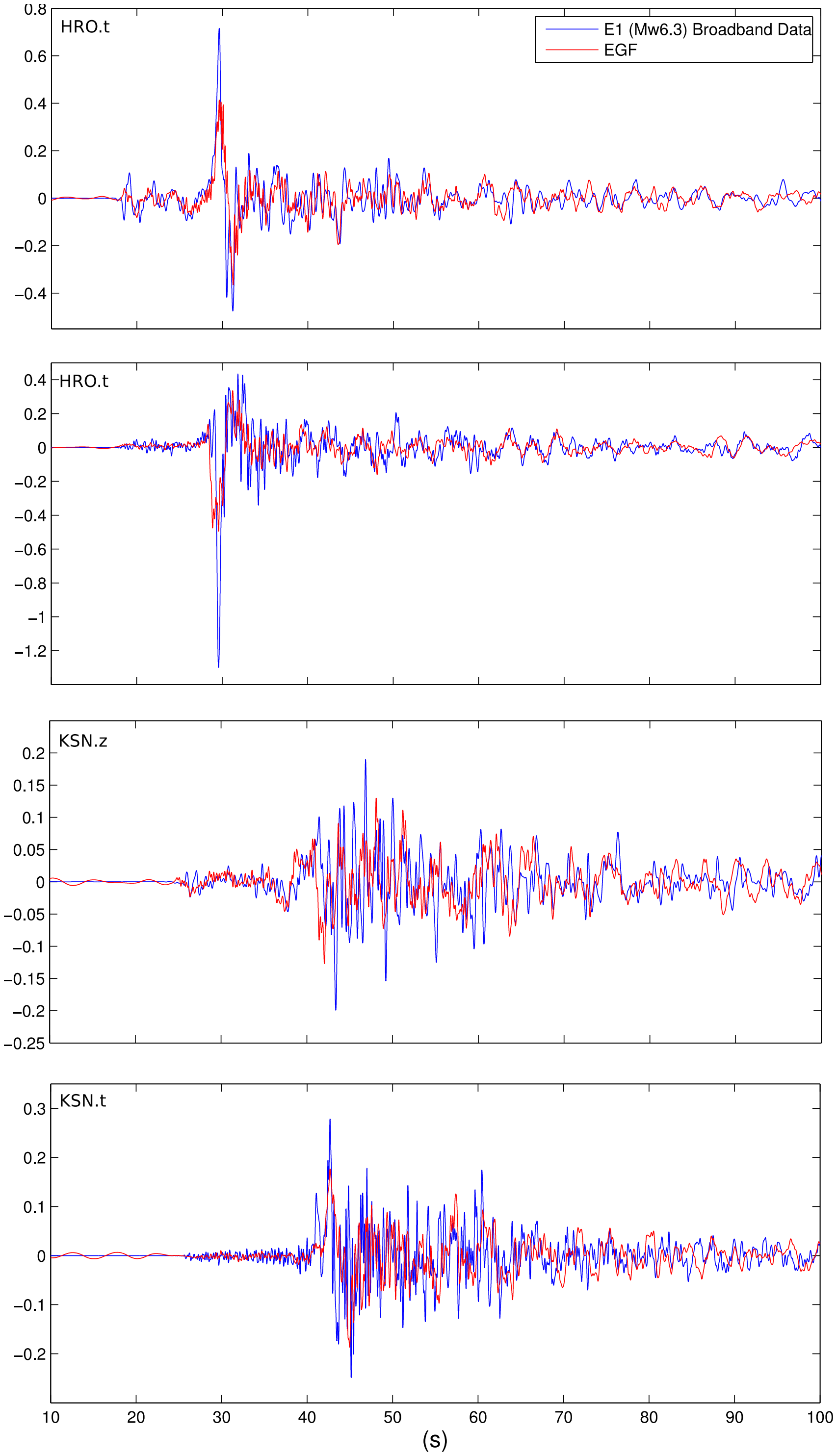

Figure 2.B7: *Comparison of E1 broadband velocity data and EGFs at two of the nearest stations HRO and KSN (tangential and vertical components respectively).* This is the rupture simulation with the lowest average misfit error (rupture length: 9 km, rupture velocity 4.5 km/s).

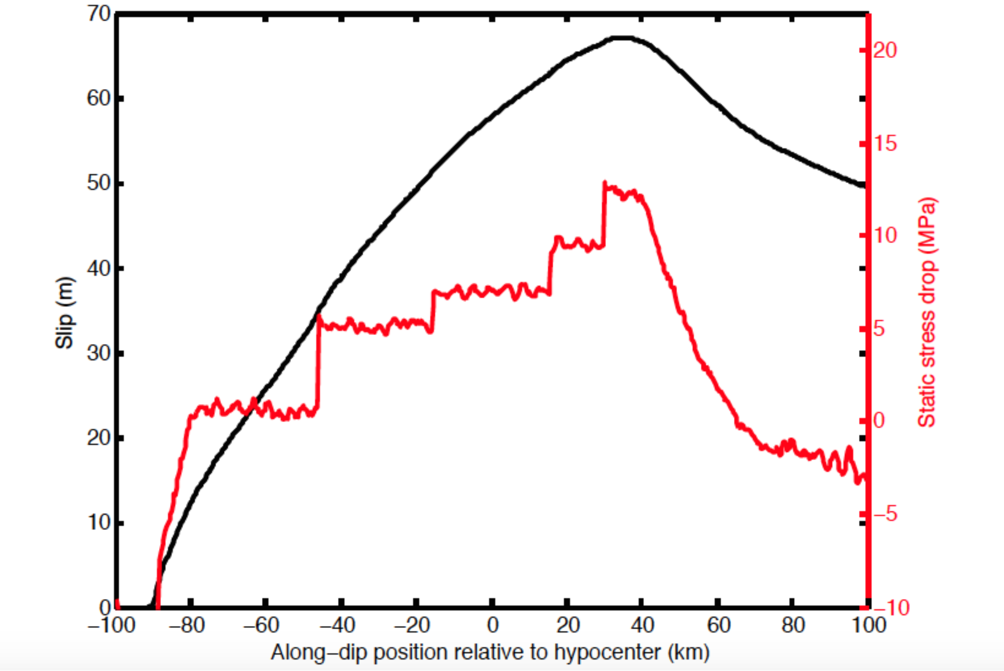

Figure 2.B8: *Final slip and static stress drop of the main event.* Reprinted figure from Huang et al., 2013, showing the along-dip distribution of final slip and static stress drop assumed in the dynamic rupture model.

Layer thickness (km)	V_S (km/s)	V_P (km/s)	Density (g/cm^3)
4.00	2.51	4.40	2.00
10.00	3.46	6.00	2.60
16.00	3.87	6.70	2.90
12.50	4.50	7.70	3.30

Table 2.B1: *1D crustal model for the Tohoku-Oki region studied.*

Station		to N, dip 33°E	to N, dip 57°W	**to S, dip 33°E**	to S, dip 57°W
HRO.z	l^2	4.35	4.37	3.50	4.34
	cc	98.20%	98.17%	98.75%	98.20%
HRO.t	l^2	7.62	7.69	4.82	7.62
	cc	95.46%	95.37%	97.75%	95.50%
KSN.z	l^2	3.23	3.24	2.53	2.49
	cc	60.89%	60.8%	63.76%	64.53%
KSN.t	l^2	2.57	2.58	2.61	2.58
	cc	96.01%	96.02%	94.48%	94.21%
	Avg. Misfit	3.62	3.65	**2.68**	3.05

Table 2.B2: *Simulation results based on displacement data.* Best resolved rupture distance and velocity are 8 km and 4.5 km/s respectively. $l_2 = ||EGF - E1||_2$. cc is the cross-correlation value of the S phases (SV, SH). The average misfit error is the summation of all components' l_2 weighted by their corresponding cc.

Station		to N, dip 33°E	to N, dip 57°W	**to S, dip 33°E**	to S, dip 57°W
HRO.z	l^2	14.02	14.09	11.92	13.85
	cc	73.69%	73.51%	83.13%	79.58%
HRO.t	l^2	22.77	22.83	22.11	21.83
	cc	53.99%	53.74%	72.96%	59.87%
KSN.z	l^2	7.96	7.97	5.83	5.68
	cc	46.57%	46.01%	47.44%	44.11%
KSN.t	l^2	7.57	7.59	7.30	7.22
	cc	52.52%	52.45%	50.08%	50.84%
	Avg. Misfit	12.71	12.74	**10.04**	11.06

Table 2.B3: *Simulation results based on velocity data.* Best resolved rupture distance and velocity are 9 km and 4.5 km/s respectively, which are consistent with the results from using displacement data.

2.7 References

Ammon, Charles J, Hiroo Kanamori, and Thorne Lay (2008). “A great earthquake doublet and seismic stress transfer cycle in the central Kuril islands”. In: *Nature* 451.7178, pp. 561–565. DOI: `10.1038/nature06521`. URL: `http://dx.doi.org/10.1038/nature06521`.

Fujiwara, Toshiya, Shuichi Kodaira, Tetsuo No, Yuka Kaiho, Narumi Takahashi, and Yoshiyuki Kaneda (2011). “The 2011 Tohoku-Oki earthquake: Displacement reaching the trench axis”. In: *Science* 334.6060, pp. 1240–1240. DOI: `10.1126/science.1211554`. URL: `http://dx.doi.org/10.1126/science.1211554`.

Graves, Robert W (1996). “Simulating seismic wave propagation in 3D elastic media using staggered-grid finite differences”. In: *Bulletin of the Seismological Society of America* 86.4, pp. 1091–1106.

Hartzell, Stephen H. (1978). “Earthquake aftershocks as Green’s functions”. In: *Geophysical Research Letters* 5.1, pp. 1–4. ISSN: 1944-8007. DOI: `10.1029/GL005i001p00001`. URL: `http://dx.doi.org/10.1029/GL005i001p00001`.

Hasegawa, Akira, Keisuke Yoshida, and Tomomi Okada (2011). “Nearly complete stress drop in the 2011 Mw 9.0 off the Pacific coast of Tohoku Earthquake”. In: *Earth, planets and space* 63.7, pp. 703–707. DOI: `10.5047/eps.2011.06.007`. URL: `http://dx.doi.org/10.5047/eps.2011.06.007`.

Helmberger, DV (1983). “Theory and application of synthetic seismograms”. In: *Earthquakes: observation, theory and interpretation* 37, pp. 173–222.

Hino, Ryota et al. (2009). “Insight into complex rupturing of the immature bending normal fault in the outer slope of the Japan Trench from aftershocks of the 2005 Sanriku earthquake (Mw= 7.0) located by ocean bottom seismometry”. In: *Geochemistry, Geophysics, Geosystems* 10.7. DOI: `10.1029/2009GC002415`. URL: `http://dx.doi.org/10.1029/2009GC002415`.

Huang, Yihe, Jean-Paul Ampuero, and Hiroo Kanamori (2014). “Slip-weakening models of the 2011 Tohoku-Oki earthquake and constraints on stress drop and fracture energy”. In: *Pure and Applied Geophysics* 171.10, pp. 2555–2568. DOI: `10.1007/s00024-013-0718-2`. URL: `http://dx.doi.org/10.1007/s00024-013-0718-2`.

Huang, Yihe, Lingsen Meng, and Jean-Paul Ampuero (2012). “A dynamic model of the frequency-dependent rupture process of the 2011 Tohoku-Oki earthquake”. In: *Earth, planets and space* 64.12, pp. 1061–1066. DOI: `10.5047/eps.2012.05.011`. URL: `http://dx.doi.org/10.5047/eps.2012.05.011`.

Ide, Satoshi, Annemarie Baltay, and Gregory C Beroza (2011). “Shallow dynamic overshoot and energetic deep rupture in the 2011 Mw 9.0 Tohoku-Oki earthquake”. In: *Science* 332.6036, pp. 1426–1429. DOI: `10.1126/science.1207020`. URL: `http://dx.doi.org/10.1126/science.1207020`.

Ito, Yoshihiro et al. (2011). “Frontal wedge deformation near the source region of the 2011 Tohoku-Oki earthquake”. In: *Geophysical Research Letters* 38.7. L00G05, n/a–n/a. ISSN: 1944-8007. DOI: `10.1029/2011GL048355`. URL: `http://dx.doi.org/10.1029/2011GL048355`.

Kato, Aitaro and Toshihiro Igarashi (2012). “Regional extent of the large coseismic slip zone of the 2011 Mw 9.0 Tohoku-Oki earthquake delineated by on-fault aftershocks”. In: *Geophysical Research Letters* 39.15. DOI: `10.1029/2012GL052220`. URL: `http://dx.doi.org/10.1029/2012GL052220`.

Kato, Aitaro, Shin?ichi Sakai, and Kazushige Obara (2011). “A normal-faulting seismic sequence triggered by the 2011 off the Pacific coast of Tohoku Earthquake: Wholesale stress regime changes in the upper plate”. In: *Earth, planets and space* 63.7, pp. 745–748. DOI: `10.5047/eps.2011.06.014`. URL: `http://dx.doi.org/10.5047/eps.2011.06.014`.

Koketsu, Kazuki, Hiroe Miyake, Hiroyuki Fujiwara, and Tetsuo Hashimoto (2008). “Progress towards a Japan integrated velocity structure model and long-period ground motion hazard map”. In: *Proceedings of the 14th World conference on earthquake engineering*, S10–038.

Lay, Thorne, Charles J Ammon, Hiroo Kanamori, Marina J Kim, and Lian Xue (2011). “Outer trench-slope faulting and the 2011 Mw 9.0 off the Pacific coast of Tohoku Earthquake”. In: *Earth, planets and space* 63.7, pp. 713–718. DOI: `10.5047/eps.2011.05.006`. URL: `http://dx.doi.org/10.5047/eps.2011.05.006`.

Lin, Jian and Ross S. Stein (2004). “Stress triggering in thrust and subduction earthquakes and stress interaction between the southern San Andreas and nearby thrust and strike-slip faults”. In: *Journal of Geophysical Research: Solid Earth* 109.B2. B02303, n/a–n/a. ISSN: 2156-2202. DOI: `10.1029/2003JB002607`. URL: `http://dx.doi.org/10.1029/2003JB002607`.

Nakajima, Junichi, Akira Hasegawa, and Saeko Kita (2011). “Seismic evidence for reactivation of a buried hydrated fault in the Pacific slab by the 2011 M9. 0 Tohoku earthquake”. In: *Geophysical Research Letters* 38.7. DOI: `10.1029/2011GL048432`. URL: `http://dx.doi.org/10.1029/2011GL048432`.

Ohta, Yusaku et al. (2011). “Large intraslab earthquake (2011 April 7, M 7.1) after the 2011 Off the Pacific Coast of Tohoku earthquake (M 9.0): Coseismic fault model based on the dense GPS network data”. In: *Earth, planets and space* 63.12, pp. 1207–1211. DOI: `10.5047/eps.2011.07.016`. URL: `http://dx.doi.org/10.5047/eps.2011.07.016`.

Simons, Mark et al. (2011). “The 2011 magnitude 9.0 Tohoku-Oki earthquake: Mosaicking the megathrust from seconds to centuries”. In: *science* 332.6036, pp. 1421–1425. DOI: `10.1126/science.1206731`. URL: `http://dx.doi.org/10.1126/science.1206731`.

Song, Xi J and Donald V Helmberger (1996). “Source estimation of finite faults from broadband regional networks”. In: *Bulletin of the Seismological Society of America* 86.3, pp. 797–804.

Tan, Ying and Don Helmberger (2010). “Rupture directivity characteristics of the 2003 Big Bear sequence”. In: *Bulletin of the Seismological Society of America* 100.3, pp. 1089–1106. DOI: `10.1785/0120090074`. URL: `http://dx.doi.org/10.1785/0120090074`.

Toda, Shinji, Ross S Stein, and Jian Lin (2011). “Widespread seismicity excitation throughout central Japan following the 2011 M= 9.0 Tohoku earthquake and its interpretation by Coulomb stress transfer”. In: *Geophysical Research Letters* 38.7. DOI: `10.1029/2011GL047834`. URL: `http://dx.doi.org/10.1029/2011GL047834`.

Wei, Shengji, Robert Graves, Don Helmberger, Jean-Philippe Avouac, and Junle Jiang (2012). “Sources of shaking and flooding during the Tohoku-Oki earthquake: A mixture of rupture styles”. In: *Earth and Planetary Science Letters* 333, pp. 91–100. DOI: `10.1016/j.epsl.2012.04.006`. URL: `http://dx.doi.org/10.1016/j.epsl.2012.04.006`.

Yue, H and T Lay (2011). “Inversion of high-rate (1 sps) GPS data for rupture process of the 11 March 2011 Tohoku earthquake (Mw 9.1)”. In: *Geophysical Research Letters* 38.7. DOI: `10.1029/2011GL048700`. URL: `http://dx.doi.org/10.1029/2011GL048700`.

Zhan, Zhongwen et al. (2012). “Anomalously steep dips of earthquakes in the 2011 Tohoku-Oki source region and possible explanations”. In: *Earth and Planetary Science Letters* 353, pp. 121–133. DOI: `10.1016/j.epsl.2012.07.038`. URL: `http://dx.doi.org/10.1016/j.epsl.2012.07.038`.

Zhang, ZhuQi, John YongShun Chen, and Jian Lin (2008). “Stress interactions between normal faults and adjacent strike-slip faults of 1997 Jiashi earthquake swarm”. In: *Science in China Series D: Earth Sciences* 51.3, pp. 431–440. DOI: `10.1007/s11430-008-0023-6`. URL: `http://dx.doi.org/10.1007/s11430-008-0023-6`.

Zhao, Lian-She and Donald V Helmberger (1994). “Source estimation from broadband regional seismograms”. In: *Bulletin of the Seismological Society of America* 84.1, pp. 91–104.

Zhu, Lupei and Donald V Helmberger (1996). “Advancement in source estimation techniques using broadband regional seismograms”. In: *Bulletin of the Seismological Society of America* 86.5, pp. 1634–1641.

Chapter 3

RAPID ASSESSMENT OF EARTHQUAKE SOURCE CHARACTERISTICS

Lui, Semechah KY, Don Helmberger, Junjie Yu, and Shengji Wei (2016). “Rapid Assessment of Earthquake Source Characteristics”. In: *Bulletin of the Seismological Society of America* 106.6, in press. DOI: `10.1785/0120160112`. URL: `http://dx.doi.org/10.1785/0120160112`.

ABSTRACT

Recent studies emphasize the rapid assessment of earthquake source properties, such as moment magnitude, to help alleviate the impact of earthquakes. Depending on local crustal structure, earthquakes occurring at different depths can differ greatly in high frequency motions, which emphasizes the importance in constraining focal depth for the predictions of strong motions. For large earthquakes, assessing rupture directivity is also essential in estimating ground motion effects around the source region. In this chapter, we perform an in-depth study on a group of recent earthquakes near the intersection of the San Jacinto and San Andreas Fault systems in Southern California. We develop a systematic method to accurately estimate moment magnitude and focal mechanism within 3 to 6 s after the first P arrival. Focal depth can also be constrained within approximately 10 s upon the arrival of S waves. To determine the direction of fault rupture, we implement a forward-modeling method, which takes smaller events nearby as empirical Green's functions to simulate the rupture direction of the beginning motion generated by larger events. With a small event nearby, we resolve the rupture characteristic of the 2014 M_w 4.4 event using information at stations within 35 km from the epicenters, and successfully predict the ground motion response at stations at farther distances, where directivity effect is significant. Rupture direction of simulated earthquakes with larger magnitudes can also be accurately resolved using the method proposed, opening a possibility to predict ground motions ahead of time, in particular for hazardous regions.

3.1 Introduction

The increased seismic-station coverage associated with early warning and real-time seismology provides an opportunity to study strong-motion predictability. Early warning implies a prediction, that is, just what level of shaking is expected. In particular, many large earthquakes are preceded by foreshocks, and nearly all have aftershocks, some of which are quite damaging. Predicting the level of shaking for these smaller events with testable accuracy is hence fundamental in establishing creditability. In short, although treating earthquakes as centroid moment tensors proves effective at longer periods (>5 s), shorter periods (0.5–10 Hz) must be addressed in the strong-motion band, in which uncertainties in focal depth and rupture directivity become essential issues.

3.1.1 Small earthquakes as useful resources

Over the past decade, several earthquakes with $M_{\mathrm{w}} > 5$ occurred in the Southern California region, showing intriguing observations. Two of them are the M_{w} 5.4 Chino Hills event in 2008 (Figure 3.1) and the M_{w} 5.4 Brawley event in 2012 (Figure 3.1, inset). These moderate events have allowed in-depth studies, including their source and rupture characteristics (Geng et al., 2013; Hauksson et al., 2008; Wei et al., 2013). Interesting findings include the Brawley event being an indirect triggered source due to nearby fluid injection wells (Wei et al., 2015). With the earthquake epicenters located near a populated area, as well as the proximity of the Brawley earthquake to one of the geothermal energy production sites, there is high incentive to convey earthquake information as quickly and accurately as possible. Therefore, at the initial stage, we explored different methods to efficiently resolve the source characteristics, in particular the moment magnitude and focal mechanism. Instead of using the entire network to resolve focal mechanisms, we managed to recover reasonable results using the P arrivals at nearby stations. The first P wave of the Brawley event reached the closest station WLA within 3 seconds. With only a single station, focal mechanism could be recovered within 10 seconds and moment magnitude within 20 seconds. With both stations WLA and SNR, similar results can be recovered (Figure 3.2). For the Chino Hill event, with waveform at 4 stations, moment magnitude and focal mechanism converge to the full-array inversion results within 12 seconds after the first arrival. (The result for the Chino Hill event is included in Figure 3.A1.) These preliminary results motivate a systematic analysis to rapidly assess earthquakes characteristics for events at all sizes, including important source parameters, and to distill crucial information for

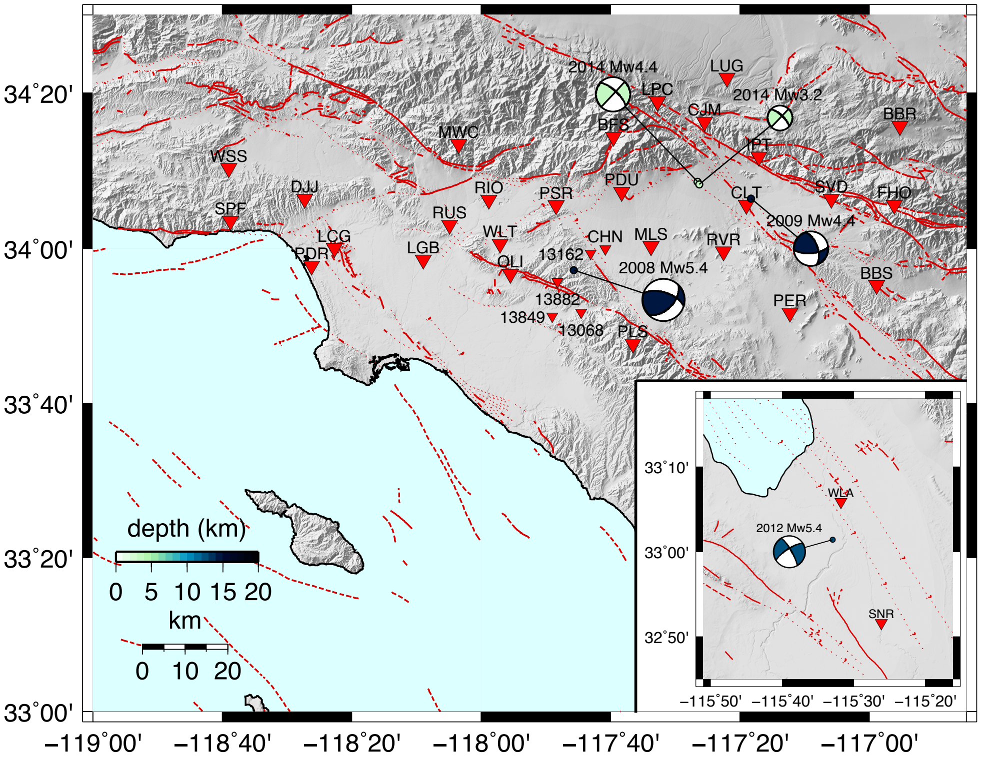

Figure 3.1: *Overview of the study region of this project near the city of Fontana located near the San Andreas Fault.* The Californian fault system is delineated by red dashed lines. Red triangles are selected CI network stations used extensively for this study. Circles are epicenter location of several prominent earthquakes in the study area, with colors representing their focal depths. (Inset) Local map showing 2012 M_w 5.4 Brawley event. Stations WLA and SNR are used in preliminary studies on real-time source characterization.

the necessary steps to implement in hazard mitigation.

3.1.2 Data from earthquakes near Fontana, CA as a test case

More recently, a number of earthquakes that occurred in Fontana, California, provide key data to address these issues. This region is located near the intersection of the San Andreas and San Jacinto faults and has been seismically active throughout the years (Figure 3.1), hosting earthquakes with a wide range of size and focal depth. The possible onset of a large rupture nucleation at the intersection of the two major faults may extend on either fault line and in either direction. At present, one of the major pressing concerns is the potential damaging response of the Los Angeles basin to any earthquakes occurring outside it and in particular at this intersection (Jones et al., 2008). Therefore, our investigation extends to retrieving rupture properties

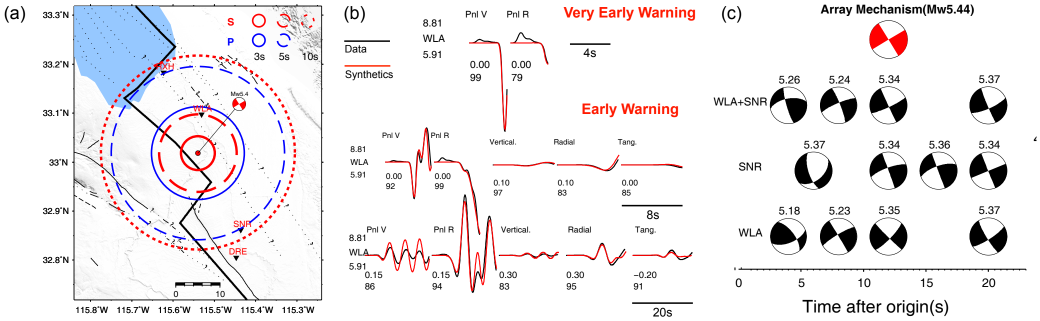

Figure 3.2: *Preliminary test on the 2012 Brawley event.* (a) Map view of event and station location with focal mechanism of the M_w 5.4 earthquake. The solid, dashed and dotted circles indicate the different arrival times of P and S waves, assuming the PCM velocity model (Wei et al., 2013). (b) Inversion results at station WLA with 4s, 8s and 20s of waveform are displayed. (c) The waveform inversion results reported as a function of waveform availability. The two nearest TriNet stations (WLA and SNR) were used separately and jointly.

of the earthquakes, including the rupture plane and the direction of rupture, which is crucial information in estimating the effects of the source to neighboring areas at all azimuths. We also aim to investigate the source and path effects of the corridor along the San Bernardino Valley and the LA Basin.

Two M_w 4.4 earthquakes near Fontana, which occurred in 2009 and 2014, respectively, are compared in our study. Their epicenters are less than 15 km apart, with similar moment magnitude (M_w 4.4) and strike-slip focal mechanisms. The only difference is focal depth, with the 2009 event occurring over 10 km deeper than the 2014 event. Intriguing observations can be identified - Focal depth plays a more significant role in contributing to the extent of shaking in the Basin area than expected (Figure 3.3). Although broadband waveforms show similar amplitude range, the deep event has much higher energy content when waveforms are filtered to a frequency range of 3-10 Hz at station RUS, which is located at the edge of the Los Angeles basin. In this frequency range, a wide range of buildings will be significantly affected. This phenomenon is found consistent at nine other stations spanning approximately 80 km from east to west along this narrow corridor (Figure 3.A2).

In short, focal depth plays a more significant role in contributing to the extent of shaking in the basin area than expected. Currently the earthquake early warning (EEW) algorithm focuses on retrieving the correct epicenter location and moment magnitude with 3 seconds of waveforms (Kanamori, 2005; Wu and Kanamori, 2005, 2008). These intriguing observations further emphasize focal depth being an

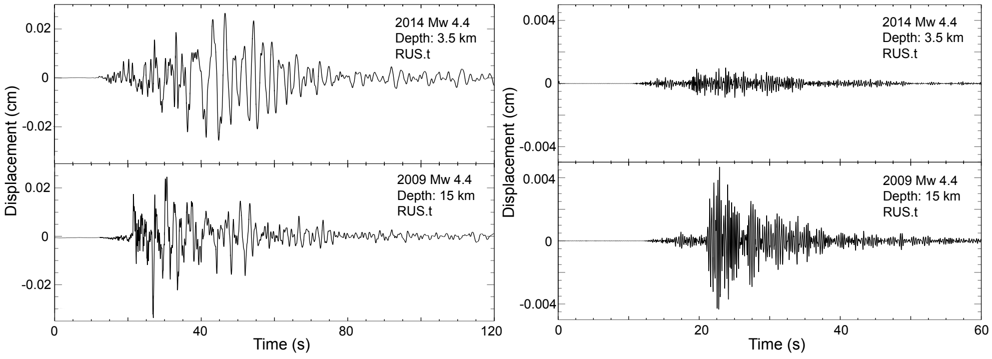

Figure 3.3: *Significant difference in energy content for earthquakes at different focal depths.* The tangential responses at station RUS near downtown Los Angeles, at a distance of I) 60 km for shallow event and II) 72 km for the deep event. Broadband waveform (left) indicates the strong late phase (8s back) for the deep event, which is likely sSmS (Helmberger et. al., 1993). The high frequency energy radiation is also much stronger (a factor of 5) for the deep event (right).

important source parameter to constrain.

For all the reasons above, we select earthquakes near Fontana as test cases to perform a comprehensive and systematic analysis in characterizing earthquake source and rupture properties, including moment magnitude, focal mechanism and depth, and rupture direction and dimension, using close-by stations. Besides aiming to quickly extract information from real-time data, we also investigate how accurately we can further predict ground motion at farther distances, based on these results.

3.2 Methodology

In this study, the cut-and-paste (CAP) method is the primary tool to model waveforms recorded at selected station (Zhao and Helmberger, 1994; Zhu and Helmberger, 1996). This approach compares the Pnl and surface wave segments separately with waveforms from a synthetic source. Since differential time shifts are allowed among the different segments of the complete wavefield, it results in accurate source estimates even with synthetic Green's functions generated from imperfect 1D velocity models or poorly located events. Here we compute the Green's functions using a frequency-wave number integration method (Zhu and Rivera, 2002), and the CAP approach determines via grid search the optimal moment magnitude, conjugate fault planes, and focal depth. Typically, depth is constrained by the surface wave-to-body wave amplitude ratio, as well as by depth phases in the Pnl wave trains.

To resolve rupture characteristics of these events, we follow the approach developed by Tan and Helmberger, (2010), a modeling technique that utilizes both duration and amplitude information to estimate rupture directivity. In their analysis, a small nearby event is selected as the empirical Green's functions (EGFs) event. A grid search is conducted to solve for a common rise time τ_r and rupture duration time τ_c at individual stations that minimize the total waveform misfit error

$$e = \sum_{i=1}^{N} [d_i(t) - \Delta M_0 g_i(t) * (\tau_r * \tau_{ci}), \tag{3.1}$$

in which $d_i(t)$ and $g_i(t)$ represent records from the target event and the EGF event, and ΔM_0 is a scaling factor to account for the two events being different in size (and radiation pattern, if applicable). τ_r and τ_c are rise time and rupture duration respectively, and $\tau_r * \tau_c$ gives the relative source time function (STF) of the target event with respect to the EGF event. The summation is over all the selected stations. In the simple scenario of unilateral horizontal rupture on a vertical fault, the variation of τ_c can be modeled with

$$\tau_c = \frac{fl}{V_r} - \frac{fl}{v_{p,s}} cos(\varphi - \phi), \tag{3.2}$$

in which fault length (fl) and rupture speed (V_r) can be easily estimated. φ and ϕ are the rupture propagation direction and the station azimuth respectively. In the 2003 Big Bear sequences, the a priori Haskell source model facilitates estimation of rupture parameters such as fault length (fl) and rupture speed (V_r). This method has been successfully implemented in another study by Luo et al., (2010) on the widely felt Mw 4.6 earthquake in Inglewood, CA. They used aftershocks as EGFs and retrieved rupture directivity of the mainshock directing to the southeast, which is consistent with the orientation of the Newport-Inglewood fault (Figure 3.A3). Another approach to study rupture characteristics is to use EGF based on the generalized ray theory (Helmberger, 1983). The target event is simulated by a summation of EGF events assumed as point sources, with each of them varied by a small time variance, depending on their shift in horizontal and vertical direction from the original point source. (For details, see Appendix A of Chapter 2). Previously, we have used this approach to simulate the rupture properties of an intra-slab event in the Tohoku-Oki region with an aftershock that occurred at a similar location (Lui et al., 2015).

3.3 Analysis and Results

Three Fontana events are selected for our analysis. The two Fontana earthquakes mentioned in section 1.2 are subjected to detailed comparison as we determine their source characteristics using the CAP method. The two epicenters are approximately 13 km apart, with the deep event slightly to the east. We also selected the biggest aftershock of the shallow event in 2014, with M_w 3.2 and at a similar location, to be the EGF event for studying the directivity of the M_w 4.4 event. Note that the two events need not have the same mechanisms but their source parameters must be determined by other means, i.e. CAP, from stored data sets. Mechanisms can be determined down to $M_w = 2$ using the method applied in Tan and Helmberger, (2007). Such a library can be generated for many locations in Southern California given our level of seismicity.

3.3.1 Real-time assessment of source parameters

For the purpose of comparison, we first model the waveforms of the two events with a bigger group of CI stations in the Southern California Seismic Network (SCSN), within an epicentral distance of 500 km. Inversion is done up to 0.2 Hz for Pnl waves and up to 0.1 Hz for surface waves. With CAP inversion, the strike/dip/rake values for the shallow and deep events are 44°/88°/31° and 81°/70°/82° respectively, and their focal depths are 3.5 and 14.5 km respectively (Figure 3.A4). (These parameters will be called "network mechanism" and "network depth.") Results are similar to what is reported in the SCSN catalogue, in which the 2014 shallow and 2009 deep events have strike/dip/rake/depth (units: °/°/° km) values at 33/87/26/3.6 and 83/73/22/14.2 respectively.

With accurately determined source characteristics, the next step is to investigate how quickly and accurately these results can be obtained within a short time after an earthquake occurs, on the order of seconds after the first P arrival. For the 2014 shallow event, we selected a group of six nearby stations, which are within an epicentral distance of 20 km and form a close ring of seismic recording for the shallow event, providing good azimuthal coverage (Figure 3.4). The P wave reached these stations within 4 s after the origin time, whereas the S wave arrived at the stations within 8 s. By applying CAP on waveforms recorded at only these six stations, source parameters evolve as more and more seismic data are available for inversion. Eventually all parameters match with the network mechanism.With only 3 s of incoming waveform, strike and dip inversions are already within 10° from the network mechanism (Figure 3.5a). The waveform cross correlations are also

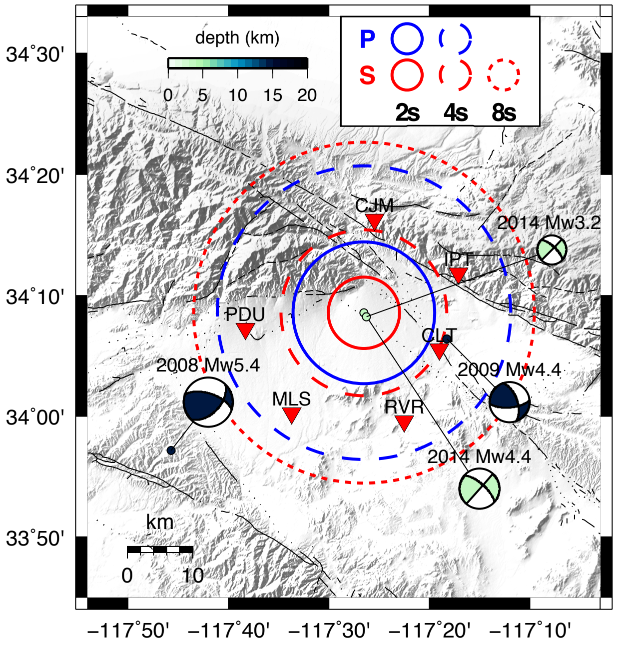

Figure 3.4: *Stations near the epicenters are selected for rapid assessment of source parameters.* Circles (solid/dashed/dotted) represent the arrival of P and S waves at 2, 4, and 8 s after the origin time. Within 4 s, P wave has reached the six closest stations (triangles) within 4 seconds.

above 90% for most of the vertical and radial components at stations. Furthermore, moment magnitude differs by less than 0.1 from the network inversion estimate. Because focal depth can only be accurately determined after the arrival of S waves, we only assume an average hypocenter depth in the area (~7 km) for the 3 and 6 s inversion. With 10 s of waveform, including the incoming S phase, we then also perform a grid search on focal depth. For the deep event in 2009, a slightly different group of stations are selected, due to the difference in event location. Station CLT is clipped in this case, given its <2 km distance from the source. Nonetheless, a similar level of accuracy is obtained from the inversion (Figure 3.5b). The 2014 and 2009 earthquakes are constrained at a depth of 3.5 and 14 km, respectively, which are almost identical with network depth. As a check, we reran the 3 and 6 s inversion with the updated focal depths, and similar results are obtained. This indicates that preliminary seismic moment and focal mechanism estimates are not heavily dependent on focal depth as demonstrated in Figure 3.5.

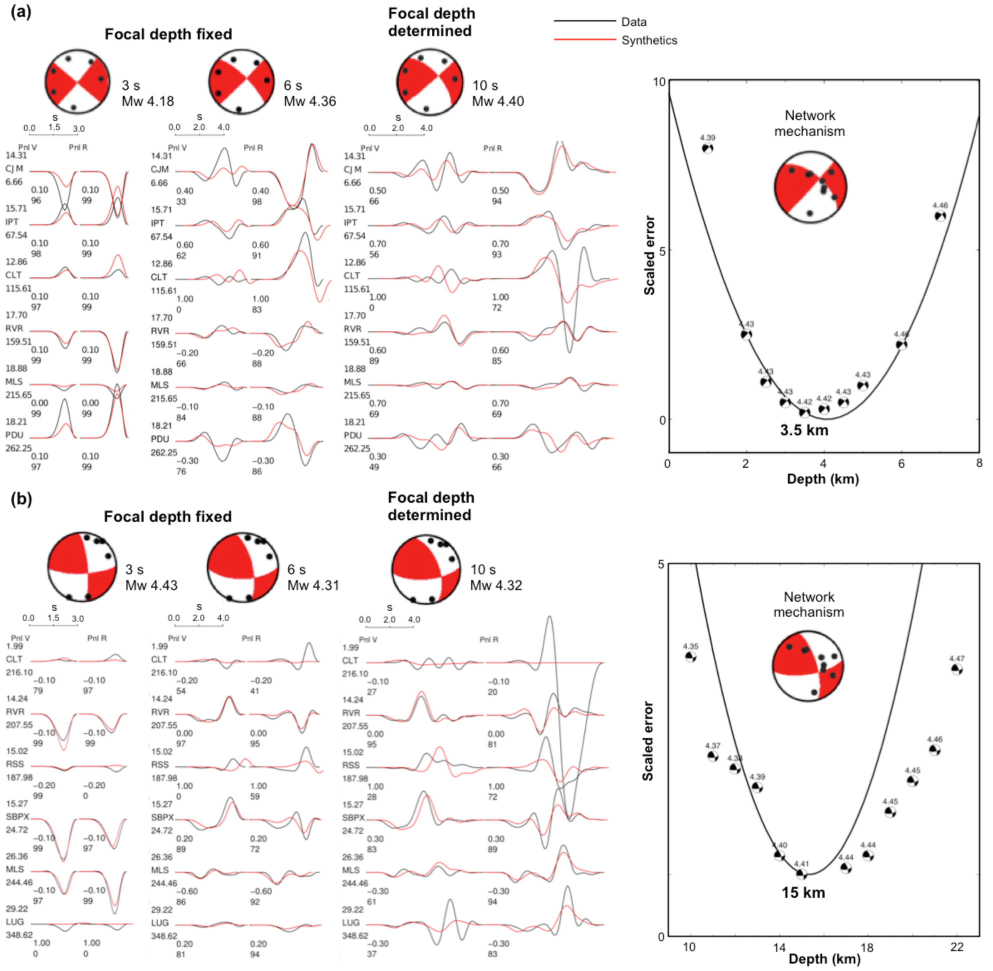

Figure 3.5: *CAP allows accurate and fast characterization of moment magnitude, focal mechanism and depth.* (a) Inversion with 3s, 6s and M_w = 4.4. The figure to the right displays scaled errors from grid search on focal depth. Focal depth can be determined once S wave arrives (within 10 s in this case). Before the S wave arrival, a focal depth (h = 7 km) is assumed when conducting inversions. (b) Analogous inversion results for the deep 2009 M_w 4.4 event.

3.3.2 Assessing rupture properties

Although source mechanism and focal depth can be well determined within 10 s after the first arrival, for much larger earthquakes, it is also important to obtain information regarding the rupture direction and dimension with growing moment magnitude. In the same area near Fontana, a M_w 3.2 aftershock occurred at almost the exact same location and similar depth as the shallow M_w 4.4 event. Waveform of this smaller event is similar to the M_w 4.4 event (see Figure 3.A5, available in the electronic supplement to this article), and the two earthquakes also share very similar focal mechanism according to the SCSN catalogue. Since directivity effect lessens with decreasing magnitude, the M_{w} 3.2 event is assumed to act like a point source compared to the target event. We compare the amplitude ratio of the first 2 s of vertical and radial P arrivals for the M_{w} 4.4 and 3.2 events at stations at all azimuths. Our results indicate that the ratio is much higher at stations to the northwest. This preliminarily suggests the M_{w} 4.4 earthquake ruptured towards that direction (Figure 3.6).

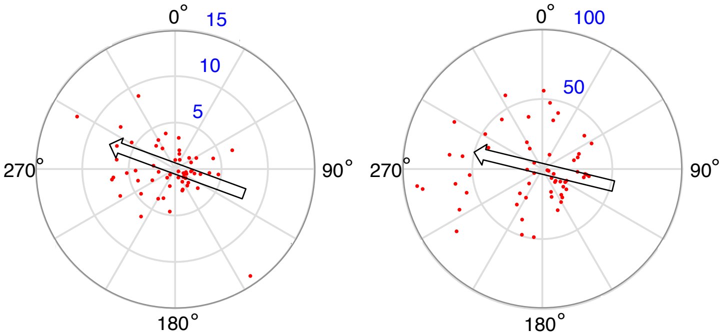

Figure 3.6: *Directivity observed from difference in amplitude ratio of waveform across all azimuths.* Using a smaller event near the main shock, we compare the vertical (left) and radial (right) component amplitude ratio of the first 2.5 seconds of P waves between the big and small events, as a function of azimuth. In the radial plot, each dot represents one station. Waveforms are filtered to 0.5 - 2 Hz. The scale on the concentric circles is the amplitude ratio. The main shock carries much higher energy to stations to the west and northwest, providing an early indication of rupture directivity.

With this hypothesis, we then follow the forward modeling approach in Tan and Helmberger, (2010) and model the directivity of the M_{w} 4.4 event using the M_{w} 3.2 earthquake as the EGF event. EGFs are generated by convolving the first 3 s of P wave with a range of STFs, which have rupture duration τ_c ranging from 0.1 to 0.5 s and a best-fitting rise time τ_r at 0.1 s. Note that τ_r is insensitive in this study and it is fixed at 0.1 s in real time analysis. P waves used for the inversion are filtered to 0.5-4 Hz. ΔM_0 is 63 in this case, accounting for the moment ratio between the two events. Results indicate a distinct variation of best-fitting STF across azimuth (Figure 3.7). Station CLT, which is to the southeast of the epicenter at an azimuth of 114°, fits best with rupture duration (τ_c) of 0.45 s. On the other hand, station LPC is located in the opposite direction with an azimuth of 333°, and τ_c = 0.15 s fits best. For stations in other azimuths, τ_c is between 2.5 and 3 s. The analysis validates the hypothesis that the M_{w} 4.4 earthquake ruptured toward northwest. This result

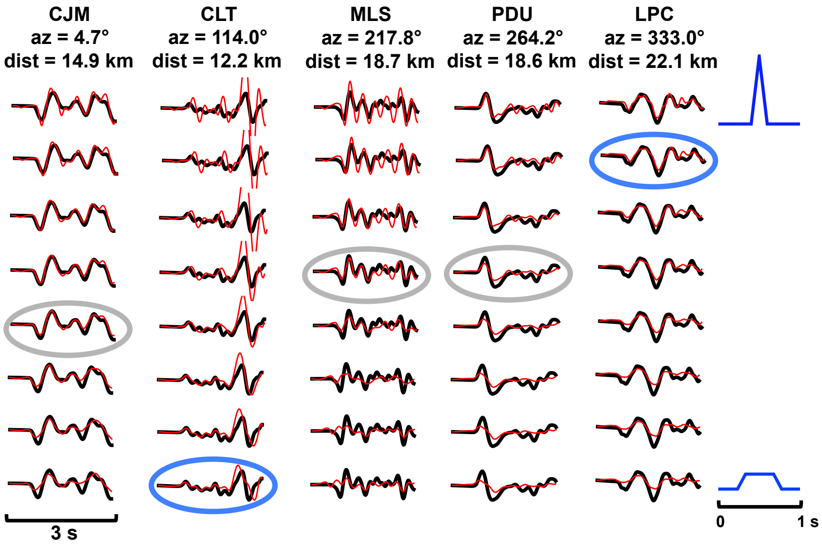

Figure 3.7: *Predicting rupture directivity using incoming P-wave.* Each column represents comparison of main shock data at a station (radial component) with a range of EGFs, which is the convolution of aftershock data with a specific source time function. The best-fitting pairs are circled. Note the variation across azimuth in the fit between data (thick lines) and EGFs (thin lines). The extreme cases at stations CLT and LPC suggest a rupture directing to the northwest. Refer to Figure 3.A6 for the results of all the remaining stations.

is further validated when we include in the analysis the first arriving P waves at all the triggered CI stations (Figure 3.A6). The values of τ_c have a smooth variation with the maximum and minimum value corresponding to azimuths 120° and 305° (Figure 3.8). The sensitivity of this analysis with waveform frequency is low, as we obtain similar results using waveforms filtered up to 2.5 Hz, 4 Hz and 10 Hz (Figure 3.8). A rupture direction of az = 305° is very similar to the strike value of one of the conjugate planes for the shallow event (strike = 313°). Based on results from the P-wave analysis and the assumed 1D model, the estimated rupture length and rupture speed are 0.8 km and 2.9 km/s respectively, according to Equation 3.2.

3.4 Discussion

The methodology proposed here allows a quick characterization of seismic moment, focal mechanism and depth, and rupture properties with the first P and S arrivals at stations within 35 km from the epicenter, which is less than 10 s of seismic data. Here, we will discuss how these data can be used to predict ground motions at more distant stations. Essentially, this is opposite of the study by Luo et al., (2010), which predicts near-in effects from distant stations.

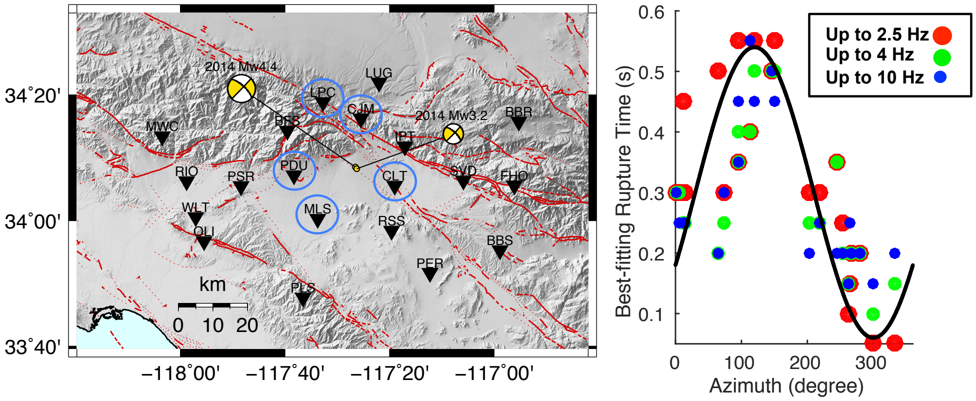

Figure 3.8: *Sensitivity test of waveform at different frequency bands.* (Left) A map view showing all the stations included in this analysis. The five stations circled are selected for rapid directivity estimation using the first 3 s of P waves, and the result is similar to when we include all the stations. (Right) We obtain similar analysis results when using waveforms filtered to different frequency bands (up to 2.5, 4, and 10 Hz).

3.4.1 Predicting the effect of directivity at farther stations

Based on the directivity analysis of P waves, one can further estimate the site response. Here we use broadband velocity tangential component for this test as SH waves are generally regarded as the more destructive phases at stations with larger epicentral distances, although other components work equally well. We select 4 stations at approximately 50 km away from the source. Stations CHF and WLT are in the direction of rupture, while stations BBS and MSJ are away from it (Figure 3.9). Predicted waveforms are simulated by convolving the M_w 3.2 event with a STF calculated from Equation 3.2, based on the estimated rupture speed and direction from the P-wave analysis, as well as an assumed S-wave velocity (V_s) of 3.18 km/s at this depth, according to the 1-D velocity model used in this study (Table 3.A1). Our simulation produces excellent fits between predicted waveforms and the M_w 4.4 data at all four stations (Figure 3.9). For comparison, we also assume a rupture in the reverse direction (to the southeast) and simulate the corresponding waveforms (dashed line). A much worse fit results. The effect of directivity is mostly revealed in the waveform amplitude rather than the pulse shape, but our simulations indicate that it is possible to quickly predict responses at larger distances provided that there are smaller events nearby available as EGF events for path corrections. The prediction of S waves based on a calibrated STF is also validated by a grid search on a range of trapezoidal STFs (Figure 3.A7). The best-fitting EGFs are very

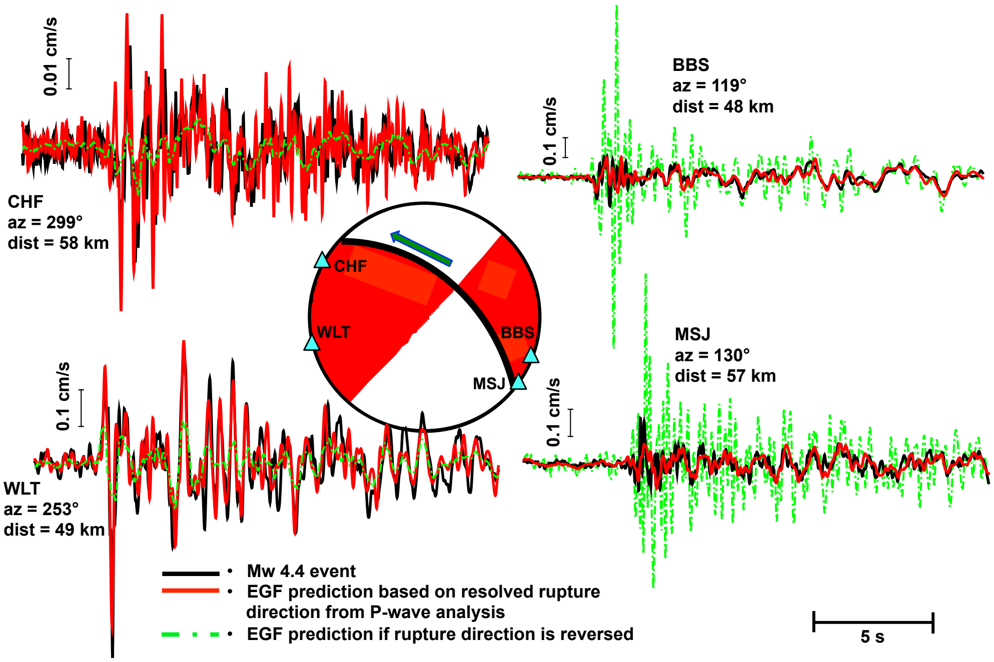

Figure 3.9: *We can predict the amplitude of S-wave arrivals based on the P-wave directivity analysis.* With estimated rupture length and velocity, one can compute the source time function of S waves and generate the prediction of site response for SH waves (tangential component). Four stations are selected in this test, which are at different ends of the rupture plane. Rupture direction is indicated by the arrow. Waveform predictions have excellent fit with the M_w 4.4 data. Dashed lines with significant differences in predictions occur if the rupture directions are reversed.

similar to those generated from the calibrated STF. Moreover, we are able to apply the same method and predict Rayleigh wave motions (Figure 3.A8). Note that when we choose a smaller event for EGF modeling, the differences in focal mechanisms are allowed, as demonstrated by Tan and Helmberger, (2007). Focal depth, however, remains an essential factor in levels of shaking.

3.4.2 Implications for earthquake early warning and Shake Map

The extent of ground motion depends on both the direction of fault rupture and local geological materials. With the complicated tectonics in Southern California, path effect plays a particularly important role in ground-motion prediction. Shallow events often generate secondary surface waves that follow the soft 3D tracks near the surface, as demonstrated in a study by Savage and Helmberger, (2004) on the wave propagation through the Salton Trough. Such motions are difficult to model because they are often highly path-dependent, as pointed out by Carl Tape (personal communication, 2015), who performed extensive inversions of crustal surface waves. As a result, the EGF approach proposed here has significant advantages, as numerous small earthquakes are available in the region containing specific wave path information. Work can begin on building a EGFs library consisting of earthquakes in Southern California. As an earthquake occurs, the library allows immediate identification and processing of a smaller event with similar location and depth, at the same time generates site-response predictions at greater distances when rupture properties of the main event become available and before seismic energy propagates into the area. Note that our methodology is particularly useful in predicting Shakemaps and "Did you feel it?" information due to aftershocks, which make a significant impact on populated regions as well as building responses. For example, the deep event received five times more reports than the shallow event (USGS Community Internet Intensity Map) as expected from Figure 3.3.

In July 2015, a M_{w} 4.1 earthquake occurred at a similar location in Fontana, at a depth of 5 km. Together with the shallow event in 2014, they have both triggered building responses in a 9-story high-rise in Pasadena and a 15-story high-rise in downtown LA, which are over 70 km from the epicenters (Monica Kohler, personal communication, 2016). Currently the EEW algorithm estimates the expected ground-motion intensity based on constrained earthquake location and seismic moment with 3 s of P waves at nearby stations (Kanamori, 2005; Wu and Kanamori, 2005, 2008). While these are of obvious values, accurate estimation of focal mechanism, depth, and rupture direction, besides being valuable information for early warning and the formulation of shake maps, will also be crucial for the engineering community to improve building response predictions.

3.4.3 Impact of large earthquakes

Exploring the scalability of this methodology is a subject of our ongoing research, taking advantage of station densifications. To understand the behavior and predictability of larger earthquakes, which occur much less frequently, it requires realistic simulation of Green's functions. Deterministic and empirical methodologies are both used to generate events of greater size. As a test case, we take the latter approach and use available intermediate-sized earthquakes as empirical Green's functions to simulate still bigger events. The big event is assumed to be a finite-fault earthquake, represented by the summation of a number of smaller events (Song et al., 1995, a study on the M_{w} 6.7 Northridge earthquake in 1994). Here the M_{w} 4.4 shallow event near Fontana is summed 32 times to represent a M_{w} 5.4 earthquake, with a rupture length of 2.8 km and rupture velocity of 2.9 km/s. Each point source is shifted by a small amount of time and adjusted for depth based on generalized ray theory, and in each test case they are aligned differently to model various rupture directions (Figure 3.10a; (Helmberger, 1983; Song and Helmberger, 1996)). Notable differences in waveform amplitude and pulse shape can be seen at stations

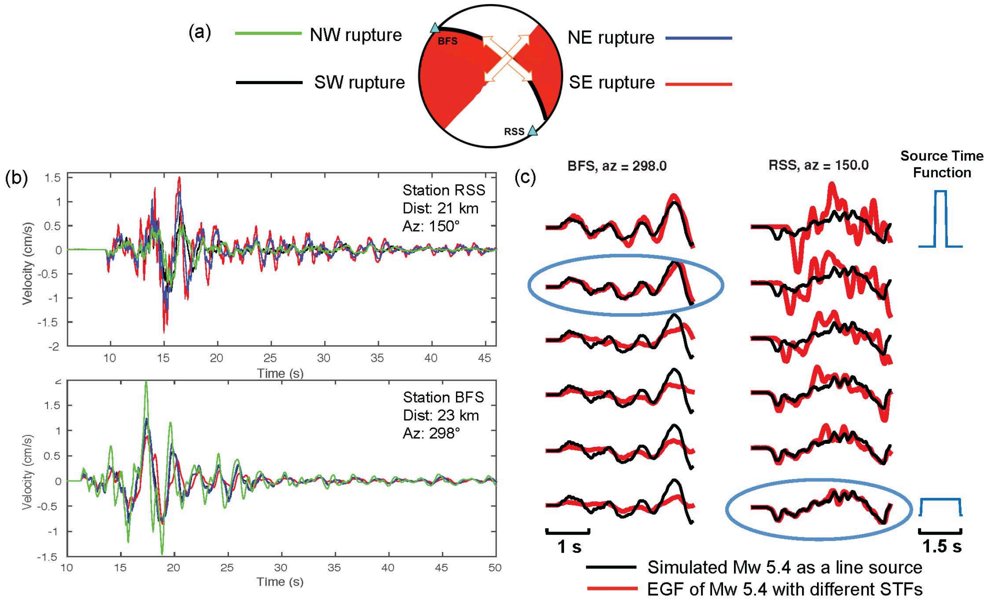

Figure 3.10: *Simulating Green's functions of larger earthquakes using the EGF approach.* (a) An finite-fault earthquake with M_w 5.4 is represented by a summation of 32 point sources with M_w 4.4. Ruptures are simulated in 4 directions as indicated by the arrows. (b) Broadband empirical Green's functions of the M_w 5.4 event at stations RSS (to the southeast) and BFS (to the northwest). (c) Result of directivity test with the M_w 5.4 synthetic waveforms (shown in 10b) treated as real data. The best-fitting pairs are circled. Resultant STFs are in agreement with the simulated rupture direction (northwest).

away from and in the direction of rupture. For full broadband records, waveform amplitude differs by a factor of two depending on the azimuth of the stations from the earthquake source (Figure 3.10b). Treating the line-source synthetic waveforms as real data, we then proceed with the directivity test as described in the previous section to resolve for corresponding source-time functions using the first 3 s of P waves. Here we use one of the M_w 5.4 event simulations with rupture directing to northwest. The resultant STFs are in excellent agreement with the assigned rupture direction (Figure 3.10c). Waveform at station RSS, which is away from the rupture, fits best with a broad STF, while station BFS, which is in the rupture direction, fits best with a tall and narrow STF. This marks as a good validation of our method and implies that the EGF library can be extended to earthquakes with M_w larger than those in the existing catalog, further enhancing ground-motion estimations in real time when a big earthquake hits.

The methodology proposed in our study is useful in determining source characteristics of intermediate-sized events. Challenges will arise, nonetheless, as the earthquake grows larger in size and complexity, i.e. at larger M_w, the Pnl wave train spans in a longer time window and the later phases will overlap with the first arrival of the direct S wave. This adds complexity to the methodology, as it is difficult to separate the effects of multiple phases that arrive at the same time. At this point, one has to utilize a ring of stations that are slightly farther from the epicenter. This inevitably increases the time required to determine source characteristics, but the additional source information will still be beneficial for assessing what is happening as well as early responses. Although not discussed here, we are generating valuable information about the broadband rupture properties of earthquakes for use in numerical simulations at higher frequencies.

3.5 Conclusion

To summarize, we propose a systematic procedure that allows rapid assessment of the source characteristics and rupture properties of earthquakes. A test case using earthquakes near Fontana, CA is successful in recovering moment magnitude, focal mechanism, and focal depth of the earthquake within 10 s after the first P-wave arrival. Rupture directivity can also be estimated from the first 3 s of P waves using forward modeling of EGFs. Once rupture properties are constrained, the ground-motion response for the stronger S waves that arrive later can be accurately predicted using EGFs in areas at farther distances. This set of methodology can potentially improve the effectiveness of the Earthquake Early Warning system, contributing to the mitigation of seismic hazard.

3.6 Appendix A: Supplementary Information

This supplement includes 8 figures and 1 table. Figure 3.A1 displays results from a preliminary study on the 2008 Chino Hills earthquake. Figure 3.A2 and 3.A4 show the comparison of waveforms for the two M_w 4.4 events near Fontana recorded at stations along the corridor between the San Bernardino Valley and the LA Basin, and the complete Cut-and-Paste inversion results of them. Figure 3.A3 shows the results of a previous study on the M_w 4.6 Inglewood earthquake inside the LA Basin. Figures 3.A5 to 3.A8 are related to the directivity and ground-motion prediction analysis. Table 3.A1 refers to the crustal model used for this study.

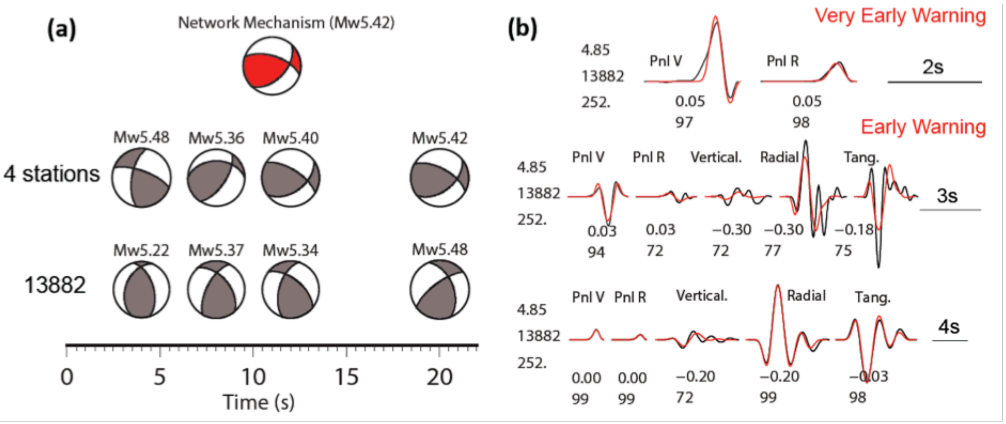

Figure 3.A1: *Preliminary study on the 2008 Chino Hills earthquake.* (a) Waveform inversion as a function of time after the first P-wave arrival at close-in stations. Inversions were performed using four nearest stations and one station (13882) respectively. (b) Waveform comparison for station 13882 at 4s, 8s and 12s.

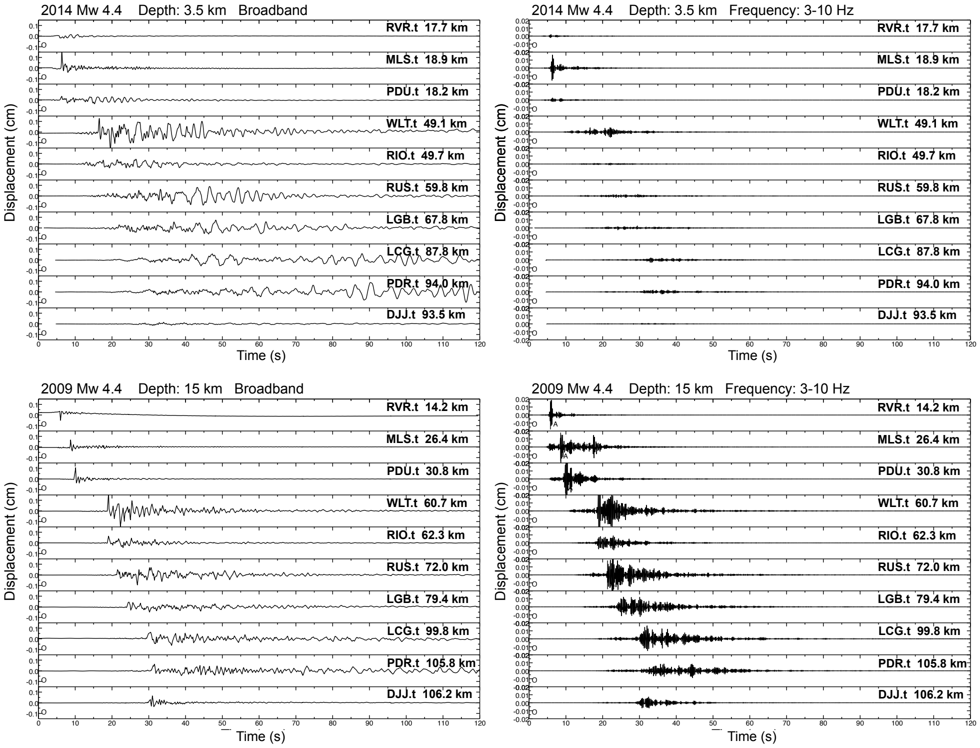

Figure 3.A2: *Waveform recorded at stations within the LA Basin.* (Top row) Shallow event near Fontana, CA in 2014. (Bottom row) Deep event near Fontana, CA in 2009. Note the significant difference in energy content between (Left column) broadband waveform and (Right column) waveform filtered at high-frequency (3-10 Hz).

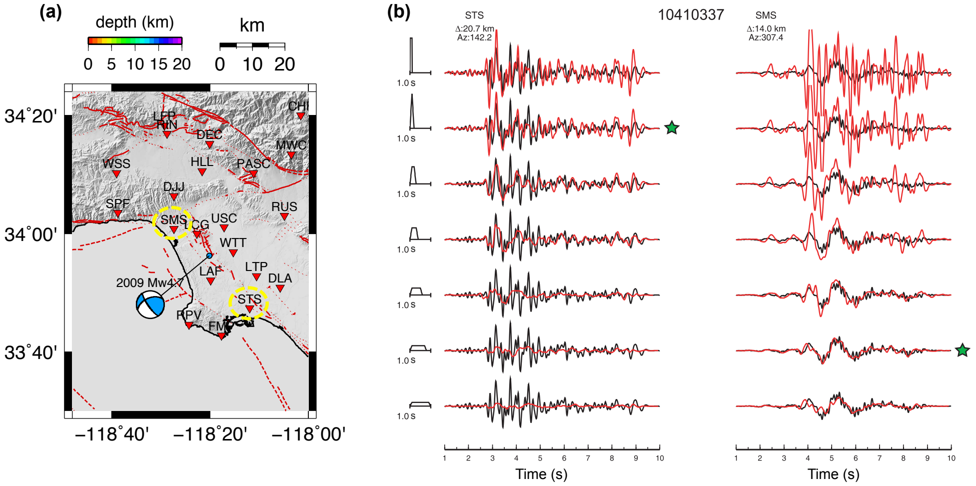

Figure 3.A3: *The study on the Inglewood M_w 4.6 earthquake by Luo et al (2010).* (a) Map showing the location of the two stations STS and SMS. (b) Reprinted figure from Luo et al. (2010), which shows the directivity validation test by using various trapezoidal source time functions to simulate the main event (10410337), with the predictions at both stations with a green star.

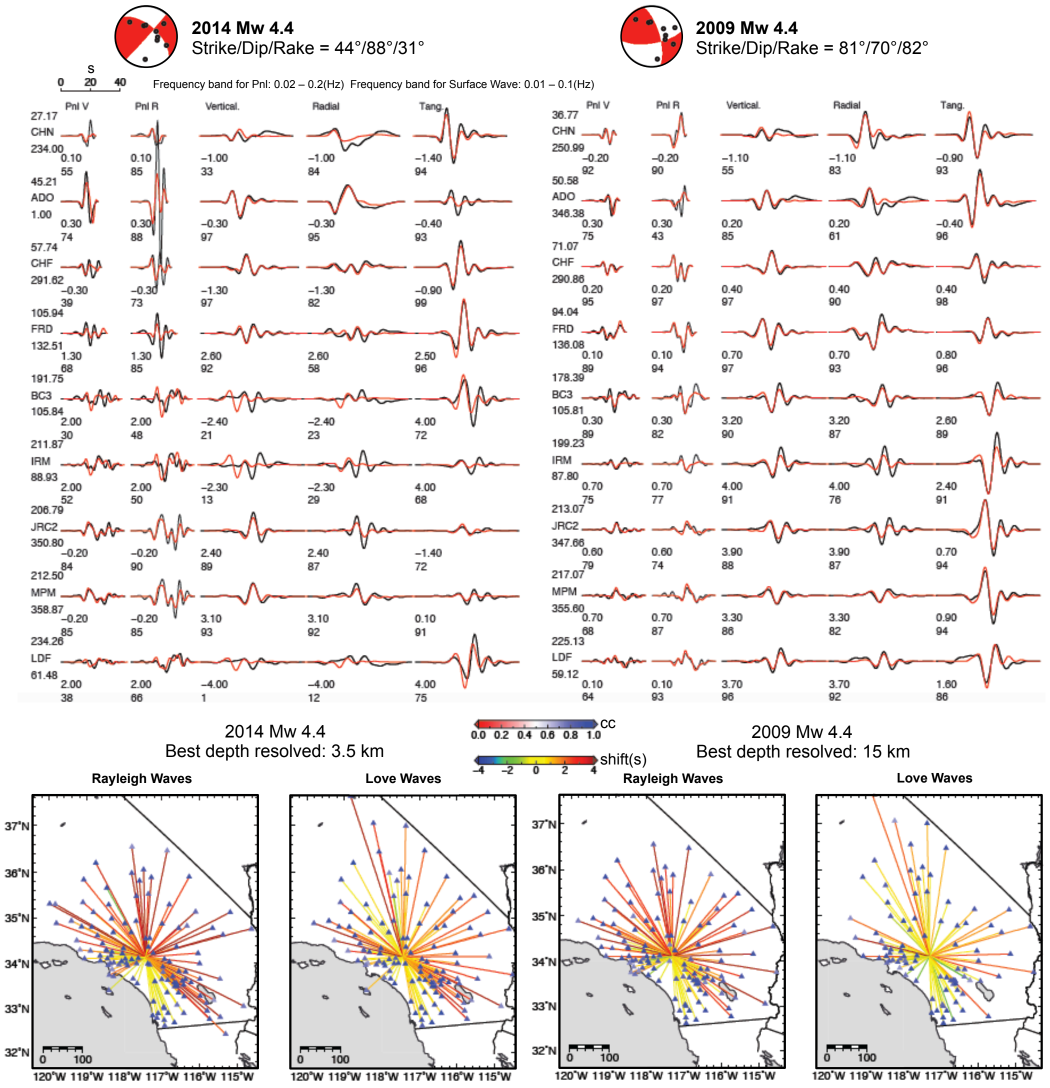

Figure 3.A4: *Waveform inversion of the two events using the whole network.* (Top) Waveform comparison between data (black) and 1D synthetics (red) at selected stations. The two rows of numbers below the seismogram represent (top) timing shift (in second) of the synthetic waveform relative to the data and (bottom) cross-correlation value. (Bottom) Spider diagrams show the timing shift (line color) and cross-correlation (triangle color) between data and 1D synthetics at each station. When comparing waveform cross-correlations at various stations, for those with cross-correlations values above 70%, Rayleigh waves show similar time-shift values (lines in dark orange) for both events. Time-shift values for Love waves differ slightly more, but it can be concluded that the lateral location of the earthquakes is reliable. This also validates the 1D velocity model used to generate the Green's functions at these periods for hard-rock sites.

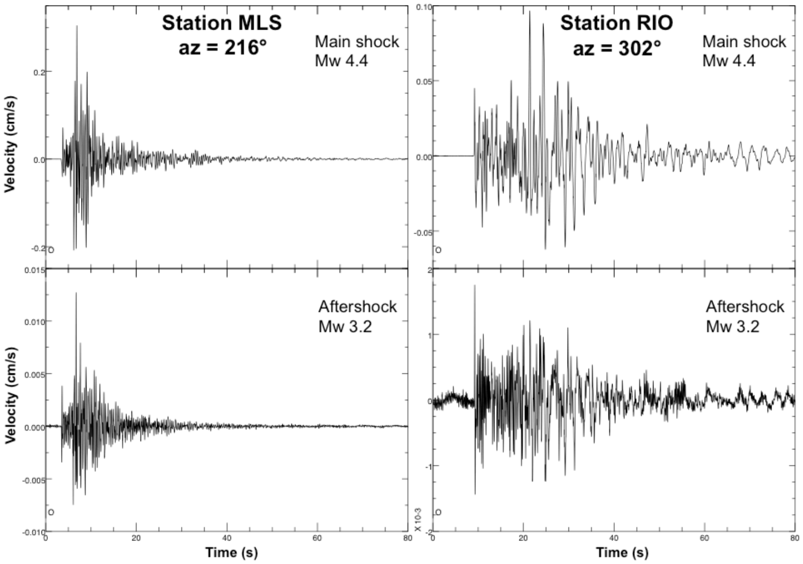

Figure 3.A5: *Small event can be used as EGFs for studying directivity.* The M_w 4.4 shallow earthquake and its biggest M_w 3.2 aftershock have almost identical epicenter locations, as well as similar velocity waveform.

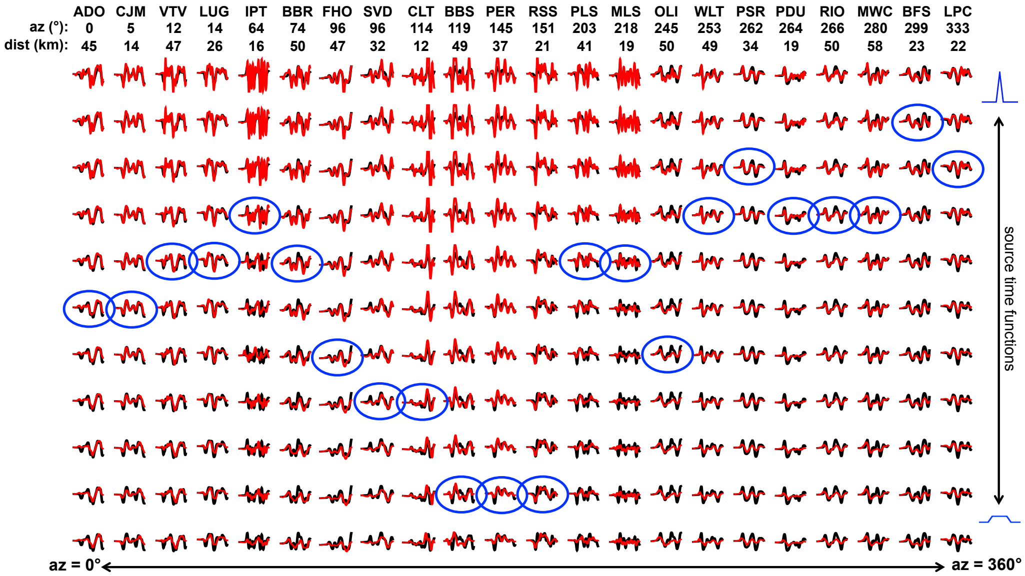

Figure 3.A6: *Detailed results of the directivity analysis with 3 s of incoming P wave.* A range of source-time functions (STF), which are used to generated empirical Green?s functions (EGFs) - convolving with the small event data. Each column represents waveform comparison at each station between data and different EGFs. This analysis includes all CI stations triggered during the small event. Circled are ones with the lowest misfit. Note that stations BBS, PER, and RSS (southeast) and station BFS (northwest) have the best fit with the flattest and sharpest STF respectively, including rupture directing to northwest.

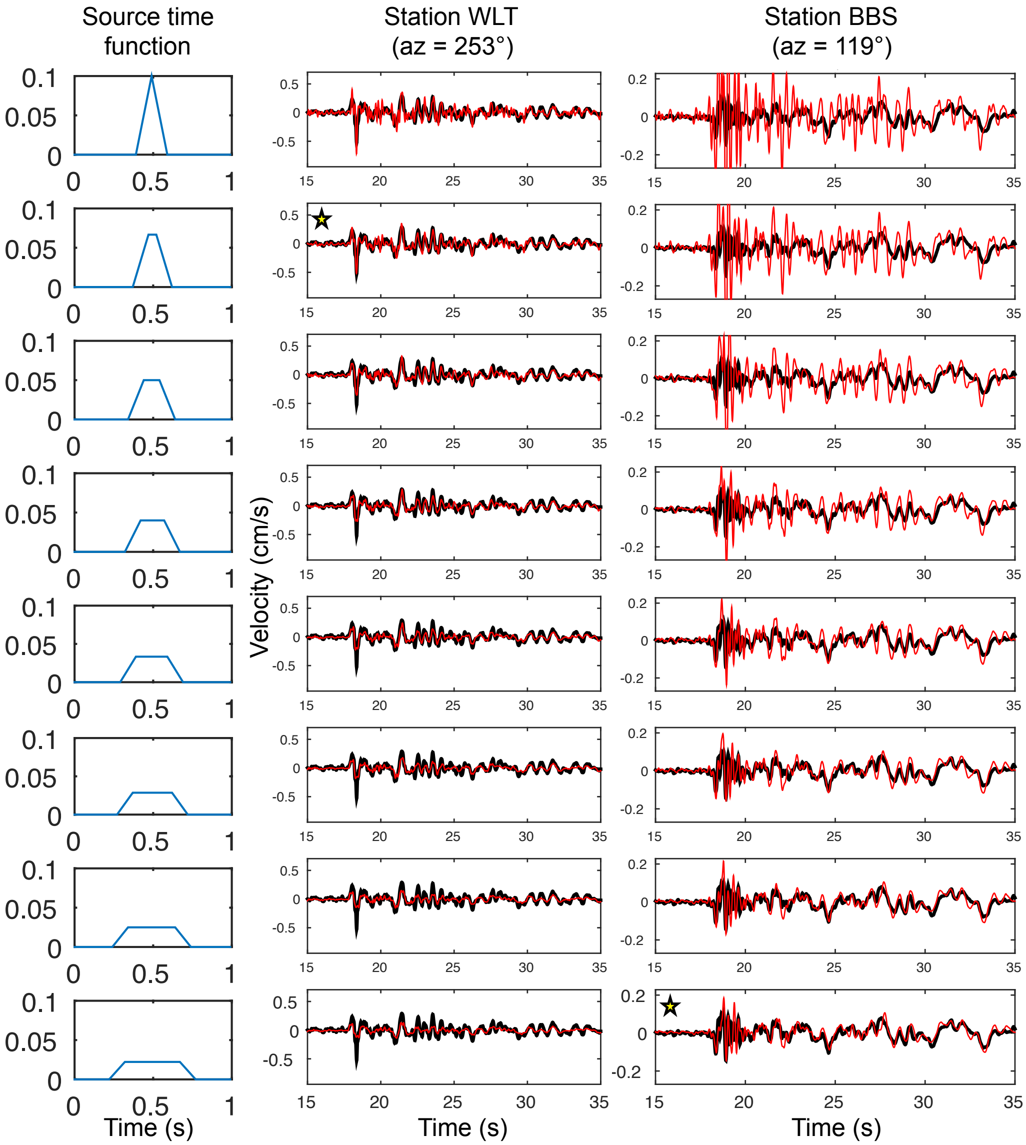

Figure 3.A7: *Validating the ground-motion prediction test with the EGF approach.* We use different trapezoidal source time function to generate EGFs and fit them with the SH waves of the M_w 4.4 shallow event. Yellow stars indicate the best fit between EGF (red) and data (black).

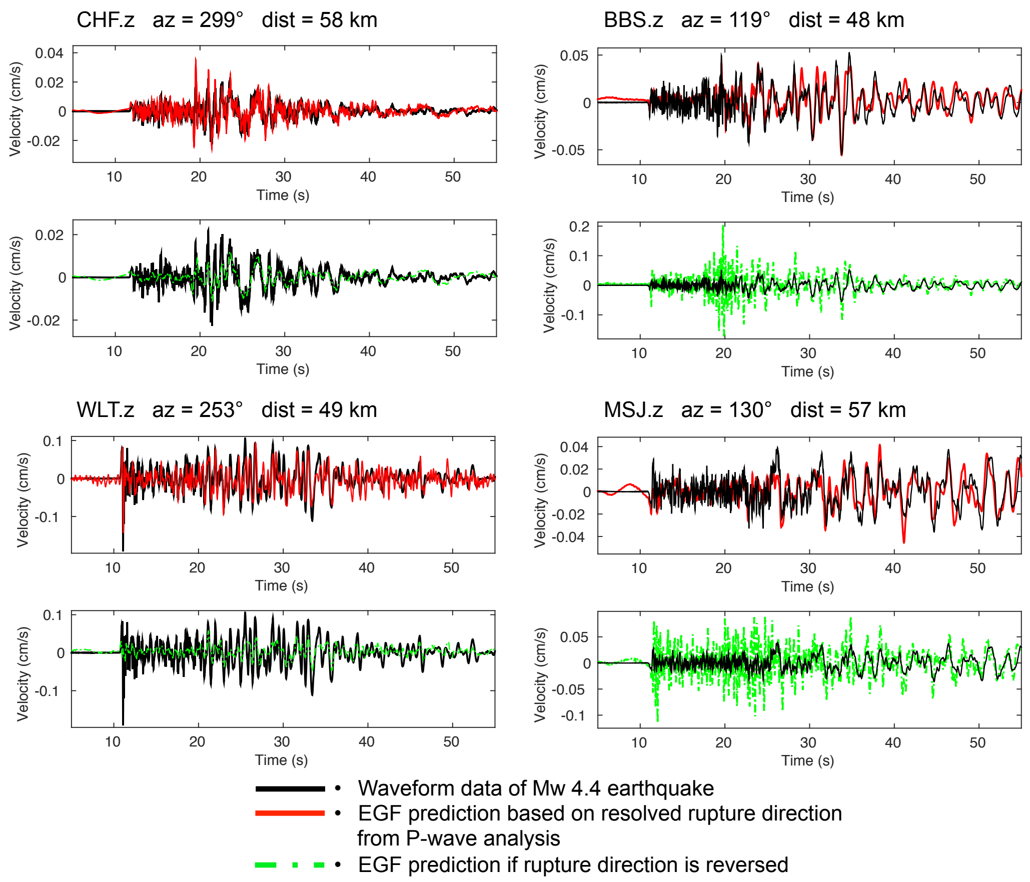

Figure 3.A8: *Rayleigh wave prediction for the same four stations.* The analytical source time functions are formulated with $V_s = 3.18\ km/s$. Results obtained are consistent with the SH wave prediction - EGFs with a NW rupture (red) fit the waveform data (black) much better than when rupture direction is revered (green).

Table 3.A1: 1D crustal model for the Southern California region studied

Thickness (km)	V_s (km/s)	V_p (km/s)	Density (g/cm^3)
5.50	3.18	5.50	2.40
10.50	3.64	6.30	2.67
16.00	3.87	6.70	2.80
12.50	4.50	7.80	3.30

3.7 References

Geng, Jianghui, Yehuda Bock, Diego Melgar, Brendan W Crowell, and Jennifer S Haase (2013). "A new seismogeodetic approach applied to GPS and accelerometer observations of the 2012 Brawley seismic swarm: Implications for earthquake early warning". In: *Geochemistry, Geophysics, Geosystems* 14.7, pp. 2124–2142. DOI: `10.1002/ggge.20144`. URL: `http://dx.doi.org/10.1002/ggge.20144`.

Hauksson, Egill et al. (2008). "Preliminary report on the 29 July 2008 Mw 5.4 chino Hills, eastern Los angeles basin, california, earthquake sequence". In: *Seismological Research Letters* 79.6, pp. 855–866. DOI: `10.1785/gssrl.79.6.855`. URL: `http://dx.doi.org/10.1785/gssrl.79.6.855`.

Helmberger, DV (1983). "Theory and application of synthetic seismograms". In: *Earthquakes: observation, theory and interpretation* 37, pp. 173–222.

Jones, Lucile M et al. (2008). "The shakeout scenario". In: *US Geological Survey Open-File Report* 1150, p. 308.

Kanamori, Hiroo (2005). "Real-time seismology and earthquake damage mitigation". In: *Annu. Rev. Earth Planet. Sci.* 33, pp. 195–214. DOI: `10.1146/annurev.earth.33.092203.122626`. URL: `http://dx.doi.org/10.1146/annurev.earth.33.092203.122626`.

Lui, Semechah KY, Don Helmberger, Shengji Wei, Yihe Huang, and Robert W Graves (2015). "Interrogation of the Megathrust Zone in the Tohoku-Oki Seismic Region by Waveform Complexity: Intraslab Earthquake Rupture and Reactivation of Subducted Normal Faults". In: *Pure and Applied Geophysics* 172.12, pp. 3425–3437. DOI: `10.1007/s00024-015-1042-9`. URL: `http://dx.doi.org/10.1007/s00024-015-1042-9`.

Luo, Yan et al. (2010). "Source mechanism and rupture directivity of the 18 May 2009 Mw 4.6 Inglewood, California, earthquake". In: *Bulletin of the Seismological Society of America* 100.6, pp. 3269–3277. DOI: `10.1785/0120100087`. URL: `http://dx.doi.org/10.1785/0120100087`.

Savage, B and DV Helmberger (2004). "Complex Rayleigh waves resulting from deep sedimentary basins". In: *Earth and Planetary Science Letters* 218.1, pp. 229–239. DOI: `10.1016/S0012-821X(03)00570-3`. URL: `http://dx.doi.org/10.1016/S0012-821X(03)00570-3`.

Song, Xi J and Donald V Helmberger (1996). "Source estimation of finite faults from broadband regional networks". In: *Bulletin of the Seismological Society of America* 86.3, pp. 797–804.

Song, Xi J, Laura E Jones, and Donald V Helmberger (1995). "Source characteristics of the 17 January 1994 Northridge, California, earthquake from regional broadband modeling". In: *Bulletin of the Seismological Society of America* 85.6, pp. 1591–1603.

Tan, Ying and Don Helmberger (2007). “A new method for determining small earthquake source parameters using short-period P waves”. In: *Bulletin of the Seismological Society of America* 97.4, pp. 1176–1195. DOI: `10.1785/0120060251`. URL: `http://dx.doi.org/10.1785/0120060251`.

– (2010). “Rupture directivity characteristics of the 2003 Big Bear sequence”. In: *Bulletin of the Seismological Society of America* 100.3, pp. 1089–1106. DOI: `10.1785/0120090074`. URL: `http://dx.doi.org/10.1785/0120090074`.

Wei, Shengji, Don Helmberger, Susan Owen, Robert W Graves, Kenneth W Hudnut, and Eric J Fielding (2013). “Complementary slip distributions of the largest earthquakes in the 2012 Brawley swarm, Imperial Valley, California”. In: *Geophysical Research Letters* 40.5, pp. 847–852. DOI: `10.1002/grl.50259`. URL: `http://dx.doi.org/10.1002/grl.50259`.

Wei, Shengji et al. (2015). “The 2012 Brawley swarm triggered by injection-induced aseismic slip”. In: *Earth and Planetary Science Letters* 422, pp. 115–125. DOI: `10.1016/j.epsl.2015.03.054`. URL: `http://dx.doi.org/10.1016/j.epsl.2015.03.054`.

Wu, Yih-Min and Hiroo Kanamori (2005). “Rapid assessment of damage potential of earthquakes in Taiwan from the beginning of P waves”. In: *Bulletin of the Seismological Society of America* 95.3, pp. 1181–1185. DOI: `10.1785/0120040193`. URL: `http://dx.doi.org/10.1785/0120040193`.

– (2008). “Development of an earthquake early warning system using real-time strong motion signals”. In: *Sensors* 8.1, pp. 1–9. DOI: `10.3390/s8010001`. URL: `http://dx.doi.org/10.3390/s8010001`.

Zhao, Lian-She and Donald V Helmberger (1994). “Source estimation from broadband regional seismograms”. In: *Bulletin of the Seismological Society of America* 84.1, pp. 91–104.

Zhu, Lupei and Donald V Helmberger (1996). “Advancement in source estimation techniques using broadband regional seismograms”. In: *Bulletin of the Seismological Society of America* 86.5, pp. 1634–1641.

Zhu, Lupei and Luis A. Rivera (2002). “A note on the dynamic and static displacements from a point source in multilayered media”. In: *Geophysical Journal International* 148.3, pp. 619–627. ISSN: 1365-246X. DOI: `10.1046/j.1365-246X.2002.01610.x`. URL: `http://dx.doi.org/10.1046/j.1365-246X.2002.01610.x`.

Chapter 4

REPEATING MICROEARTHQUAKE SEQUENCES INTERACT PREDOMINANTLY THROUGH POSTSEISMIC SLIP

Lui, Semechah KY and Nadia Lapusta (2016). “Repeating microearthquake sequences interact predominantly through postseismic slip”. In: *Nature Communications* 7, p. 13020. DOI: `10.1038/ncomms13020`. URL: `http://dx.doi.org/10.1038/ncomms13020`.

ABSTRACT

Studying small repeating earthquakes enables better understanding of fault physics and characterization of fault friction properties. Some of the nearby repeating sequences appear to interact, such as the "San Francisco" and "Los Angeles" repeaters on the creeping section of the San Andreas Fault. It is typically assumed that such interactions are induced by static stress changes due to coseismic slip. Here, we present a study of the interaction of repeating earthquakes in the framework of rate-and-state fault models using state-of-the-art simulation methods that reproduce both realistic seismic events and long-term earthquake sequences. Our simulations enable comparison among several types of stress transfer that occur between the repeating events. Our major finding is that postseismic creep dominates the interaction, with earthquake triggering occurring at distances much larger than typically assumed. Our results open a possibility of using interaction of repeating sequences to constrain friction properties of creeping segments.

4.1 Introduction

Interaction of earthquakes, which is quite important for uncovering fault physics and quantifying seismic hazard, has been widely studied but, due to large variations in where and how it occurs, the governing physical mechanisms are still unclear (Freed, 2005; Harris, 1998). Advancing the time of instability by a favorable static stress change due to coseismic slip is most commonly used in modeling aftershock sequences (King et al., 1994; Stein, 1999). However, triggering can also be found in areas of unfavorable static stress changes and at distances beyond the reach of significant static stress changes. Other proposed interaction mechanisms include dynamic stress changes due to seismic waves (Gomberg et al., 2001; Hill et al., 1993; Kilb et al., 2000), increased stress loading rate due to aseismic slip (Hsu et al., 2006; Perfettini and Avouac, 2007) or relaxation of the viscoelastic lower crust (Deng et al., 1999; Freed and Lin, 2001), pore fluid motion and induced variations in fault strength (Nur and Booker, 1972) , and evolution of viscoelastic damage rheology due to sudden increase in strain (Ben-Zion and Lyakhovsky, 2006). Earthquake triggering may involve a combination of several mechanisms.

Here, we aim to quantify the relative importance of several triggering mechanisms in the context of small repeating earthquakes. Due to their short recurrence times and known locations, small repeating earthquakes are highly suited for studies of earthquake physics (Hickman et al., 2004; Nadeau and McEvilly, 1999; Vidale et al., 1994) and, in particular, earthquake interaction (Chen et al., 2013). For example, the "San Francisco" (SF) and "Los Angeles" (LA) repeating sequences in Parkfield, California, which are among the primary targets of the San Andreas Fault Observatory at Depth (SAFOD) drilling project, have a lateral separation of less than 70 m (Hickman et al., 2004; Zoback et al., 2011). The LA events tend to occur shortly after the SF events, suggesting a triggering effect (Hickman et al., 2004).

We find that static stress changes due to postseismic slip dominate the interaction of repeating earthquakes on creeping segments. The associated propagating stress front causes the interaction to extend much farther - to 4-7 rupture diameters – than would be predicted based on static stress changes from coseismic slip alone. Conversely, for the same separation distance, the interaction would be much stronger than predicted based on stress changes due to coseismic slip. These findings motivate using interaction of small repeating earthquakes to constrain the friction properties of the surrounding creeping regions.

4.2 Results

4.2.1 Simulations of repeating earthquake sequences

We study interaction of repeating earthquakes in the framework of rate-and-state fault models (Barbot et al., 2012). In the models, repeating earthquakes occur on velocity-weakening (VW) patches embedded into a larger velocity-strengthening (VS) fault area (Figure 4.1a). Such models have been shown to reproduce the behavior of isolated repeating earthquake sequences, in particular, the scaling of their moment versus recurrence time and the response to accelerated postseismic creep (Chen et al., 2010; Chen and Lapusta, 2009). Outside the VS region, slow slip with the long-term fault slip rate is imposed, as would be appropriate for the larger creeping segment. Our simulations produce realistic fault responses, including stick-slip behavior of the patches with aseismic nucleation processes, seismic events with slip rates of the order of 1 m s^{-1}, and postseismic slip (Figure 4.1; Figure 4.B1). This is due to the state-of-the-art simulation methodology that combines slow tectonic-like fault creep with all wave-induced effects during seismic events. The modeling allows us to compare effects of static stress changes due to coseismic and postseismic slip, as well as dynamic stress changes due to seismic waves. The formulation of the model and its parameters are summarized in Appendix A.

4.2.2 Strong earthquake interaction

To study earthquake interaction, it is important to set up a quantitative measure of the interaction. Two repeating sequences are typically considered interactive if the events of one of them occur within a short time of the other. For instance, the inter-event time between the LA and SF repeating sequences is usually less than 24 hours (Hickman et al., 2004). To enable the quantification of interaction in our model, we assign the initial conditions on the fault such that the two patches, if not interacting, would produce earthquakes as far in time from each other as possible, or half of their recurrence interval T_r apart. This is accomplished by first conducting a single-patch calculation and recording the conditions on the patch when it is 0.4 T_r or 0.9 T_r after a seismic event (Figure 4.B2). We then assign these slip rate, stress, and state conditions as the initial ones in the two-patch simulation (Figure 4.B3). If the patches do not interact, then one of them is expected to produce an earthquake in 0.1 T_r and the other one in 0.6 T_r, as happens in the single-patch calculation, making the events 0.5 T_r apart. Indeed, we find that when the distance D between the two patches is large enough ($D = 15d$, where d is the patch diameter), each of them behaves as an isolated repeating sequence, with events on the two patches separated by 0.5 T_r (Figure 4.2, 4.B4a). If the patches interact, the events on the patches occur closer in time. The difference ζ between the simulated inter-event time ΔT_{sim} and the non-interacting inter-event time 0.5 T_r, normalized by 0.5 T_r, can serve as the measure of the degree of interaction:

$$\zeta = \frac{|\ \Delta T_\mathrm{sim} - 0.5T_\mathrm{r}\ |}{0.5T_\mathrm{r}}. \tag{4.1}$$

As expected based on intuition and prior studies (King et al., 1994; Stein, 1999), the two seismogenic patches behave independently when they are far apart and rupture together if they are right next to each other. In the intermediate range of distances, ruptures on the two patches cluster in time (Figure 4.2a). As the distance D between patches decreases, we start to observe interaction, with the inter-event time ΔT_sim decreasing from 0.5 T_r = 2.3 months for $D = 14.7\ d$ to 1.3 days for $D = 1.83\ d$. Hence the extent of the interaction ζ increases from 0 (no interaction) to nearly 1 (Figure 4.2b). Importantly, there is appreciable interaction at distances as large as 4 d ($\zeta = 0.4$), and even some interaction at distances of 7 d ($\zeta = 0.2$). For a larger VW patch, interaction extends even farther, with $\zeta = 0.3$ even at distances $D = 15\ d$ (Figure 4.B5). These results are surprising given the interaction distances of 1 to 2 rupture diameters typical for static stress changes.

Our simulations reveal that, in addition to the static stress increases caused by the coseismic slip of one patch on the other patch, interaction also occurs through accelerated postseismic slip between the two patches. In fact, for a wide range of model parameters, we find the accelerated aseismic slip to be the determining factor in triggering seismic events nearby. To compare the magnitude of different stress changes potentially contributing to triggering, let us consider the shear stress experienced by the center of each VW patch, focusing on the time between two events (Figure 4.3). As patch 1 ruptures (red near-vertical line in Figure 4.3), it produces several types of stress changes on patch 2 (blue line in Figure 4.3). First, dynamic wave-mediated stress changes occur, but they do not seem to have any appreciable effect in our models, consistent with prior studies in rate-and-state model (Kaneko and Lapusta, 2008; Perfettini et al., 2003). Right after the end of the seismic event, patch 2 gets a static stress increase due to the coseismic slip on patch 1, appearing as a relatively small vertical jump of ~0.1 MPa at $t = 2.39$ yr marked as (I) in Figure 4.3. The static stress increase is experienced by other points on the fault as well, and it causes accelerated aseismic slip in the VS area known as afterslip. This accelerated aseismic slip has two kinds of effects on patch 2. First, the stress of patch 2 starts to increase at a faster rate due to the response of the VS area adjacent to patch 2, from 2.39 to 2.415 yr in Figure 4.3, marked as (II). Second, the traveling postseismic front, visible in Figure 4.1b and 4.1c as a yellow to light blue area spreading from one patch to the other, brings with it even larger stressing rate increases, making this last effect dominant in our model (Figure 4.3, from 2.415 to 2.43 yr, marked as (III)). The shear stress loading slows down after the passage of the postseismic stress front (from 2.43 yr onward) but still remains higher than the pre-seismic rate. Shortly before 2.5 yr, patch 2 responds dynamically. In this simulation, the two VW patches are ~3.7 d apart, and $\zeta = 0.54$. At shorter distances between patches, patch 2 typically ruptures even sooner after the creeping front arrives.

The interaction between patches produces other more subtle but interesting effects. Compared to the non-interacting case, the recurrence interval of VW patches is slightly lengthened for cases with shorter separation distances (D = 3.7 d and 1.83 d; Figure 4.2a, Figure 4.B4b). However, the recurrence interval getting longer in two-patch simulations is not a universal effect; in some simulations, the recurrence interval of the VW patches in the two-patch simulation becomes shorter than that in the one-patch simulation (Figure 4.B6). The difference between the recurrence intervals in the single-patch and two-patch simulations likely results from the combination of two factors: the response of the patches to induced stress changes in the two-patch simulations and the difference in seismic events that occur on the patches in the two simulations, as described in the discussion section.

4.2.3 Dominance of postseismic stress change

How can we compare what appears to be, based on the stress changes (Figure 4.3), the dominating effect of the postseismic slip with the effect of the directly induced static stress changed due to coseismic slip (with the latter being the typical explanation for earthquake interaction)? We can estimate the time advance of the triggered earthquake due to the static stress increase caused by coseismic slip alone; the difference between that and the simulated time advance should be due to the postseismic effects. The time advance due to the coseismic slip can be estimated in two ways, based on the Coulomb failure model (Gomberg et al., 2000) and Dieterich rate-and-state model (Dieterich, 1994). The Coulomb model has a simple failure criterion of shear stress τ reaching a critical friction threshold of $\mu(\sigma - p) + S$, where σ is the normal traction (positive in compression), p is the pore fluid pressure, μ is the friction coefficient, and S is the cohesion (Gomberg et al., 2000). Thus the fault is brought closer to failure for positive changes of $\Delta CFS = \Delta\tau - \mu(\Delta\sigma - \Delta p)$ which correspond to the time advance of $\Delta T_{\mathrm{CM}} = \Delta CFS/\dot{\tau}_{\mathrm{b}}$, where $\dot{\tau}_{\mathrm{b}}$ is the background stressing rate. In our models, $\Delta CFS = \Delta\tau$. In the Dieterich model, the time to instability T for a nucleation site with slip velocity V is analytically evaluated based on the spring-slider approximation of elastic interactions and an assumption on the state variable evolution (Dieterich, 1994):

$$T(V) = \frac{a\bar{\sigma}}{\dot{\tau}_{\mathrm{b}}} \ln\left(\frac{\dot{\tau}_{\mathrm{b}}}{H(\sigma - p)V} + 1\right), \dot{\tau}_{\mathrm{b}} \neq 0, \tag{4.2}$$

$$H = \frac{-k}{(\sigma - p)} + \frac{b}{L}, \tag{4.3}$$

where $\bar{\sigma} = \sigma - p$ is the effective normal stress, a, b, and L are rate-and-state parameters (see Appendix A) and k is the spring stiffness (and hence the effective stiffness of the nucleation site). A positive step in shear stress ($\Delta\tau$) increases slip rate V to $V_{\mathrm{new}} = \exp[\Delta\tau/(a(\sigma - p))]$, thus shortening the time to the next rupture. The difference $\Delta T_{\mathrm{DM}} = T(V) - T(V_{\mathrm{new}})$ between the two times to instability constitutes the time advance due to $\Delta\tau$.

From our simulations, we can obtain the interseismic stress loading rate $\dot{\tau}_{\mathrm{b}}$ and positive shear stress step $\Delta\tau$ occurring on the triggered patch due to coseismic slip on the other patch. The stiffness of the nucleation patch can be approximated (Perfettini et al., 2003) as $k = \eta G/h_{\mathrm{nucl}}$, where $\eta = 2/\pi$, G is the shear modulus, and h^* is the nucleation size given by (Rubin and Ampuero, 2005):

$$h^* = \frac{2GLb}{\pi\bar{\sigma}(b - a)^2}, \tag{4.4}$$

Therefore, we can estimate the corresponding time advances ΔT_{CM} and ΔT_{DM}, which are about an order of magnitude smaller than the simulated time advance (Figure 4.2b), confirming the dominant effect of the stress changes due to postseismic slip.

4.3 Discussion

Our finding that the interaction of earthquakes on creeping segments may be dominated by their postseismic slip opens the possibility of estimating fault friction properties based on modeling the interaction. The postseismic slip depends on the stress drop of the seismic event, which determines the stress increase on the surrounding creeping fault regions, as well as the steady-state velocity strengthening $(a - b)\bar{\sigma}$ of the creeping region (Perfettini and Avouac, 2007); the latter effect is demonstrated in Figure 4.B7. Values of $(a - b)$ much larger than the ones estimated in the laboratory impede postseismic slip and remove its triggering effect (Figure 4.4a). If the stress drops are known, one can determine, through modeling, the range of values of $(a - b)\bar{\sigma}$ that reproduce observations.

For the LA and SF repeaters on the San Andreas Fault, determining the constraints on friction due to postseismic-slip-dominated interaction would involve first determining which source properties (including stress drop) better fit the available seismic data. Currently stress estimates for small earthquakes are typically obtained from a widely used relation for a circular crack of radius r with the constant stress drop $\Delta\tau$ and moment M_{o}: $\Delta\tau = (7M_o)/(16r^3)$, in which the moment is well constrained and the radius r is determined from the source spectra and its corner frequency based on simplified source models (Abercrombie, 2014). For the LA and SF sequences, such stress drop estimates are in the range of 10 to 30 MPa (Abercrombie, 2014; Dreger et al., 2007; Imanishi et al., 2004), depending on the simplified source model used. If the stress drops of the LA and SF repeaters are indeed ~10 MPa, then, given the inferences of their separation, the patches are large enough to be right next to each other (Figure 4.4b). In our model, they would essentially rupture in a single dynamic event. If the stress drops are closer to 30 MPa, then the events are separated by about 1.4 diameters of the repeaters (taking the average diameter of the two patches), similar to the shortest inter-patch distance of $D = 1.83\ d$ considered here. In that case, based on our modeling so far, the interaction should be dominated by postseismic slip and hence by the velocity-strengthening friction properties of the area between the patches. The absence of the LA-SF interaction after the 2004 M_{w} 6.0 Parkfield earthquake may be due to the increase in the value of $(a - b)\bar{\sigma}$ between the patches, for example, due to decrease in pore pressure. Determining the realistic source properties of the LA and SF repeaters based on seismic data as well as constraining the velocity-strengthening properties between the patches based on the interaction would require a targeted three-dimensional modeling of the two repeaters, in which a two-dimensional fault is embedded into a three-dimensional elastic medium, with patches represented as circles, a subject of our ongoing work. Note that such much more computationally challenging modeling could not be used in this work, as it would make the longer inter-patch distances $D/d = 15$ considered here computationally intractable in the context of simulating earthquake sequences.

The interaction of the two patches in our simulations is influenced by multiple kinds of stress changes received at different times of their interseismic period (Figure 4.3);

this complexifies the resulting patch behavior. One such complexity is that the recurrence time of interacting patches may be either shorter or longer than that of identical patches that do not interact. This is due to a combination of two factors. First, after seismic event I on patch 1 triggers a seismic event II on patch 2, the (favorable) stress perturbations from event II reach patch 1 early in its interseismic cycle, and such stress perturbations sometimes advance and sometimes delay the nucleation process. The delay can result if the (favorable) stress changes lead to a nucleation-size aseismic transient, relieving stresses in the nucleation zone and delaying the next seismic event (Kaneko and Lapusta, 2008). Second, different stress conditions on the patches before a seismic event (due to ongoing stress interactions as well as due to rupture nucleation in a slightly different location within the patch) can cause the resulting seismic slip on the patches to be slightly different, corresponding to different stress drops and hence different required interseismic loading times. The intricate interplay between these interrelated factors needs to be investigated further. It may at least partially explain the irregularity of the observed repeating sequences, which are likely to be continuously perturbed not only by each other, as in the case of the LA and SF repeaters, but also by other seismic events nearby as well as potential interseismic phenomena such as unsteady creep elsewhere on the fault (Maurer and Johnson, 2014).

To enable the precise quantification of the interaction and quantitative comparison between the effects of various stress changes, we have focused here on the models with the initial conditions that put the two patches half a cycle (0.5 T_r) apart; the results should hold for other initial conditions as well, based on the following consideration. If the first event on patch 1 occurs when patch 2 is closer to failure than half a cycle, then the extent of interaction between patches should be the same or greater than in the half-a-cycle-apart case. If the first event on patch 1 occurs when patch 2 is farther from failure than half a cycle, then that particular event may have smaller or no effect; however, at the time of the next seismic event on patch 2, patch 1 should be closer to failure than half a cycle, and the interaction should again be the same or greater than in the half-a-cycle-apart case, but with the patch roles reversed (patch 2 triggering patch 1). This is essentially what our simulations show. For example, for large enough patches (d = 82 m = 4.1 h^* and 108 m = 5.4 h^*, where h^* is the nucleation size for the VW patches given by Equation 4.4, and patch separation distance $D = 1.83\ d$, the eventual behavior is that of seismic events on one patch triggering seismic events on the other patch nearly instantaneously compared to their recurrence interval, for all initial conditions we have explored

(Figure 4.B6, 4.B8-4.B9). This is also true for several cases of initial conditions for smaller patches (d = 40 m = 2 h^* and 54 m = 2.7 h^*, Figure 4.2, 4.B8-4.B9).

Some initial conditions on smaller patches lead to more complex behavior, with the two patches initially moving towards such rapid triggering, but then gradually evolving to the long-term state in which the two patches consistently rupture half a cycle (0.5 T_r) apart (Figure 4.B8-4.B10). Note that such a pattern also represents interaction strongly influenced by postseismic slip, not only because substantial triggering is indeed observed at the beginning of the simulations, but also because the long-term behavior is different from the predictions based on co-seismic stress changes only (Figure 4.2b). According to both Coulomb and Dieterich predictions, coseismic seismic stress changes imposed by a seismic event on patch 1 onto patch 2 should advance the next seismic event on patch 2 by 15-20% (Figure 4.2b). The fact that this does not happen in the simulations is probably related to the additional influence of the postseismic stress changes. Ultimately, this evolving behavior is due to the interplay of seismic and substantial aseismic slip, both spontaneous and interaction-induced, on such smaller patches, which would be completely aseismic if they were smaller than h^* (Chen and Lapusta, 2009). This apparent precise cancellation among all triggering effects will likely disappear in a more realistic three-dimensional model, especially in the presence of spatial heterogeneity in fault friction properties that is likely to exist on natural faults and perturb the regularity of the patch recurrence. Note that the patch behavior is dependent on the ratio of d/h^* because the ratio of aseismic to seismic slip on the patches systematically increases as the patch diameter d decreases to the nucleation size h^* (Chen and Lapusta, 2009).

The potentially dominant effect of postseismic slip on the interaction of repeating earthquakes demonstrated by our modeling adds to the growing realization of the importance of aseismic slip in earthquake source processes, even in phenomena long thought to be dominated by seismic slip. This includes the suggestion that aftershock sequences may be at least partially controlled by aseismic slip (Perfettini and Avouac, 2007) as well as with the observations that fluid injection into fault zones may trigger aseismic slip which, in turn, at least helps to trigger microseismicity (Guglielmi et al., 2015; Wei et al., 2015). Our findings motivate further development of earthquake source models that faithfully reproduce the interaction between seismic and aseismic fault slip, such as realistic source models of the Parkfield repeaters constrained by the wealth of available data (Zoback et al., 2011).

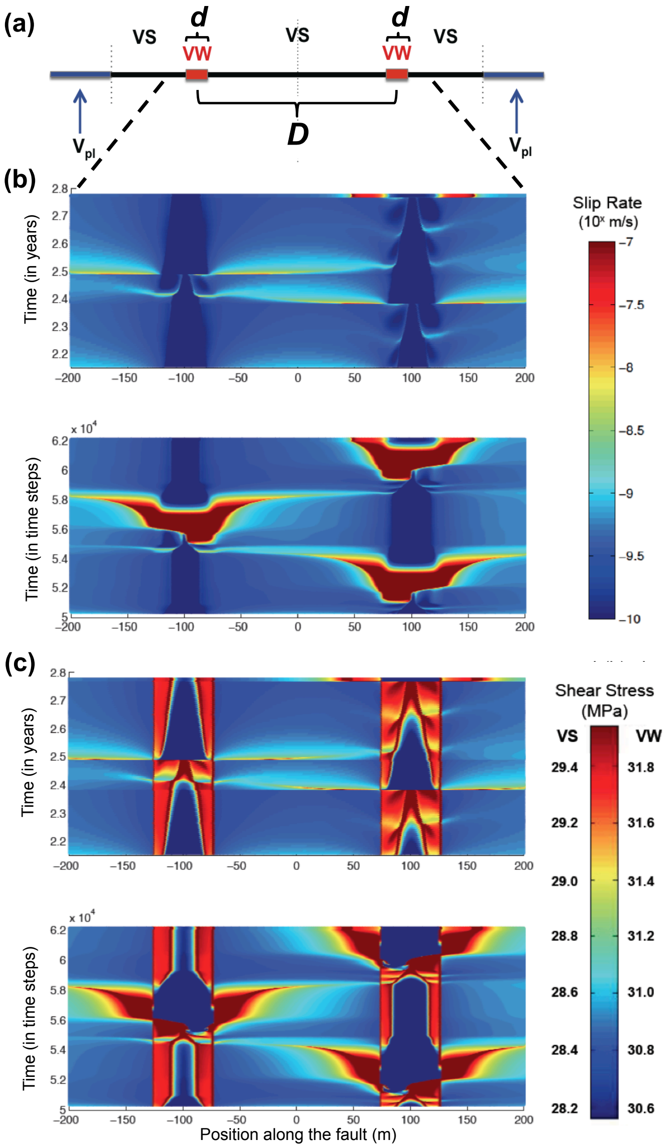

Figure 4.1: *Interaction of two repeating earthquake sequences in a rate-and-state fault model.* (a) Schematics of the model in which a one-dimensional fault is embedded into elastic medium and loaded with slow, tectonic slip rate of 23 mm yr^{-1}. The fault contains two seismogenic velocity-weakening (VW) patches surrounded with velocity-strengthening (VS) regions. (b,c) Evolution of slip rate (b) and shear stress (c) on the fault with the simulated time (top) and as functions of variable time step (bottom). The color scales are chosen to emphasize the slip rates and stress values relevant to postseismic effects. Seismic events start at an edge of a VW patch and spread through the patch, penetrating into and eventually stopping in the surrounding VS regions. The resulting postseismic creeping fronts (PCFs) are clearly observed traveling from one patch to the other. The PCF from the right patch advances the seismic event on the left patch. The PCF from the left patch triggers some aseismic slip on the right patch, but without appreciably changing the timing of the event appreciably. The time-dependent evolution of the slip rate is also shown in Movie S1.

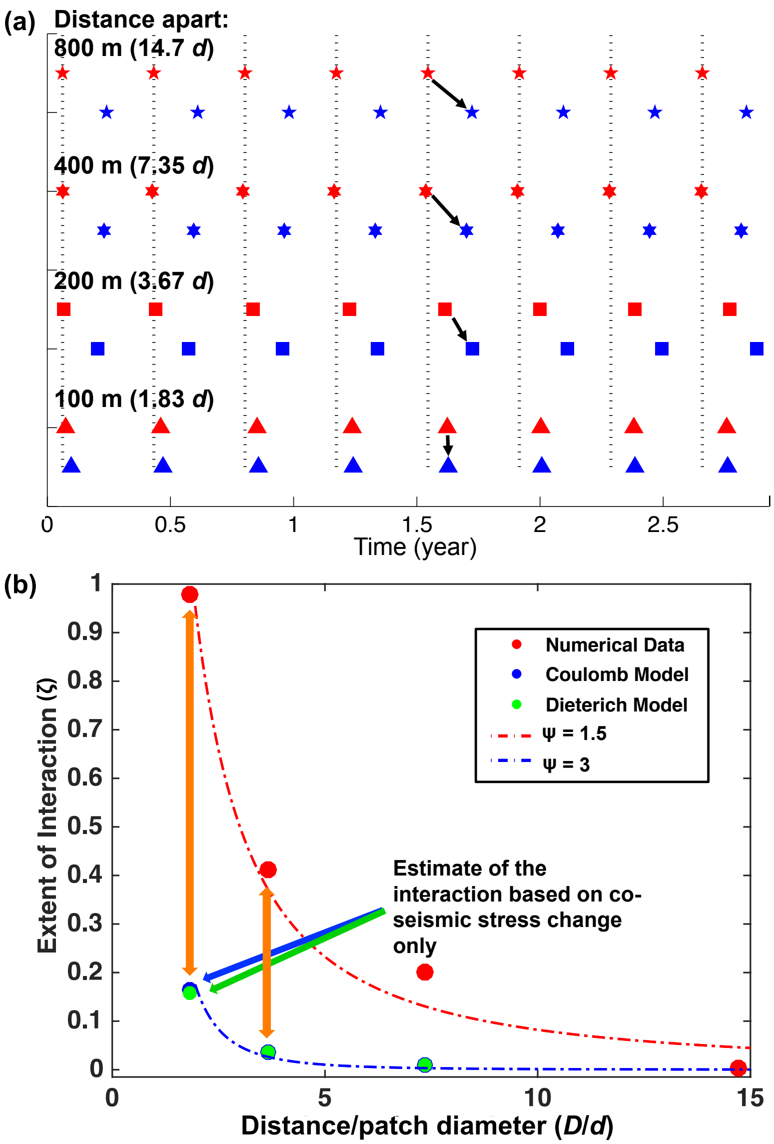

Figure 4.2: *Exploring the extent of interaction.* (a)Dependence of the interaction on the distance between the patches. Red and blue markers represent the occurrence of seismic events on the two VW patches. Patches in the simulation with $D = 15\ d$ rupture with the expected inter-event time of half of the single-patch recurrence time, and hence they are non-interacting. The inter-event times decrease significantly as the distance between the two VW patches reduces. Dashed lines mark the recurrence interval for the non-interacting case. (b) Extent of interaction in our simulations (red dots) plotted against separation distance D/d. Estimates of the interaction based on the coseismic stress changes only for the Coulomb and Dieterich models are shown as blue and green dots, respectively. Orange arrows indicate the inferred effect of postseismic creep which clearly dominates. Dashed lines show the fit of the results to a power law $\zeta = (D/d)^{-\Psi}$.

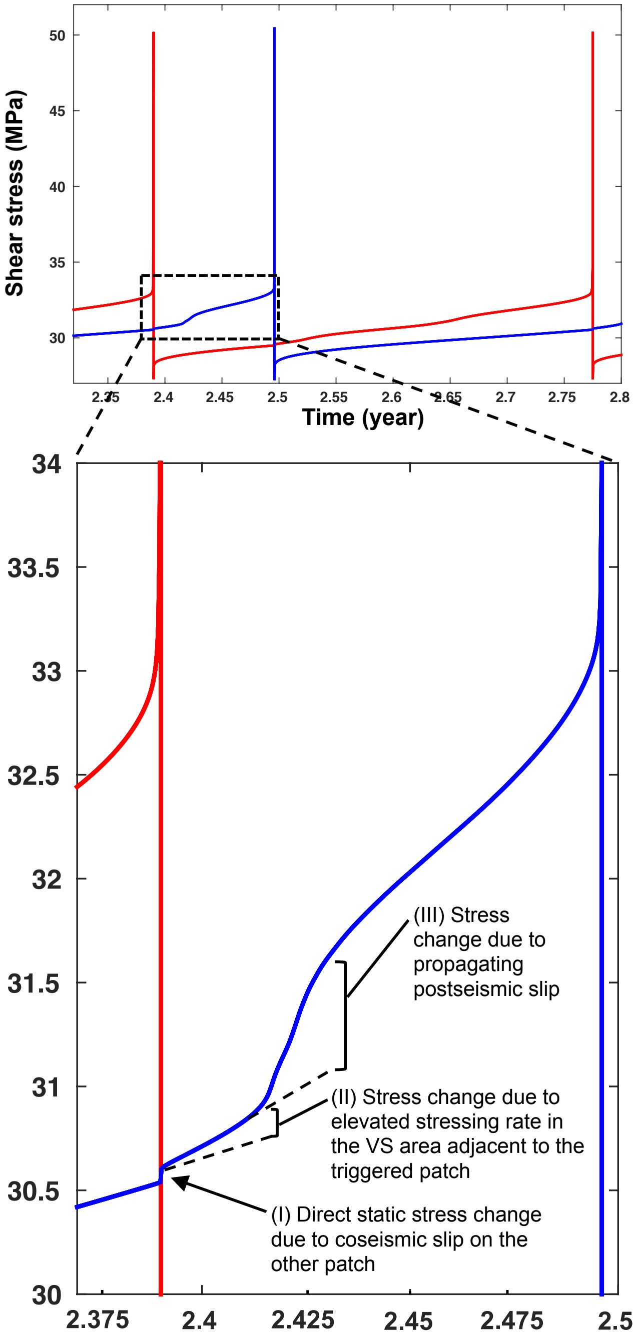

Figure 4.3: *Different types of stress changes induced on the triggered VW patch.* (Top) Shear stress as a function of time in the center of the triggering patch (red line) and triggered patch (blue). (Bottom) Zoom into the dashed rectangle of the top panel shows three types of stress increases in the triggered patch: (I) Direct static stress change due to coseismic slip on the other patch; (II) Stress change due to elevated stressing rate in the VS region adjacent to the triggered patch; (III) Stress change due to propagating postseismic creep. Postseismic stress changes (II) and (III) are clearly much larger than the stress change (I) due to coseismic slip only.

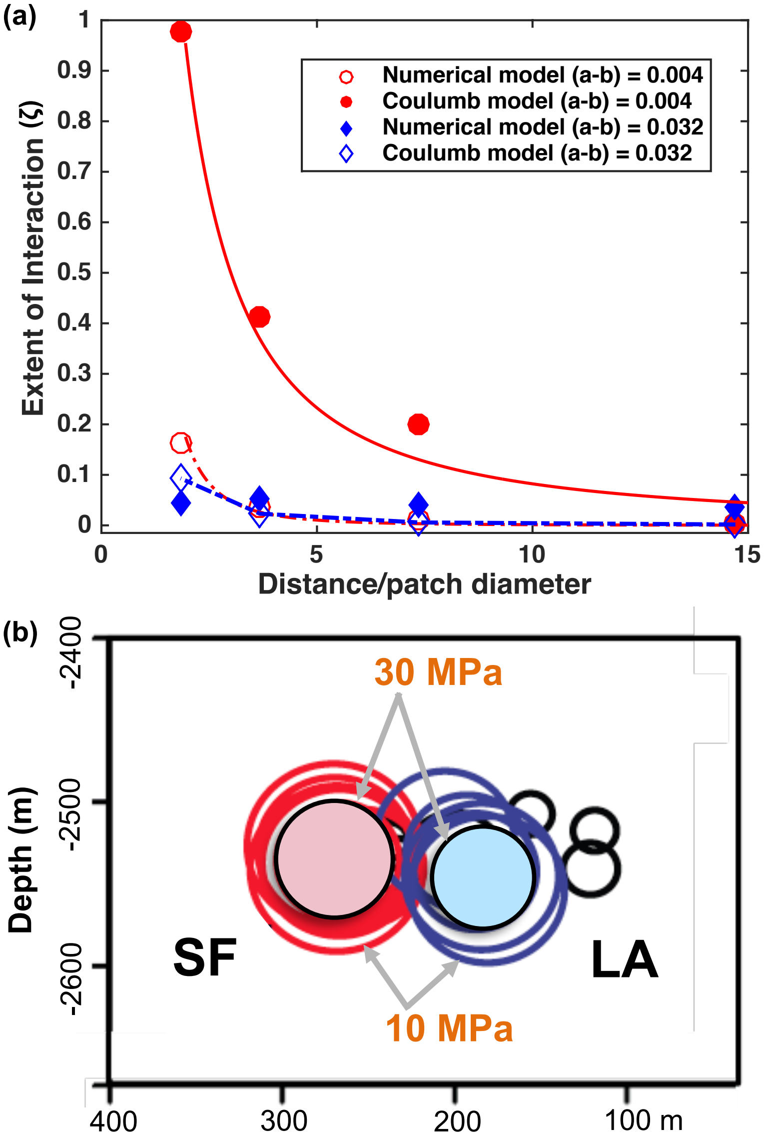

Figure 4.4: *Effect of the VS region on the interaction.*(a) Comparison of interaction with different friction properties of the VS region: $(a-b)_{\text{VS}} = 0.004$ (circles) and 0.032 (diamonds). Filled and empty markers represent our numerical model and Coulomb model, respectively. Postseismic creep (and its effect) is suppressed as $(a-b)_{\text{VS}}$ increases from 0.004 to 0.032. (b) Schematic diagram of the fault plan view of the San Andreas fault at Parkfield around the area that hosts the SF and LA repeaters (modified from Zoback et al., 2011). The extent of the patches for both 10 MPa (empty circles) and 30 MPa (filled circles) stress drops are shown; D/d changes with different stress drop estimates. For the stress drops of 30 MPa, the repeaters are separated by about 1.4 average patch diameters; the nearly-instantaneous triggering observed for these repeaters before 2004 is consistent with our findings and can be used to constrain the velocity-strengthening properties of the creeping region.

4.4 Appendix A: The Rate-and-State Fault Model

Our numerical simulations are based on a two-dimensional elastodynamic model of a one-dimensional fault embedded into an elastodynamic medium. The fault is governed by laboratory-derived rate-and-state friction laws which have been quite successful in reproducing a number of earthquake phenomena (Dieterich, 2007). The shear strength is given by:

$$\tau_f = \bar{\sigma} f = (\sigma - p)[f_o + a \ln(\frac{V}{V_{\mathrm{o}}}) + b \ln(\frac{V_o \theta}{L})], \tag{4.5}$$

$$\frac{d\theta}{dt} = 1 - \frac{V\theta}{L}, \tag{4.6}$$

where τ_f is the shear strength of the fault, $\bar{\sigma}$ is the effective normal stress, f is the friction coefficient, f_{o} is the reference friction coefficient at the reference slip velocity V_{o}, a and b are rate-and-state parameters, V is the slip velocity, and L the characteristic slip for the evolution of the state variable θ. In steady state, when V is constant, one gets $\theta = L/V$ and the resulting shear stress (τ_{ss}) is:

$$\tau_{\mathrm{ss}} = \bar{\sigma}[f_{\mathrm{o}} + (a - b) \ln(\frac{V}{V_{\mathrm{o}}})]. \tag{4.7}$$

Thus an interface with $a - b < 0$ has VW friction, while $a - b > 0$ corresponds to VS friction. On the fault, two VW patches are surrounded by VS regions (Figure 4.1a); outside, the long-term slip rate is imposed. Parameters of the model are listed in Table 4.A1; the values of a and b in the velocity-strengthening region as well as the patch diameter are varied in some simulations as specified when the simulations are discussed. Stresses, slips, and slip rates within the VW and VS regions are computed by equating the fault shear stress given by elastodynamic relations with the fault strength given by the friction law (Equation 4.5 and 4.7) (Lapusta and Liu, 2009). We make the size of the friction fault large enough to ensure that the effects of seismic and postseismic slip on the patches die out before reaching the boundaries of the friction region, so that the edges of the friction region move with the long-term slip rate consistent with the imposed rate outside.

Table 4.A1: Parameters of Our Simulations

Parameter	Symbol	Value
Shear wave speed	c_s	3.0 km s^{-1}
Shear modulus	μ	30 GPa
Loading slip rate	V_{pl}	23 mm yr^{-1}
Reference slip velocity	V_0	10^{-6} m s^{-1}
Reference friction coefficient	f_0	0.6
Characteristic slip distance	L	40 μm
Effective normal stress	$\bar{\sigma}$	50 MPa
Rate-and-state parameters in VW region	a, b	0.015, 0.019
Nucleation size	h^*	20 m
Rate-and-state parameters in VS region[1]	a, b	0.019, 0.015
Patch diameters[1]	d	54 m

[1] Unless stated otherwise.

4.5 Appendix B: Supplementary Information

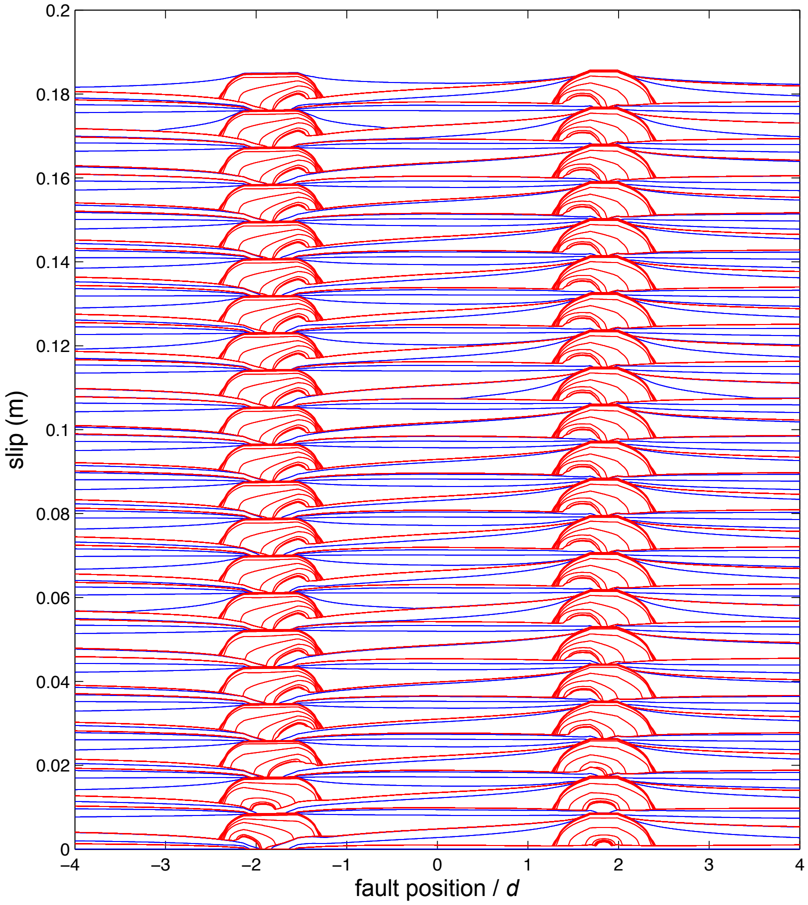

Figure 4.B1: *Cumulative slip along the fault through time, based on the initial conditions shown in Figure4.B2.* Blue and red lines represent the interseismic and coseismic periods, respectively. In this simulation, $D = 3.7\ d$. It takes four seismic cycles for the VW patches to establish a stable rupture pattern, in which the two events initiate on the side of the patch closest to the other patch, the location favored by the stress changes imposed by one patch on the other.

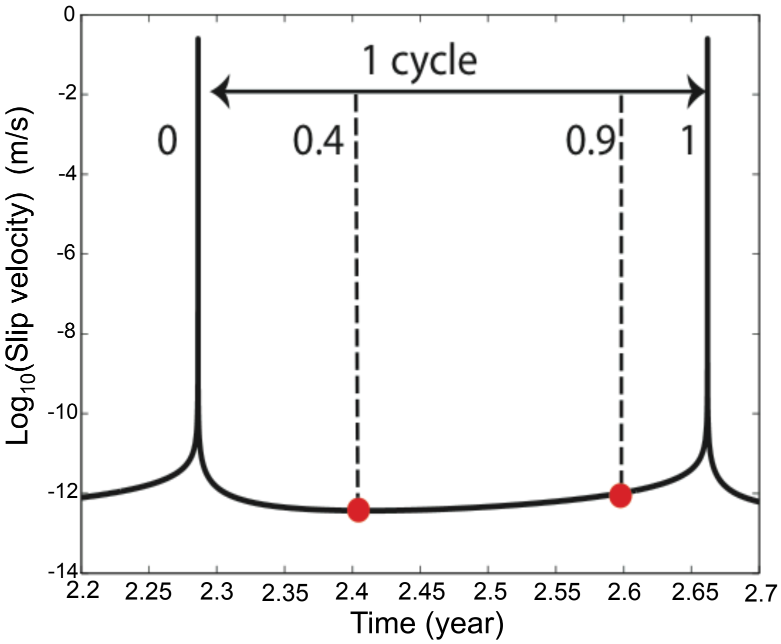

Figure 4.B2: *Selecting initial conditions for simulations that allow us to quantify the potential interaction between the repeating sequences.* The initial slip rate, shear stress, and state conditions for the two VW patches are taken from a single-patch simulation at two particular snapshots in time, 0.4 T_r and 0.9 T_r, respectively. If the two patches do not interact, then they are expected to produce seismic events 0.5 T_r apart.

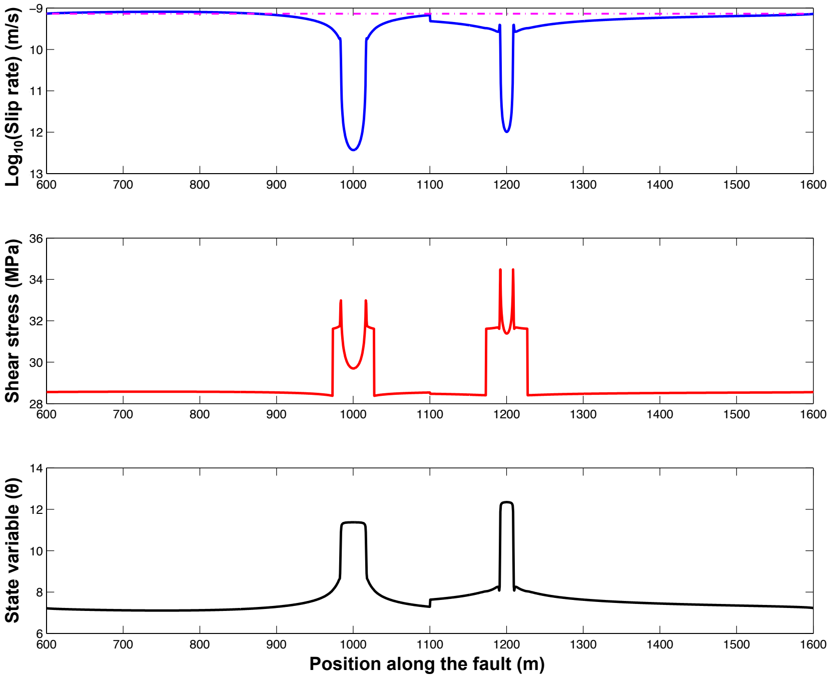

Figure 4.B3: *Example of initial conditions* (spatial distributions of the slip rate, shear stress, and state variable θ) on the fault. In this simulation, D = 3.7 d. The VW patch on the right ruptures first after the simulation begins. We refer to the patch as "patch 1." The magenta dotted line in the top panel indicates the loading rate.

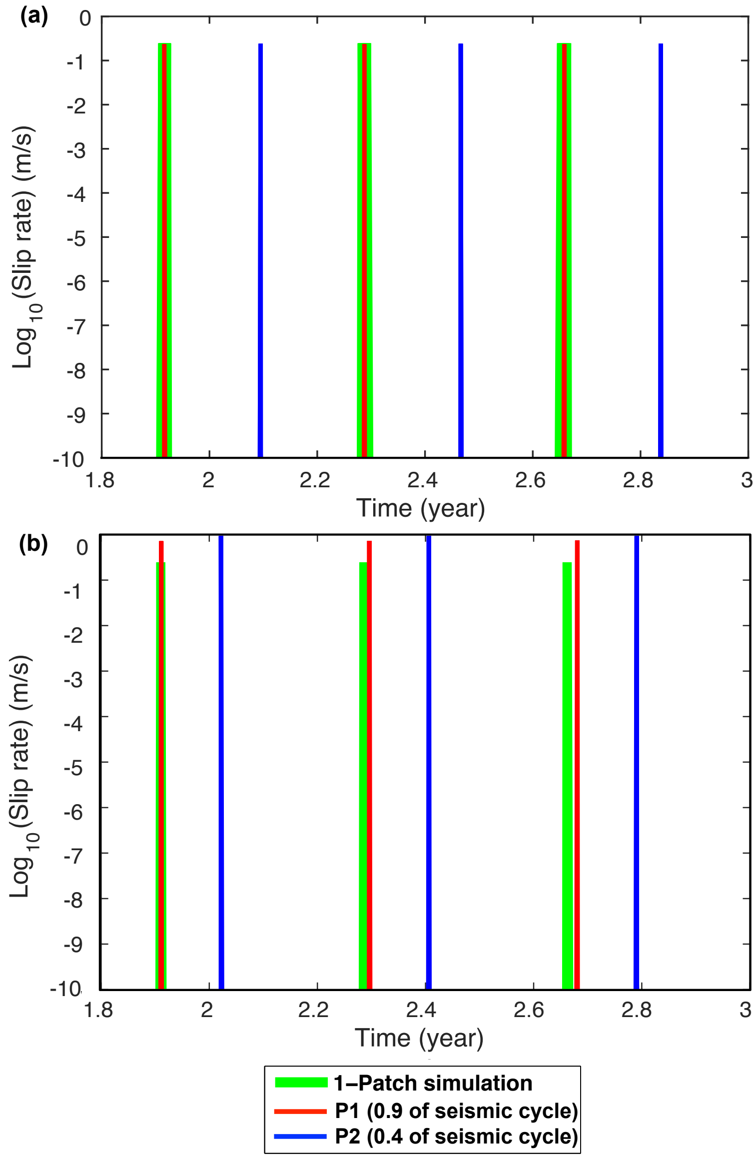

Figure 4.B4: *Comparison of the single-patch (thick green lines) and two-patch (blue and red lines) simulations* with (a) D = 15 d and (b) D = 3.7 d. In (a), for both simulations, slip rate at the center of the VW patches is identical. In the two-patch case, each patch behaves as the one in the single-patch simulation, with one of the patches shifted by half the recurrence time, as intended by the initial conditions. Therefore, the two repeating sequences are seismically independent for D = 15 d. In (b), for D = 3.7 d, there is an interaction, with patch 1 (red lines) inducing patch 2 (blue lines) to rupture sooner than half a cycle apart. The recurrence interval in the two-patch simulation is also slightly longer.

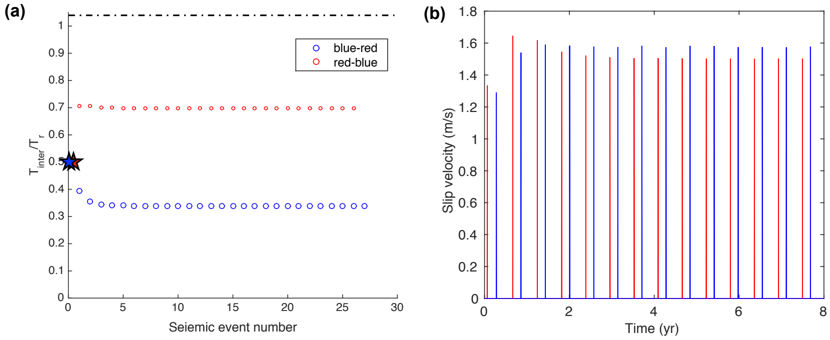

Figure 4.B5: Interaction of two VW patches with $d = 82$ m $= 4.1\ h^*$, a diameter larger than our basic case (Table 4.A1), separated by $D = 15\ d$. (a) The inter-event time between seismic events on the two patches, T_{inter}, normalized by the recurrence interval of a single-patch simulation, T_r, is plotted as a function of the event number. The stars indicate the inter-event time of 0.5 T_{r} imposed by the initial conditions. As patch 1 produces the first seismic event, patch 2 ruptures sooner than imposed by the initial conditions, and the inter-event time between events on patch 1 and patch 2 is decreased from 0.5 T_{r} to 0.34 T_{r} (blue circles), resulting in $\zeta = 0.32$. Note that the inter-event time between an event on patch 2 and the next one on patch 1 is correspondingly growing to 0.7 (red circles). The black dashed line represents the ratio between the new Tr in this simulation and the original T_{r} showing that, in this case, the recurrence time of the patches is nearly identical to the simulations with a single patch. (b) Slip velocity in the middle of the patch 1 and 2 (red and blue lines, respectively), illustrating the occurrence of the seismic events with time.

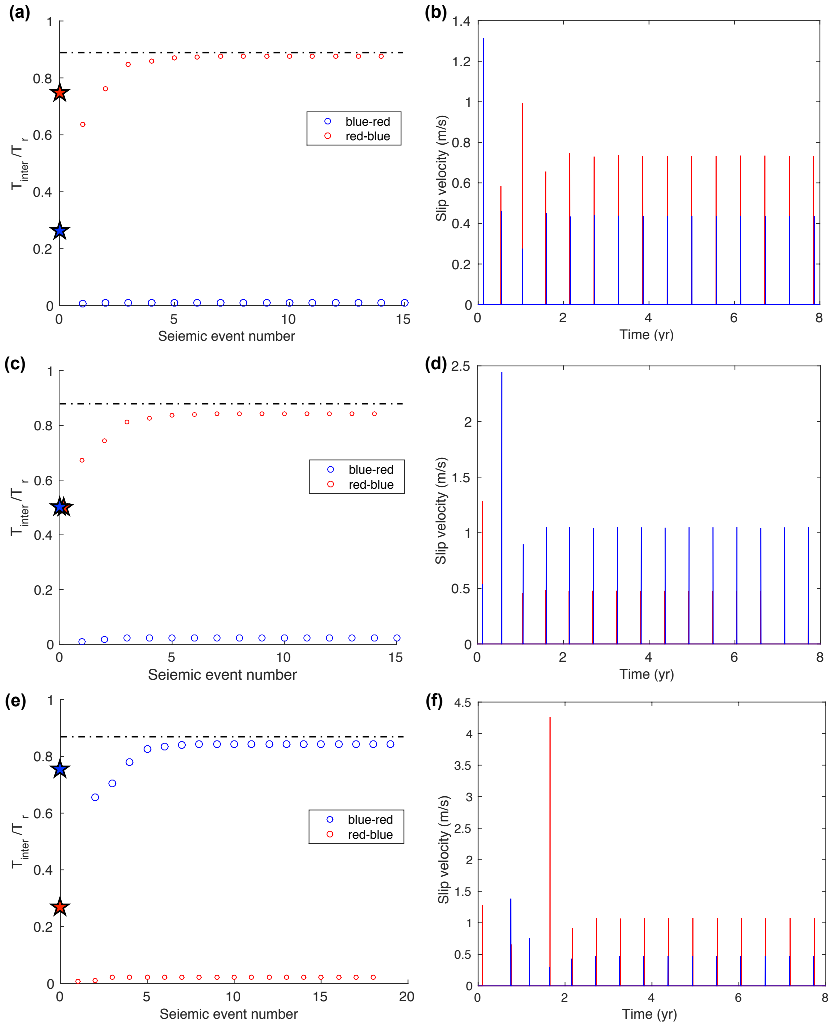

Figure 4.B6: Interaction of two VW patches with d = 108 m, D = 1.83 d, and initial conditions (a-b) 0.9 T_r and 0.65 T_r (separation of 0.25 T_r), (c-d) 0.9 T_r and 0.4 T_r (separation of 0.5 T_r), and (e-f) 0.9 T_r and 0.15 T_r (separation of 0.75 T_r). Markers and lines have the same meaning as those of Figure 4.B5. In all cases, we observe near-instantaneous triggering between the patches. For the case with the initial conditions of 0.9 T_r and 0.15 T_r, the triggering pattern is reversed as expected, with patch 2 triggering patch 1. Note that the recurrence interval in the two-patch simulations is about 0.9 of that of the single-patch simulation, as illustrated by the dashed lines in the left column.

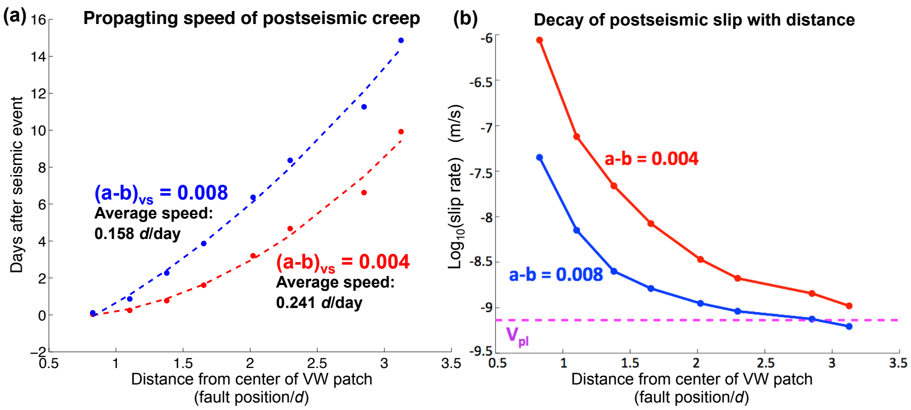

Figure 4.B7: *Behavior of postseismic creep on faults with different velocity-strengthening friction properties* $(a-b)_{\text{VS}}$. (Left) Comparison of the propagating speed of the postseismic creep front (PCF). Red and blue curves represent simulations with $(a-b)_{\text{VS}} = 0.004$ and 0.008 respectively. (Right) Comparison of the decay of the maximum PCF slip rate with distance from the center of the VW patch.

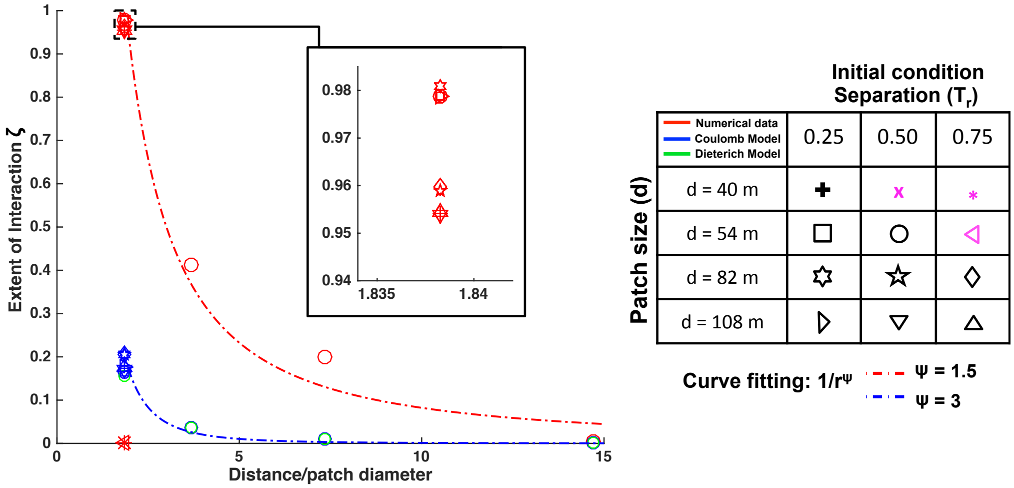

Figure 4.B8: Comparing the extent of interaction ζ as defined in the main text for VW patches with different initial conditions for $D = 1.83\ d$, superimposed on the cases of Figure 4.2b from the main text. (inset) Zoom into the dashed rectangle. For large enough VW patches, all initial conditions result in near-instantaneous triggering in our numerical simulations (red markers), validating the results for the specific initial conditions presented in the main text. Blue markers indicate the Coulomb model prediction for the static stress changes alone, for the same cases. For smaller patches just above the nucleation size, some initial conditions (Table 4.B1) show the strong interaction initially (e.g., Figure 4.B10) but then evolve towards being half a cycle apart, as discussed in the main text. These cases are indicated by magenta symbols in the legend on the right of the plot.

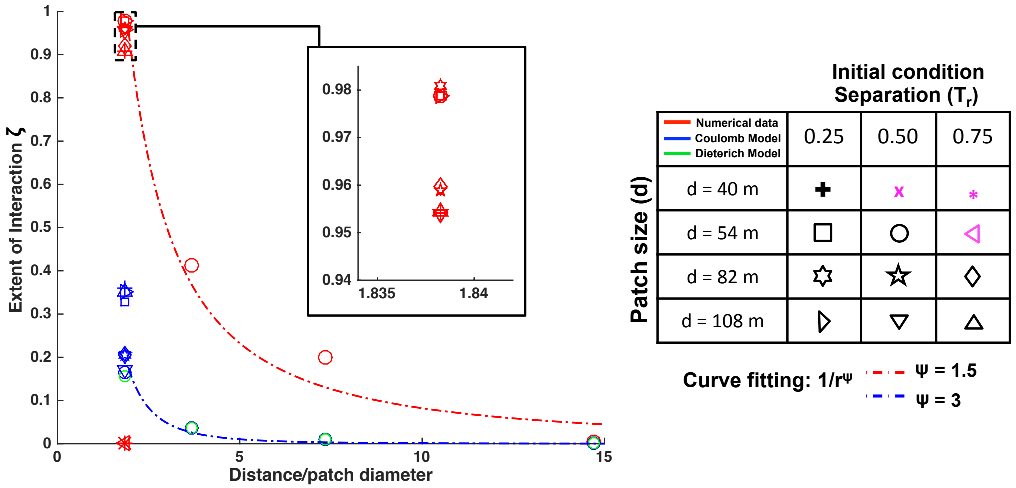

Figure 4.B9: Similar to Figure 4.B8, but with a different definition of ζ, In the main text and Figure4.B8, ζ is defined with respect to the half-recurrence interval 0.5 T_r which is both the inter-event time imprinted in the initial conditions of our basic simulated case and the intuitive inter-event time for non-interacting patches. Here, ζ is redefined with respect to the actual time separation in the initial conditions of the two patches, i.e., 0.25 T_r for some cases and 0.5 T_r for others, both for numerical simulations and Coulomb estimates.

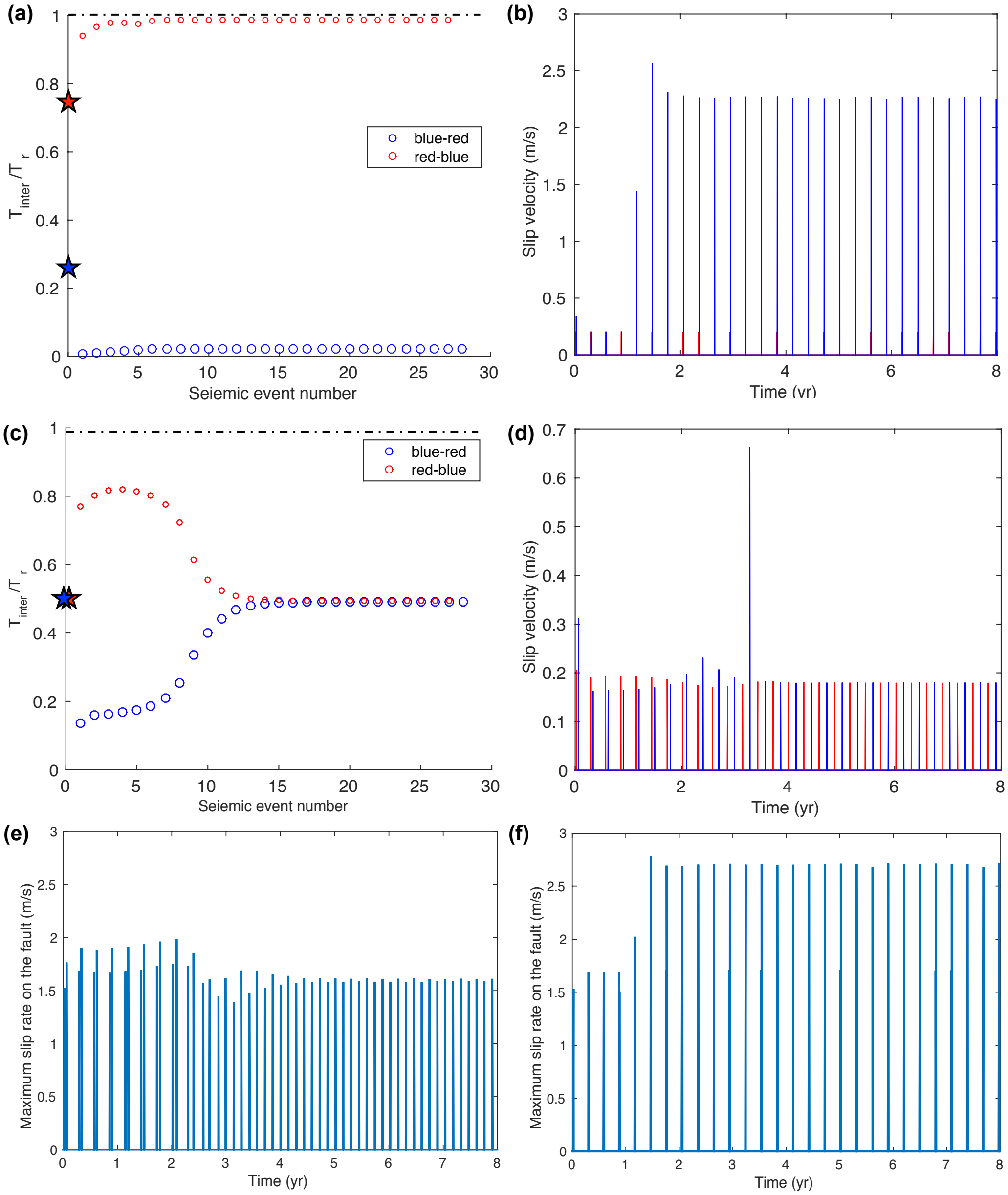

Figure 4.B10: Interaction of two VW patches with with d = 40 m, D = 1.83 d, and (a-b) 0.9 T_r and 0.65 T_r (separation of 0.25 T_r), and (c-d) 0.9 T_r and 0.4 T_r (separation of 0.5 T_r). Markers and lines have the same meaning as those of Figure 4.B5. For the initial conditions separated by 0.25 T_r, when patch 1 ruptures, patch 2 is at about 0.75 of its interseismic period, which leads to near-instantaneous triggering. For the initial conditions separated by 0.5 T_r, the two patches start off with substantial interaction. However, the model behavior evolves into seismic events on the two patches being half a cycle apart. This still indicates substantial interaction, as discussed in the main text.

Table 4.B1: Summary of the eventual event pattern for a range of VW patch sizes d and initial conditions, with $D = 1.83\ d$. "Yes" and "No" indicate whether near-instantaneous triggering occurs in the simulations; the cases with "No" start with the interaction but eventually evolve towards seismic events being half a cycle apart. h^* denotes the nucleation size. Details of simulations with asterisks are shown in Figure 4.B6 and 4.B10.

	IC = 0.9 T_r & 0.65 T_r	IC = 0.9 T_r & 0.4 T_r	IC = 0.9 T_r & 0.15 T_r
$d = 40$ m $\approx 2\ h^*$	Yes*	No*	No
$d = 54$ m $\approx 2.7\ h^*$	Yes	Yes	No
$d = 82$ m $\approx 4.1\ h^*$	Yes	Yes	Yes
$d = 108$ m $\approx 5.4\ h^*$	Yes*	Yes*	Yes*

4.6 References

Abercrombie, Rachel E. (2014). “Stress drops of repeating earthquakes on the San Andreas Fault at Parkfield”. In: *Geophysical Research Letters* 41.24. 2014GL062079, pp. 8784–8791. ISSN: 1944-8007. DOI: `10.1002/2014GL062079`. URL: `http://dx.doi.org/10.1002/2014GL062079`.

Barbot, Sylvain, Nadia Lapusta, and Jean-Philippe Avouac (2012). “Under the hood of the earthquake machine: Toward predictive modeling of the seismic cycle”. In: *Science* 336.6082, pp. 707–710. DOI: `10.1126/science.1218796`. URL: `http://dx.doi.org/10.1126/science.1218796`.

Ben-Zion, Yehuda and Vladimir Lyakhovsky (2006). “Analysis of aftershocks in a lithospheric model with seismogenic zone governed by damage rheology”. In: *Geophysical Journal International* 165.1, pp. 197–210. DOI: `10.1111/j.1365-246X.2006.02878.x`. URL: `http://dx.doi.org/10.1111/j.1365-246X.2006.02878.x`.

Chen, Kate Huihusan, Roland Bürgmann, and Robert M. Nadeau (2013). “Do earthquakes talk to each other? Triggering and interaction of repeating sequences at Parkfield”. In: *Journal of Geophysical Research: Solid Earth* 118.1, pp. 165–182. ISSN: 2169-9356. DOI: `10.1029/2012JB009486`. URL: `http://dx.doi.org/10.1029/2012JB009486`.

Chen, Kate Huihusan, Roland Bürgmann, Robert M Nadeau, Ting Chen, and Nadia Lapusta (2010). “Postseismic variations in seismic moment and recurrence interval of repeating earthquakes”. In: *Earth and Planetary Science Letters* 299.1, pp. 118–125. DOI: `10.1016/j.epsl.2010.08.027`. URL: `http://dx.doi.org/10.1016/j.epsl.2010.08.027`.

Chen, Ting and Nadia Lapusta (2009). “Scaling of small repeating earthquakes explained by interaction of seismic and aseismic slip in a rate and state fault model”. In: *Journal of Geophysical Research: Solid Earth* 114.B1. B01311, n/a–n/a. ISSN: 2156-2202. DOI: `10.1029/2008JB005749`. URL: `http://dx.doi.org/10.1029/2008JB005749`.

Deng, Jishu, Kenneth Hudnut, Michael Gurnis, and Egill Hauksson (1999). “Stress loading from viscous flow in the lower crust and triggering of aftershocks following the 1994 Northridge California, earthquake”. In: *Geophysical Research Letters* 26.21, pp. 3209–3212. DOI: `10.1029/1999GL010496`. URL: `http://dx.doi.org/10.1029/1999GL010496`.

Dieterich, James (1994). “A constitutive law for rate of earthquake production and its application to earthquake clustering”. In: *Journal of Geophysical Research: Solid Earth* 99.B2, pp. 2601–2618. ISSN: 2156-2202. DOI: `10.1029/93JB02581`. URL: `http://dx.doi.org/10.1029/93JB02581`.

Dieterich, JH (2007). “Applications of rate-and state-dependent friction to models of fault slip and earthquake occurrence”. In: *Treatise on Geophysics* 4, pp. 107–129.

Dreger, Douglas, Robert M Nadeau, and Angela Chung (2007). “Repeating earthquake finite source models: Strong asperities revealed on the San Andreas Fault”. In: *Geophysical Research Letters* 34.23. doi: `10.1029/2007GL031353`. url: `http://dx.doi.org/10.1029/2007GL031353`.

Freed, Andrew M (2005). “Earthquake triggering by static, dynamic, and postseismic stress transfer”. In: *Annu. Rev. Earth Planet. Sci.* 33, pp. 335–367. doi: `10.1146/annurev.earth.33.092203.122505`. url: `http://dx.doi.org/10.1146/annurev.earth.33.092203.122505`.

Freed, Andrew M and Jian Lin (2001). “Delayed triggering of the 1999 Hector Mine earthquake by viscoelastic stress transfer”. In: *Nature* 411.6834, pp. 180–183. doi: `10.1038/35075548`. url: `http://dx.doi.org/10.1038/35075548`.

Gomberg, J., N. Beeler, and M. Blanpied (2000). “On rate-state and Coulomb failure models”. In: *Journal of Geophysical Research: Solid Earth* 105.B4, pp. 7857–7871. issn: 2156-2202. doi: `10.1029/1999JB900438`. url: `http://dx.doi.org/10.1029/1999JB900438`.

Gomberg, J, PA Reasenberg, P Bodin, and RA Harris (2001). “Earthquake triggering by seismic waves following the Landers and Hector Mine earthquakes”. In: *Nature* 411.6836, pp. 462–466. doi: `10.1038/35078053`. url: `http://dx.doi.org/10.1038/35078053`.

Guglielmi, Yves, Frédéric Cappa, Jean-Philippe Avouac, Pierre Henry, and Derek Elsworth (2015). “Seismicity triggered by fluid injection–induced aseismic slip”. In: *Science* 348.6240, pp. 1224–1226. doi: `10.1126/science.aab0476`. url: `http://dx.doi.org/10.1126/science.aab0476`.

Harris, Ruth A. (1998). “Introduction to Special Section: Stress Triggers, Stress Shadows, and Implications for Seismic Hazard”. In: *Journal of Geophysical Research: Solid Earth* 103.B10, pp. 24347–24358. issn: 2156-2202. doi: `10.1029/98JB01576`. url: `http://dx.doi.org/10.1029/98JB01576`.

Hickman, Stephen, Mark Zoback, and William Ellsworth (2004). “Introduction to special section: preparing for the San Andreas Fault Observatory at Depth”. In: *Geophysical Research Letters* 31.12. doi: `10.1029/2004GL020688`. url: `http://dx.doi.org/10.1029/2004GL020688`.

Hill, DP et al. (1993). “Seismicity remotely triggered by the magnitude 7.3 Landers, California, earthquake”. In: *Science* 260.5114, pp. 1617–1623. doi: `10.1126/science.260.5114.1617`. url: `http://dx.doi.org/10.1126/science.260.5114.1617`.

Hsu, Ya-Ju et al. (2006). “Frictional afterslip following the 2005 Nias-Simeulue earthquake, Sumatra”. In: *Science* 312.5782, pp. 1921–1926. doi: `10.1126/science.1126960`. url: `http://dx.doi.org/10.1126/science.1126960`.

Imanishi, Kazutoshi, William L Ellsworth, and Stephanie G Prejean (2004). “Earthquake source parameters determined by the SAFOD Pilot Hole seismic array”. In: *Geophysical Research Letters* 31.12. DOI: `10.1029/2004GL019420`. URL: `http://dx.doi.org/10.1029/2004GL019420`.

Kaneko, Y and N Lapusta (2008). “Variability of earthquake nucleation in continuum models of rate-and-state faults and implications for aftershock rates”. In: *Journal of Geophysical Research: Solid Earth* 113.B12. DOI: `10.1029/2007JB005154`. URL: `http://dx.doi.org/10.1029/2007JB005154`.

Kilb, Deborah, Joan Gomberg, and Paul Bodin (2000). “Triggering of earthquake aftershocks by dynamic stresses”. In: *Nature* 408.6812, pp. 570–574. DOI: `10.1038/35046046`. URL: `http://dx.doi.org/10.1038/35046046`.

King, Geoffrey CP, Ross S Stein, and Jian Lin (1994). “Static stress changes and the triggering of earthquakes”. In: *Bulletin of the Seismological Society of America* 84.3, pp. 935–953.

Lapusta, Nadia and Yi Liu (2009). “Three-dimensional boundary integral modeling of spontaneous earthquake sequences and aseismic slip”. In: *Journal of Geophysical Research: Solid Earth* 114.B9. DOI: `10.1029/2008JB005934`. URL: `http://dx.doi.org/10.1029/2008JB005934`.

Maurer, Jeremy and Kaj Johnson (2014). “Fault coupling and potential for earthquakes on the creeping section of the central San Andreas Fault”. In: *Journal of Geophysical Research: Solid Earth* 119.5, pp. 4414–4428.

Nadeau, Robert M and Thomas V McEvilly (1999). “Fault slip rates at depth from recurrence intervals of repeating microearthquakes”. In: *Science* 285.5428, pp. 718–721. DOI: `10.1126/science.285.5428.718`. URL: `http://dx.doi.org/10.1126/science.285.5428.718`.

Nur, Amos and John R Booker (1972). “Aftershocks caused by pore fluid flow?” In: *Science* 175.4024, pp. 885–887. DOI: `10.1126/science.175.4024.885`. URL: `http://dx.doi.org/10.1126/science.175.4024.885`.

Perfettini, H and J-P Avouac (2007). “Modeling afterslip and aftershocks following the 1992 Landers earthquake”. In: *Journal of Geophysical Research: Solid Earth* 112.B7. DOI: `10.1029/2006JB004399`. URL: `http://dx.doi.org/10.1029/2006JB004399`.

Perfettini, H, J Schmittbuhl, and A Cochard (2003). “Shear and normal load perturbations on a two-dimensional continuous fault: 2. Dynamic triggering”. In: *Journal of Geophysical Research: Solid Earth* 108.B9. DOI: `10.1029/2002JB001805`. URL: `http://dx.doi.org/10.1029/2002JB001805`.

Rubin, AM and J-P Ampuero (2005). “Earthquake nucleation on (aging) rate and state faults”. In: *Journal of Geophysical Research: Solid Earth* 110.B11. DOI: `10.1029/2005JB003686`. URL: `http://dx.doi.org/10.1029/2005JB003686`.

Stein, Ross S (1999). “The role of stress transfer in earthquake occurrence”. In: *Nature* 402.6762, pp. 605–609. DOI: `10.1038/45144`. URL: `http://dx.doi.org/10.1038/45144`.

Vidale, JE, WL Ellsworth, A Cole, C Marone, et al. (1994). “Variations in rupture process with recurrence interval in a repeated small earthquake”. In: *Nature* 368.6472, pp. 624–626. DOI: `10.1038/368624a0`. URL: `http://dx.doi.org/10.1038/368624a0`.

Wei, Shengji et al. (2015). “The 2012 Brawley swarm triggered by injection-induced aseismic slip”. In: *Earth and Planetary Science Letters* 422, pp. 115–125. DOI: `10.1016/j.epsl.2015.03.054`. URL: `http://dx.doi.org/10.1016/j.epsl.2015.03.054`.

Zoback, Mark, Stephen Hickman, William Ellsworth, et al. (2011). “Scientific drilling into the San Andreas Fault Zone—An overview of SAFOD’s first five years”. In: *Sci. Drill* 11.1, pp. 14–28. DOI: `10.2204/iodp.sd.11.02.2011`. URL: `http://dx.doi.org/10.2204/iodp.sd.11.02.2011`.

Chapter 5

MODELING THE HIGH STRESS DROPS AND THE INTERACTIONS OF THE REPEATING MICROEARTHQUAKES IN PARKFIELD

ABSTRACT

In this study, we reproduce, through numerical modeling of rate-and-state faults, the observed high stress drops of the repeating microearthquake sequences in Parkfield and their interactive behavior. The two sequences, named the Los Angeles (LA) and San Francisco (SF) events, are primary targets of the San Andreas Fault Observatory at Depth (SAFOD) drilling project, and have recurrence interval of approximately 3 years. The LA event tends to occur within hours after the SF event, suggesting strong triggering effect. Previous studies reported high stress drops for these repeaters of the order of 30 MPa. Based on models developed in Chapter 4, we further explore additional mechanisms which are necessary for the standard rate-and-state framework to match the inferred stress drops, as well as the synchronized seismic pattern. Results indicate that enhanced coseismic weakening and elevated effective normal stress on the VW patches are possible causes for the high stress drops. These models are characterized by the occurrence of substantial and variable aseismic slip on the repeating sources, which is the key to explaining the variability in the repeating source properties, their sometimes irregular interactions, their neither slip nor time-predictable behavior, and their atypical relation between recurrence interval and seismic moment.

5.1 Repeating earthquake sequences in Parkfield

While earthquakes with large magnitude ($> M_\mathrm{w}$ 7) tend to be the focus of research studies due to the catastrophic destruction that they can bring, they occur too infrequently to be useful for studies of earthquake problems in temporal scale. Small repeating earthquake sequences, on the other hand, are excellent candidates due to their short recurrence time and known location. At the same time, nature has also provided us with exciting study sites. The Parkfield segment of the San Andreas Fault (SAF) in California is the meeting place of a seismic and aseismic activities and one of the most well-studied fault segment. The SAF in this region is slipping at approximately 23 mm yr^{-1} (Lisowski and Prescott, 1981; Murray et al., 2001; Titus et al., 2006) and at the same time hosting earthquakes with a wide range of M_w. The most well-known series is the seven M_w 6.0 earthquakes that occurred approximately every 22 years since 1857 and has invited extensive studies (Bakun et al., 2005; Bakun and McEvilly, 1984; Barbot et al., 2012). On top of that, a number of microearthquakes with M_w 2-3 are also identified as repeating sequences, i.e. seismic events that occur at the same place on a regular basis, with highly similar seismic signals. Because of all the intriguing phenomena, the San Andreas Fault Observatory at Depth (SAFOD) operational plan was designed and implemented in 2000's to address a number of scientific questions related to fault mechanics (Zoback et al., 2011). A number of repeating microearthquakes were selected as targets on the fault plane at depth to guide the drilling trajectory, including the Los Angeles (LA) ad the San Francisco (SF) repeaters (Figure 5.1a).

Here we focus on modeling the SF and LA repeating earthquake sequences in this region. The magnitude of these events hovers around M_w 2, with a recurrence interval (T_r) of 2.5 to 3 years (Nadeau et al., 2004; Zoback et al., 2011). In particular, the average T_r of the seven SF events before year 2004 is 2.9 yr, with a standard deviation of 0.35 yr. For each of the sequences, the seismograms for all the events are highly correlated. Their relative locations are determined to ±10-meter uncertainty using cross-correlation alignments of common P- and S- phases between events (Nadeau et al., 2004). This indicates that repeaters are located in exactly the same location on the faults, separated by ~60 to 70 m along strike, at comparable depths of approximately 3 km (Nadeau et al., 2004; Zoback et al., 2011).

Previous modeling (Chen and Lapusta, 2009) of the repeating earthquakes at Parkfield suggests that there is significant aseismic slip occurs at the location of the repeaters. This can be illustrated by the following simple argument. The average

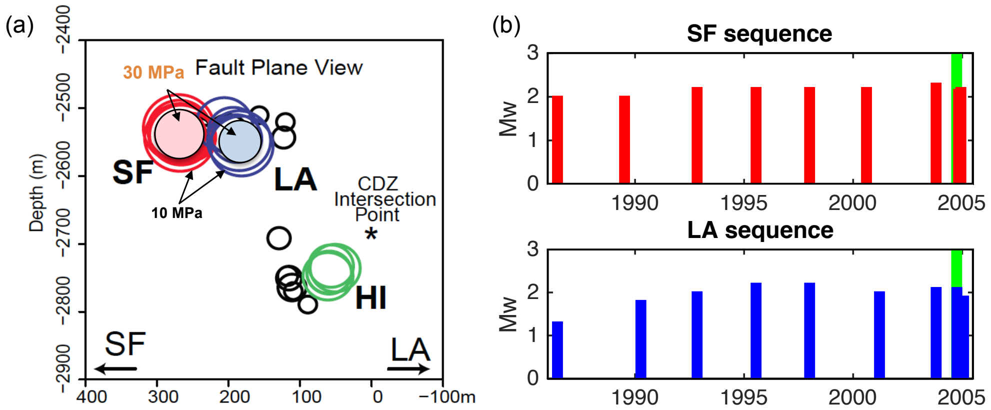

Figure 5.1: *Repeating earthquake sequences on the portion of the Parkfield segment of the San Andreas Fault* (adopted from Zoback et al. (2011)). (a) The SF and LA repeaters are spatially close to each other, with similar magnitude and relatively high stress drop. Red and blue circles are the source dimensions with 10-MPa stress-drop assumption. Filled pink and light blue circles illustrates the modified dimensions based on 30-MPa stress drop. (b) Time progression and magnitude of the SF and LA sequences, with each red and blue vertical line representing an event on the SF and LA patch, respectively. The occurrence of the M_w 6.0 earthquake is marked as the green line.

magnitude of the LA and SF repeating sequences in Parkfield is around M_w 2. According to Nadeau and Johnson (1998), the observed scaling relationship between recurrence time (T_r) and seismic moment (M_0) in this region is

$$\log T_\mathrm{r} = 0.16(\log M_0) - 2.53, \tag{5.1}$$

which results in a recurrence interval of ~3 years as observed. If we assume the background slip rate in the region to be approximately 23 mm yr^{-}1 based on previous studies (Lisowski and Prescott, 1981; Murray et al., 2001; Titus et al., 2006), the cumulative slip for each repeating earthquake and interseismic period is $V_\mathrm{pl} * T_\mathrm{r} =$ 0.07 m on average. If we assume that the slip is 100% seismic and use the seismic moment expression:

$$M_0 = \mu A \delta, \tag{5.2}$$

where $A = \pi r^2$ is circular rupture area, μ is shear modulus, and δ is the slip, the seismic slip of 70 m and $M_\mathrm{w} = 2$ results in a source radius of ~9 m. However, the stress drop on such a circular crack model is given by (Brune, 1970; Eshelby, 1957; Madariaga, 1976):

$$\Delta\tau = \frac{7M_0}{16r^3}, \tag{5.3}$$

resulting in ~300-MPa very high stress drop, a value which has not been inferred in any studies in the region.

So, clearly, the slip of 0.07 m per recurrence period cannot be all seismic. As demonstrated by the study of Chen and Lapusta, (2009), indeed, a rate-and-state fault model in which the patch size is above the nucleation size, but close to it, results in significant aseismic slip at the location of seismic events, allowing for the overall required slip with reasonable stress drops of the seismic events.

Another interesting phenomenon reported in previous studies on these clusters is their very high average stress drop values ($\Delta\sigma_{\mathrm{avg}}$) compared to other microseismicities. (Abercrombie, 1995, 2014; Dreger et al., 2007; Nadeau and Johnson, 1998; Sammis et al., 1999). The study of Abercrombie, (2014) used borehole data from the San Andreas Fault Observatory at Depth (SAFOD) drilling project and highly correlated empirical Green's functions to resolve the stress drops for several clusters, including the SF and LA repeaters. It found that $\Delta\sigma_{\mathrm{avg}}$ of the SF patch ranges between 25 and 65 MPa, while that of the LA patch, though with higher uncertainties, is between 1 and 20 MPa. Dreger et al., (2007) investigated the rupture process of the SF sequence using seismic moment rate function inversions obtained from empirical Green's function deconvolution. Based also on SAFOD borehole data, the authors recovered the finite fault slip and stress drop distribution and obtained a variable spatial distribution of the stress drop ranging from 60 to 90 MPa. Such high value was required to fit the shape of the moment rate functions. The hypocenters of these two sequences are determined to be less than 70 m apart based on double-difference relocation analysis (Waldhauser et al., 2004; Zoback et al., 2011). If one assumes a typical 10-MPa $\Delta\sigma_{\mathrm{avg}}$, the source regions of the two clusters would overlap each other (open circles in Figure 5.1a). This prompts the question: Why did the two patches rupture separately? If the $\Delta\sigma_{\mathrm{avg}}$ is indeed higher, at approximately 30 MPa, source dimensions reduce and do not overlap (filled light blue and pink circle in Figure 5.1a), explaining why SF and LA being separate repeating sequences and not a single source.

In addition, the LA and SF repeating sources have largely synchronized timing, which is a strong indication of the two sequences interacting (Nadeau et al., 2004). Before the Parkfield M_{w} 6.0 earthquake in 2004, the LA events typically occurred within 24 hours after the SF events (Figure 5.1b). The physics behind this phenomenon, as well as earthquake interaction in general, is a topic of high interest. Various mechanisms have been proposed. The mechanism most commonly assumed in many aftershock modeling studies is the static stress change due to coseismic slip. Others include dynamic stress change due to seismic waves, increased stress loading rate due to aseismic slip, the relaxation of the viscoelastic lower crust, induced variations in fault strength, etc (Deng et al., 1999; Freed and Lin, 2001; Gomberg et al., 2001; Hill et al., 1993; Hsu et al., 2006; Kilb et al., 2000; Nur and Booker, 1972; Perfettini and Avouac, 2004). In Chapter 4, we have explored the interactions between two generic repeating sequences and determined that stress changes due to postseismic slip propagating from the seismic source to neighboring seismogenic patches is actually the dominating mechanism contributing to seismic triggering between repeating earthquake sequences. This opens the possibility of determining the friction properties of the fault surrounding the LA and SF repeaters based on their interactions.

Note that, while Chen and Lapusta, (2009) were able to constrain a set of fault parameters that successfully reproduce the T_r-M_o scaling relationship as observed in Parkfield, they had to use a long-term slip rate (V_pl) of 4.5 mm yr^{-1} in order to match the absolute values of the observed recurrence times. This is significantly lower than the 23 mm yr^{-1} observed in Parkfield (Murray et al., 2001). This is because the stress drops of the repeaters in their model, ~7 MPa, are significantly lower than the observed range of values inferred by Abercrombie, (2014). Chen and Lapusta suggested modifications in the considered friction law such as the inclusion of strong dynamic weakening, which might preserve the simulated scaling but lengthen the recurrence time, so that the model can also better match the higher reference loading rate.

The goal of this work is to construct models that reproduce both the intriguing source characteristics and interactive behavior of the SF and LA sequences in Parkfield, to shed light on the frictional properties of the fault in the area. We find that the high stress drop values can be modeled with additional mechanisms such as thermal pressurization of pore fluids and locally elevated normal stress. Interactions of the two sequences depend heavily on the frictional properties of the creeping region between them, which controls the behavior of postseismic slip.

5.2 Methodology: Modeling the San Francisco and Los Angeles repeaters

5.2.1 Fault frictional resistance

Our model adopts the rate-and-state friction laws, which have been empirically derived through rock experiments in the laboratory (Dieterich, 1979; Dieterich, 1981; Dieterich, 2007; Marone, 1998; Ruina, 1983 and references therein). The laws are capable of modeling and explaining both aseismic and seismic phenomena (Ben-Zion and Rice, 1997; Dieterich, 1994; Dieterich, 1992; Gomberg et al., 1998; Lapusta and Rice, 2003; Liu and Rice, 2005; Miyazaki et al., 2006; Perfettini et al., 2003; Rice and Ruina, 1983; Tullis, 1996) (Marone et al., 1991). Under this law, the shear strength τ_{f} on the fault is given by:

$$\tau_{\mathrm{f}} = \bar{\sigma} f = (\sigma - p)[f_{\mathrm{o}} + a \ln(\frac{V}{V_{\mathrm{o}}}) + b \ln(\frac{V_{\mathrm{o}}\theta}{L})], \tag{5.4}$$

where $\bar{\sigma}$ is the effective normal stress, σ is the normal stress, p is the pore pressure, f is the friction coefficient, f_{o} is the reference friction coefficient at the reference slip velocity V_{o}, a and b are rate-and-state parameters, V is the slip velocity, and L is the characteristic slip for the evolution of the state variable θ.

The evolution of the state variable θ in our model is governed by the aging formulation:

$$\frac{d\theta}{dt} = 1 - \frac{V\theta}{L}. \tag{5.5}$$

In steady state, when V is constant, one gets $\theta = L/V$ and the resulting shear resistance τ_{ss} is:

$$\tau_{\mathrm{ss}} = \bar{\sigma}[f_{\mathrm{o}} + (a - b)\ln(\frac{V}{V_{\mathrm{o}}})]. \tag{5.6}$$

Thus the value of parameter combination $(a - b)$ defines the fault behavior at steady state. $a - b > 0$ corresponds to velocity-strengthening (VS) frictional properties, resulting in stable aseismic slip at the imposed loading rate, while $a - b < 0$ has velocity-weakening (VW) friction, and, for VW area of sufficiently large sizes, results in potentially seismogenic regions (Rice et al., 2001; Rice and Ruina, 1983; Rubin and Ampuero, 2005). In the following, we refer to fault regions as being VS or VW with the implicit understanding that the characterization applies to the steady state behavior. In our study, one important parameter is the critical size of the VW slipping region capable of producing seismic slip under slow loading, which can be estimated as (Chen and Lapusta, 2009; Rubin and Ampuero, 2005)

$$h^* = \frac{\pi^2}{4}\frac{2\mu b L}{\pi\bar{\sigma}(b - a)^2}, \tag{5.7}$$

where μ is the shear modulus.

In our model, a planar fault is embedded in a three-dimensional elastic half-space. Using spectral boundary-integral methodology (Lapusta and Liu, 2009; Lapusta et al., 2000; Noda and Lapusta, 2010), we successfully solve for the spontaneous slip history on the fault, resolving all aspects of seismic and aseismic slip at different stages of the seismic cycle, including long aseismic periods of slip with velocities of the order of millimeters per year, accelerating and decelerating aseismic slip in the interseismic period, and all inertial effects during simulated earthquakes with slip rate of the order of meters per second, and postseismic slip. The fully elastic model ignores the viscous response of the crust and assumes postseismic relaxation in the form of afterslip.

The locations of the repeating sequences in Parkfield are represented as velocity-weakening (VW) patches in our model, embedded in a velocity-strengthening (VS) creeping region, by assigning VW properties, $a - b < 0$, to the patches and VS properties, $a - b > 0$, to the surrounding fault zone. Outside the VS zone, steady sliding with the long-term slip velocity V_{pl} is imposed in order to model the creep of the surrounding fault area. In the simulations, we use fault friction parameters motivated by laboratory experiments. In particular, we test a range of friction properties on the VS creeping segment to study the effects of the postseismic slip. Fault properties and frictional parameters commonly used in simulations are listed in Table 5.1. Specific parameters used for each case are mentioned separately.

Table 5.1: Fault model parameters used for all simulations

Parameter	**Symbol**	**Value**
Shear wave speed	c_{s}	3.0 km s^{-1}
Shear modulus	μ	30 GPa
Loading slip rate	V_{pl}	23 mm yr^{-1}
Reference slip velocity	V_{o}	10^{-6} m s^{-1}
Reference friction coefficient	f_{o}	0.6
Characteristic slip distance in VS region	L_{VS}	120 μm
Effective normal stress in VS region	$\bar{\sigma}_{\mathrm{VS}}$	120 MPa
Rate-and-state parameters in VW region	a, b	0.015, 0.019
Patch diameters	d_{SF}, d_{LA}	38 m, 30 m

We first conduct simulations with only one VW patch, to obtain models that approximately reproduce the source properties of the LA and SF repeaters. We then consider models with two patches to study their interaction.

5.2.2 Choosing VW patch sizes and characteristic slip values

As discussed in the introduction (section 5.1), the anomalously long recurrence times of the repeaters suggest that much of the slip at their location accumulates aseismically (e.g. Chen and Lapusta, 2009). Therefore, in our models, we consider the patch sizes d that results in d/h^* ratio ~1.35, unless stated otherwise.

The observation that the SF and LA repeaters interact allows us to constrain the absolute sizes of the patches. Since the distance between the patches is 60 to 70 m (Nadeau et al., 2004), their size d should be $<$ 70 m for the patches to not overlap, as otherwise the two events would occur together. On the other hand, if the patches are too small, then they are far apart in relation to their size, and their interaction would be suppressed. In Chapter 4, we have established that, in simulated 2D rate-and-state models, the interaction is dominated by the postseismic effects and that the distances at which the two patches would interact similarly to the SF and LA observation are about $2d$. That translates into the source dimension d of about 35 m. With the well-constrained d and a desirable d/h^* of ~1.35, we can then derive the suitable characteristic slip L, the least constrained parameter of the rate-and-state friction from equation (5.4).

Additional smaller patch should rupture more frequently, everything else being equal, and trigger the larger patch. One intriguing observation is that, even though the LA sequence has a smaller average M_{w}, instead of having shorter T_{r} than the SF sequence, it ruptured consistently after each SF event, with the inter-event time of the order of seconds to minutes in general, and occasionally up to months (Figure 5.1b). One possible explanation for this phenomenon is the source dimension of the LA patch (d_{LA}) being below the critical nucleation length scale h^*, such that any seismic rupture can only happen when the patch is perturbed by external forces.

5.2.3 Reproducing higher source stress drops

In the standard rate-and-state friction model, stress drop of a seismic event is found to be about 10% of the representative shear strength $f_{\mathrm{o}}\,\bar{\sigma}^{o}_{\mathrm{VW}}$. In the case of Parkfield repeaters, the effective normal stress is estimated to be ~120 MPa nearby (Lockner et al., 2011). Assuming a typical static friction coefficient of 0.6, the resulting stress drop is ~7 MPa, while values of 25 to 30 MPa are inferred based on observation (Section 5.1). This discrepancy suggests additional factors are needed to reproduce the high stress drops as observed in Parkfield. Possible explanations that we explore in this study include (1) the presence of enhanced coseismic weakening mechanisms,

(2) locally elevated normal stress on the patch, or (3) a combination of 1 and 2. We mainly focus on the end-member explanations (1) and (2).

Model 1: Enhanced coseismic weakening

In Model 1 (called M1 hereafter), we explore the consequences of enhanced coseismic weakening in the form of thermal pressurization (TP) of pore fluid (Lachenbruch, 1980; Noda and Lapusta, 2010; Rice, 2006), in which fluid present in the shear zone is heated during frictional sliding. As a result, the temperature of pore fluid increases and enhances pore pressure. Higher pore pressure leads to lower effective normal stress, reducing the strength of the fault. The effectiveness of thermal pressurization depends on the width of the shearing layer and the diffusion of heat and fluids away from the shear zone. The change of temperature and pressure on the sliding surface is governed by:

$$\frac{\partial T(x,y,z,t)}{\partial t} = \alpha_{th}\frac{\partial^2 T(x,y,z,t)}{\partial y^2} + \frac{\omega(x,y,z,t)}{\rho c}, \tag{5.8}$$

$$\omega = \tau V \frac{\exp(-y^2/2w^2)}{\sqrt{2\pi}w}, \tag{5.9}$$

and

$$\frac{\partial p(x,y,z,t)}{\partial t} = \alpha_{hy}\frac{\partial^2 p(x,y,z,t)}{\partial y^2} + \Lambda\frac{\partial T(x,y,z,t)}{\partial t}, \tag{5.10}$$

where α_{th} and α_{hy} are the thermal and hydraulic diffusivities, ρc is the specific heat capacity, Λ is the pore pressure change per unit temperature change under undrained conditions, $\omega(x,y,z,t)$ is the shear heating source, and w is the half width of the shear zone on the VW patch. The parameters used in M1 are listed in Table 5.2, adopted from Rice, (2006). An estimate of slip L^* needed to achieve appreciable thermal pressurization, obtained for adiabatic and undrained shear heating of a layer of width $2w$, is given by, e.g. Rice, (2006):

$$L^* = \frac{2w\rho c}{f\Lambda}, \tag{5.11}$$

where f is the representative friction coefficient. With parameters chosen in M1, L^* is approximately $4{\cdot}10^{-3}$ m. Since the typical slip in our dynamic event is between 0.05 to 0.07 m, such L^* indicates efficient thermal pressurization and hence strong dynamic weakening on the fault. In our model, the TP is effective in the VW regions; the poroelastic parameters chosen in the VS areas effectively disable the TP there (Figure 5.2a).

Table 5.2: Hydrothermal properties of the VW patch in M1

Parameter	**Symbol**	**Value**
Specific heat	ρc	2.7 MPa/K
Thermal diffusivity	α_{th}	10^{-6} m^2 s^{-1}
Hydraulic diffusivity on VW patch	α_{hy}	10^{-4} m^2 s^{-1}
Undrained $\Delta p/\Delta T$ on VW patch	Λ	1 MPa/K
Half width of shear zone on VW patch	w	0.5 mm

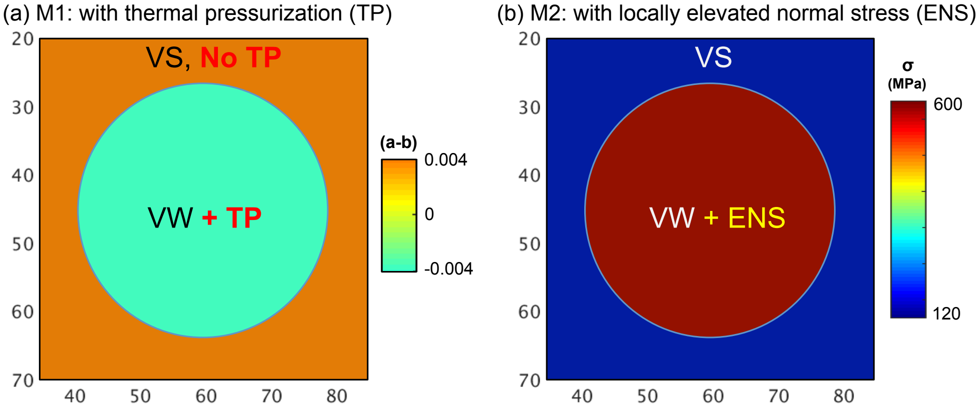

Figure 5.2: *Fault properties in M1 and M2.* For both models, a VW patch with $(a-b)_{\mathrm{VW}} = 0.004$ is embedded in a velocity-strengthening region. (a) In M1, the fault properties are such that thermal pressurization of pore fluids is efficient during seismic events, leading to enhanced coseismic weakening. Outside of the VW patch, TP is inefficient. (b) In M2, normal stress on the VW patch is elevated to represent a flattened asperity; TP is not efficient.

Model 2: Elevated normal stress on the VW patch

The higher stress drop can also be resulted from the higher effective normal stress. Normal stress can vary spatially due to surface roughness or isolated local features. For example, flattened "bumps" or asperities would lead to locally elevated normal stress (ENS); such features have been invoked to explain foreshock-like seismicity in laboratory experiments (McLaskey and Kilgore, 2013).

We explore this possibility in Model 2 (called M2 hereafter), in which we consider the velocity-weakening region to be a flattened asperity with elevated normal stress governed by standard rate-and-state friction. Since stress drop is expected to scale linearly with normal stress in this framework and, as mentioned in the previous section, the average stress drop based on inferred normal stress of 120 MPa in the area is expected to be ~7 MPa, in order to reproduce an average stress drop of 25 to 30 MPa, normal stress on the VW area needs to be much higher; we consider 600 MPa (Figure 5.2b). L of the patch is then selected such that the patch-to-h* ratio is the same as in M1, according to equation (5.4).

5.3 Simulations with a single VW patch

5.3.1 Model M1 with TP

Our first goal is to reproduce the source properties of the SF sequence, which, based on observation, is suggested to be the driving force for the triggering of the LA patch (Zoback et al., 2011). So we start by considering a fault with a single VW patch embedded in a VS region. The diameter of the circular VW patch is 38 m, surrounded by a 160 by 160 m creeping region, a dimension which is a sufficiently large for any seismic wave reflections to attenuate to their minimal effects. We apply this set up in both M1 and M2, and, for each model, two cases are run, with $(a-b)_{\text{VS}}$ = 0.004 and 0.008.

In M1, a homogeneous effective interseismic normal stress of 120 MPa is imposed on the entire fault (Figure 2a). We make TP efficient on the VW patch using the parameters listed in Table 5.2. With L_{VW} = 60 μm, the patch-to-h* ratio is 1.35. For $(a-b)_{\text{VS}}$ = 0.008 (M1-b in Table 5.3, Figure 5.3a), the average magnitude of the repeating events is Mw 2.2, ranging between 2.18 to 2.21. Average T_{r} is ~3.0 years, ranging between 2.7 and 3.2 years, with a standard deviation of 0.19 year. The average diameter of these circular ruptures is 60 m, which is ~50% more than the patch diameter, indicating that the rupture penetrates into the surrounding VS area. The average stress drop for these events is ~34 MPa. For $(a-b)_{\text{VS}}$ = 0.004, source properties are slightly different (M1-a in Table 5.3), because different $(a-b)_{\text{VS}}$ results in different amount of overlap between the seismic rupture and the surrounding creeping area. Thus the model produces events with properties similar to the SF repeaters, hovering on the high end of the range of the observed values.

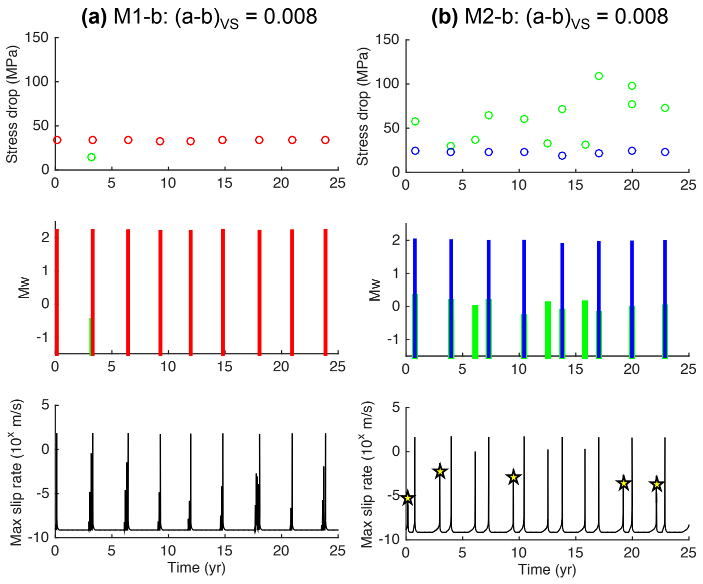

Figure 5.3: *Simulation results for (a) M1-b, (b) M2-b, and (c) M2-d with* $(a-b)_{\mathrm{VS}} =$ *0.008.* (top) Stress drop of seismic events. (middle) M_{w} of seismic events. (bottom) Maximum slip rate on the fault through time. In M2, much smaller events (green lines) than the main sequence (blue lines) occur on the patch. Yellow stars indicate aseismic transients on the patch. M2-d is a simulation with a larger patch-to-h^* ratio of 1.51. It indicates that, as the patch-to-h^* ratio increases, the variability of the main sequence increases in both M_{w} and T_{r}.

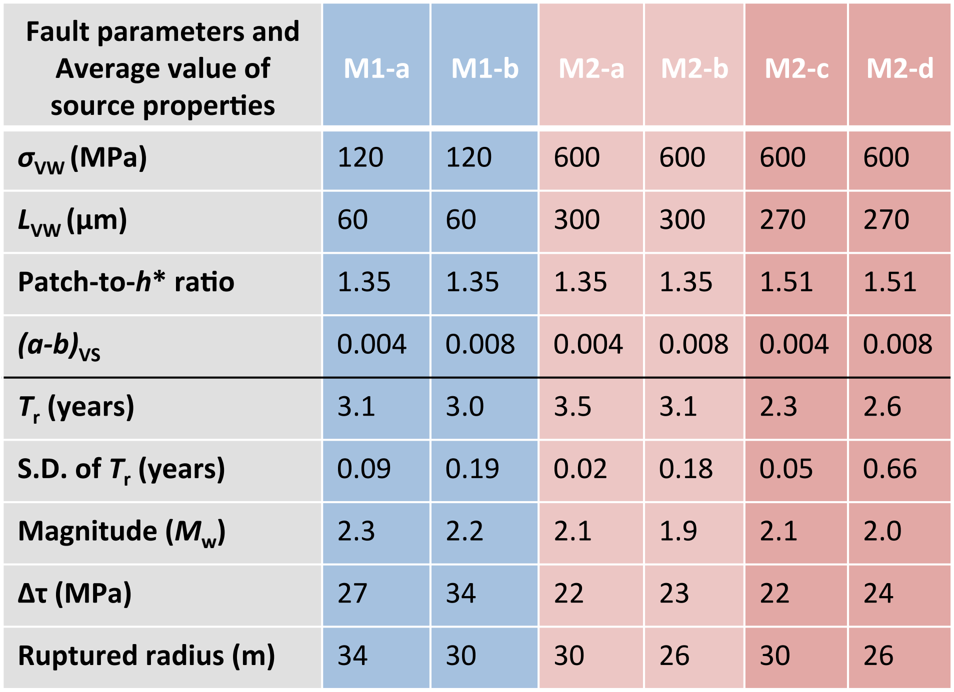

Fault parameters and Average value of source properties	**M1-a**	**M1-b**	**M2-a**	**M2-b**	**M2-c**	**M2-d**
σ_{VW} (MPa)	120	120	600	600	600	600
L_{VW} (μm)	60	60	300	300	270	270
Patch-to-h^* ratio	1.35	1.35	1.35	1.35	1.51	1.51
$(a-b)_{\mathrm{VS}}$	0.004	0.008	0.004	0.008	0.004	0.008
T_{r} (years)	3.1	3.0	3.5	3.1	2.3	2.6
S.D. of T_{r} (years)	0.09	0.19	0.02	0.18	0.05	0.66
Magnitude (M_{w})	2.3	2.2	2.1	1.9	2.1	2.0
Δτ (MPa)	27	34	22	23	22	24
Ruptured radius (m)	34	30	30	26	30	26

Table 5.3: *Fault parameters used in M1 and M2 and properties of the reproduced seismic sources.*

5.3.2 Model M2 with ENS

In M2, the effective normal stress is increased to 600 MPa in the VW region while the TP there is rendered inefficient by choosing appropriate poroelastic properties. The five times larger normal stress is motivated by our attempt to construct a model with a similar stress drop as in M1. L_{VW} is 300 μm in order to retain the same patch-to-h* ratio of 1.35 as in M1. Similarly, a series of repeating event is obtained (M2-a and M2-b in Table 5.3). For $(a-b)_{\mathrm{VS}} = 0.008$, the average magnitude of these events is M_{w} 1.94, ranging from M_{w} 1.86 to 2.00 (Figure 5.3b). The average T_{r} is 3.1 years, ranging from 2.92 to 3.37 years, with a standard deviation of 0.18 year. The average rupture diameter is 52 m and the average stress drop is 23 MPa, which is lower than that in M1-b. In order to produce events with even higher stress drop of 35 MPa as in M1-b, one would need to further enhance the effective normal stress on the VW patch. Note that our simulations indicate that the stress drop does not scale linearly with the effective normal stress of the patch. This is because the rupture exits into the surrounding VS area, and the average stress drop is affected by stress changes there. The results from M2 are also comparable to the observed values.

5.3.3 Model M3 with both ENS and TP

Under a high compressive stress as in M2, one would expect prominent frictional heating of the fault as it slips dynamically. Unless the shear zone is quite broad so that the temperature rise is not significant, enhanced coseismic weakening due to shear heating is likely to take place concurrently. As an example, we consider Model M3, which combines high $\bar{\sigma}^{o}_{\mathrm{vw}} = 480$ MPa and TP on the patch. TP in this case is less efficient compared to that in M1 of section 5.3.1, with $\Lambda = 0.1$ MPa/K and shear zone half-width $w = 10$ mm, as adopted from Noda and Lapusta, (2010). For comparison, we also present M2-like model (M2-e) with $\bar{\sigma}^{o}_{\mathrm{vw}} = 480$ MPa, which is 20% lower than in section 5.3.2. Model M3 is able to reproduce repeating events with an average magnitude of M_{w} 1.9 and an average T_{r} of 2.5 yr, which is smaller but similar to the properties of the events in M1 with more efficient TP and in M2 with $\bar{\sigma}^{o}_{\mathrm{vw}} = 600$ MPa (Table 5.4). For comparison, model M2-e produces events with even smaller magnitudes and stress drops. Somewhat more efficient thermal pressurization in M3 would allow it to produce larger M_{w} and T_{r}.

Average value of main sequence	M3 (M1+M2)	M2-e
σ_{VW} (MPa)	480	480
L_{VW} (µm)	240	240
Patch-to-h* ratio	1.35	1.35
$(a-b)_{VS}$	0.004	0.004
T_r (years)	2.5	2.3
S.D. of T_r (years)	0.05	0.05
Magnitude (Mw)	1.91	1.78
$\Delta\tau$ (MPa)	22	17
Ruptured radius (m)	25	24

Table 5.4: *Comparison between the repeating sequences reproduced in M2-e and M3.* The hydrothermal properties in case (II) are adopted from Noda and Lapusta (2010).

In the following, we focus on the properties of the end-member models M1 and M2, expecting M3-like models to have behavior in between.

5.3.4 Variability due to aseismic slip and smaller seismic events

In both models M1 and M2, due to a low patch-to-h^* ratio of 1.35, there is substantial aseismic slip on the VW patch right before the seismic nucleation of the main repeaters and postseismic slip right after the rupture. The variation in aseismic moment release contributes to the variability in the recurrence interval T_r. For example, in model M1-b, T_r1a and T_r1b is 2.68 years and 3.24 years respectively (Figure 5.4). Despite T_r1a being 20% shorter than T_r1b, the two repeaters (Ea) and (Eb) that occur at the end of T_r1a and T_r1b, respectively, have the same M_w of 2.2 and seismic moment within 2% of each other. Thus longer interseismic interval does not lead to large subsequence seismic moment release (Figure 5.4). This situation is due to a larger portion of total slip being aseismic during T_r1b, with the aseismic slip being ~20% during T_r1a vs ~40% during T_r1b, Figure 5.4).

In addition, in model M2, a number of smaller seismic events and aseismic transients occur on the VW patch during the interseismic periods of the main repeaters. The seismic events, when they occur, have $\sim M_\mathrm{w}$ 0, rupturing a very small area of the VW patch, and they tend to develop into aseismic transients (i.e., postseismic slip) that propagate through the entire VW patch, releasing shear stress on the fault (vertical green lines in Figure 5.3b). Occasionally, there is only an aseismic interseismic

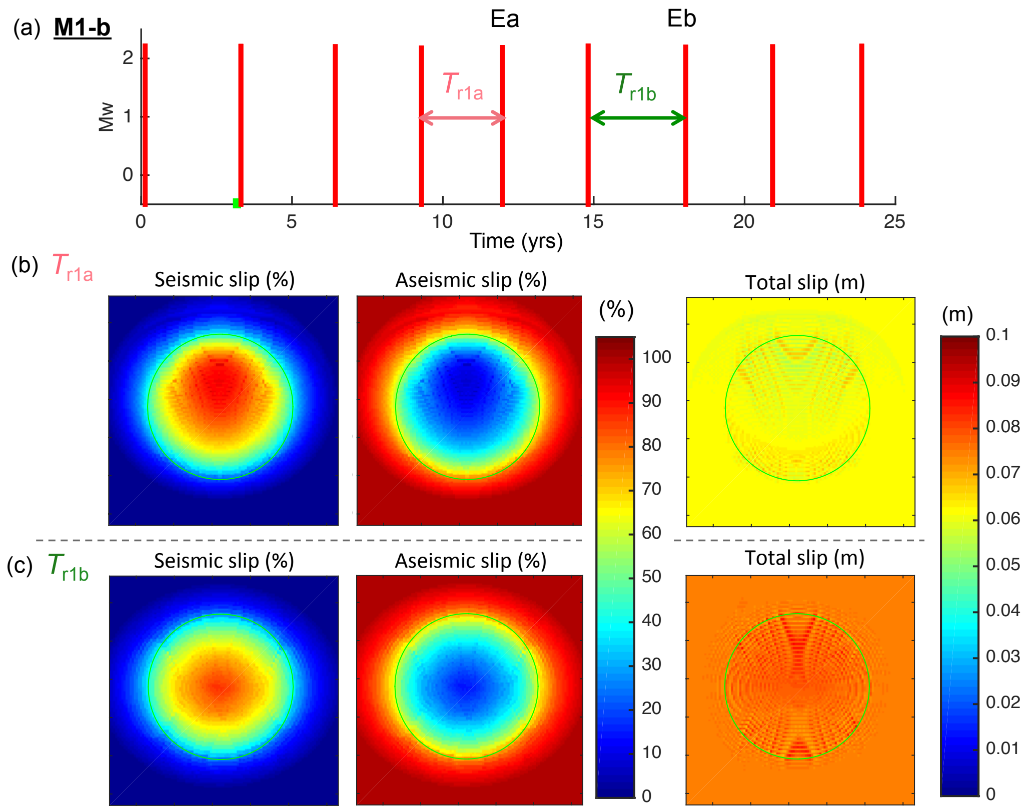

Figure 5.4: *The comparison of the ratio of seismic to aseismic slip in different recurrence periods in M1-b.* (a) M_w-time of events on the VW patch. Red lines represent the main repeating sequences while green lines are seismic events with much smaller magnitude with M_w 0. The fraction of seismic and aseismic slip of the total slip in recurrence interval T_{r1a} and T_{r1b} are displayed in (b) and (c), respectively. The fault dimension shown in each snapshot is 60 m x 60 m.

transient, with no seismic signal (stars in Figure 5.3b). These additional activity further contributes significantly to the moment release on the patch and affects the main repeating sequence. As an example of such an effect, consider the interseismic period between two repeaters marked E1 and E3 in Figure 5.5. After one of the repeaters with M_w 2.0 (E1) occurs, the VW patch returns to being locked and stress slowly accumulates. In the interseismic period, a seismic event with M_w 0.1 occurs (E2). Instead of rupturing the entire VW patch, it causes an aseismic transient propagating through the entire patch with slip rate as high as 10^{-3} m/s. Then the next main repeater occurs (E3). Overall, this recurrence interval is 0.25 yr longer than the previous one (3.13 yr). Despite that, the repeater E3 is smaller in seismic moment than E1 by ~30%, due to the interseismic stress release as described. Note

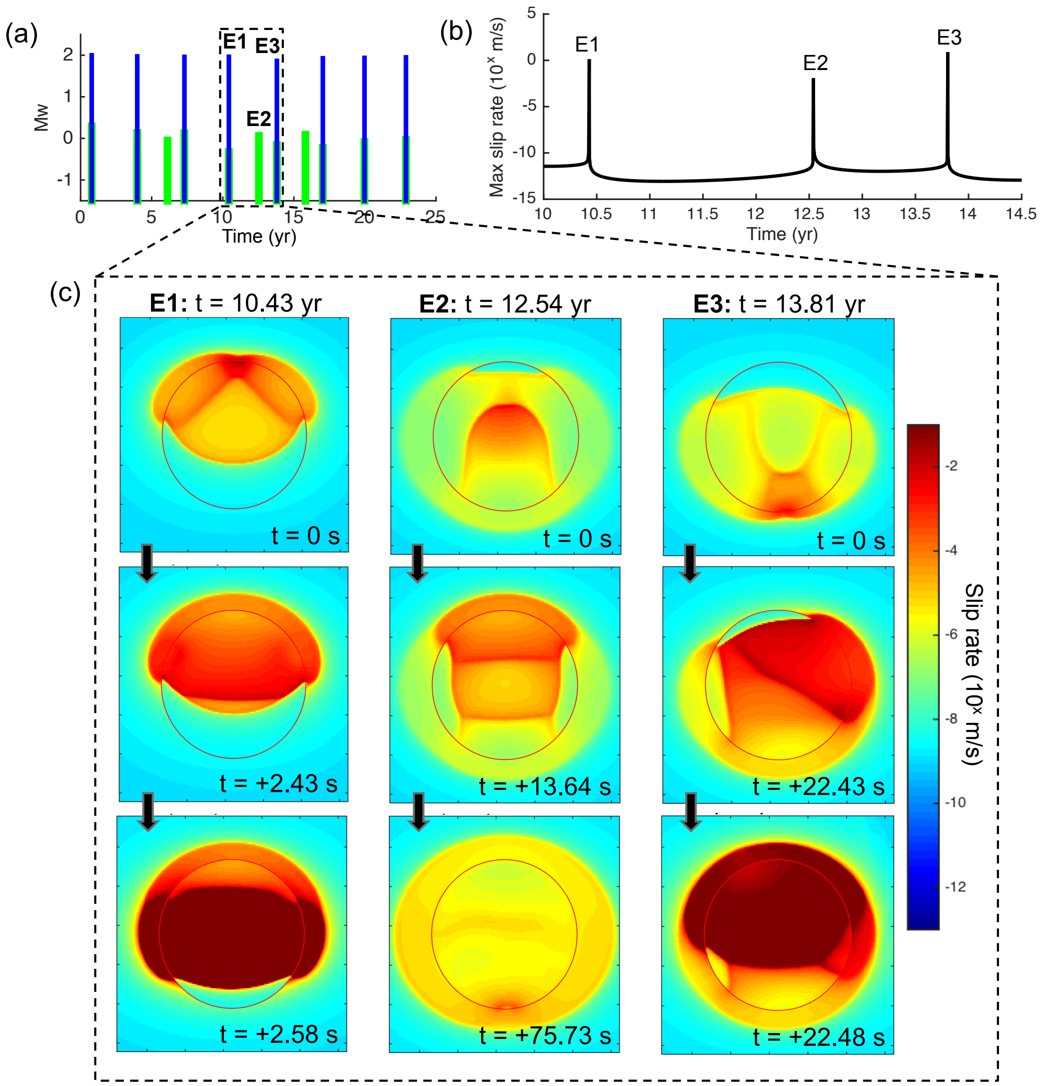

Figure 5.5: *Effect of interseismic events on the repeating sequence in M2-b.* (a) M_w of the events on the patch vs time. Blue lines represent the main repeating sequence while green lines are seismic events with much smaller magnitude. The interseismic period is longer when additional events occur on the patch. (b) Slip velocity at the center of the VW patch between year 10 to 14.5. (c) Snapshots of slip rate on and around the VW patch (red open circle) during events E1-E3, with E1 and E3 being main repeating seismic ruptures and E2 being an additional seismic event followed by an aseismic transient. E2 starts as a small seismic event that sends an aseismic slip transient through the entire patch and releases shear stress during the process. This mostly aseismic additional release of stress explains the longer Tr before E3 occurs, as well as the smaller moment of E3 compared to E1, as quantified in the text. The fault dimension shown in each snapshot is 60 m x 60 m.

that an 8% longer T_r would supposedly imply 8% larger seismic moment of the following repeater, assuming that all slip would be released seismically through the main repeaters. E3 being 30% smaller than E1 means that almost 40% of the seismic moment of E1 is released additionally between the repeaters. The seismic event E2 only contributes 0.4% to the ~40% discrepancy, indicating that most of the extra moment is released aseismically. Thus our model shows that much smaller interseismic events that are associated with relatively large aseismic slip, or completely aseismic transients, can elongate the recurrence time while reducing the moment of the main repeaters of the following events in the main repeating sequence, a counter-intuitive situation which potentially explains why these and other Parkfield repeaters are neither time nor slip predictable (Rubinstein et al., 2012). Another example of such counter-intuitive behavior (Figure 5.6) shows that the main repeater can be larger in size (~30% larger seismic moment of E4 vs E3) despite occurring after a shorter recurrence interval (T_{r2a} = 2.93 yr vs T_{r2b} = 3.38 yr, a 13% difference).

The variability of the recurrence time and moment in M2 is enhanced when L_{VW} is changed from 300 μm to 270 μm and the patch-to-h* ratio increases to 1.51 (M2-b vs M2-d in Table 5.3, Figure 5.3c). For $(a-b)_{\mathrm{VS}} = 0.008$, the average magnitude, stress drop, and rupture radius of the sequence with L_{VW} = 270 μm (M2-d) remain similar to the case of L_{VW} = 300 μm (M2-b) at approximately M_{w} 2.0, 24 MPa and 26 m respectively. However, the average T_{r} is shortened to 2.6 yr, with a larger standard deviation of 0.66 yr. The shorter and more irregular T_{r} is likely due to a different pattern of the smaller seismic events and aseismic transients on the VW patch. The dependence of the variability on the model parameters requires further study. The aseismic slip on the VW patch in M1, though contributing substantially to the total slip, is fractionally smaller than the aseismic slip on the VW patch in M2 (e.g. <40% of total slip in period T_{r1b} vs >65% in T_{r2b}, Figures 5.4 and 5.6), despite the patch-to-h^* ratio being the same at 1.35. This explains why the main repeaters in M1 is larger than those in M2 (M_{w} 2.2 in M1-b vs M_{w} 1.9 in M2-b), despite a shorter average T_{r} (3.0 years in M1-b vs 3.1 years in M2-b) (Figures 5.4 and 5.6). This difference in the fraction of slip released aseismically on the VW patch can be explained by the difference in the physics of the two models and their resulting operation under very different stress conditions. In M1, the efficient coseismic weakening due to TP results in nearly complete stress drop on the patch during main repeaters (red vertical lines in Figure 5.7c). Therefore, for most of the interseismic period, the patch is much below the characteristic slow-rate strength of $f_o\bar{\sigma}^o_{\mathrm{vw}}$, reaching the corresponding stresses only at the end of the recurrence period. In M2, however, the average stress drop on the patch during main repeaters is comparable to ~10% of

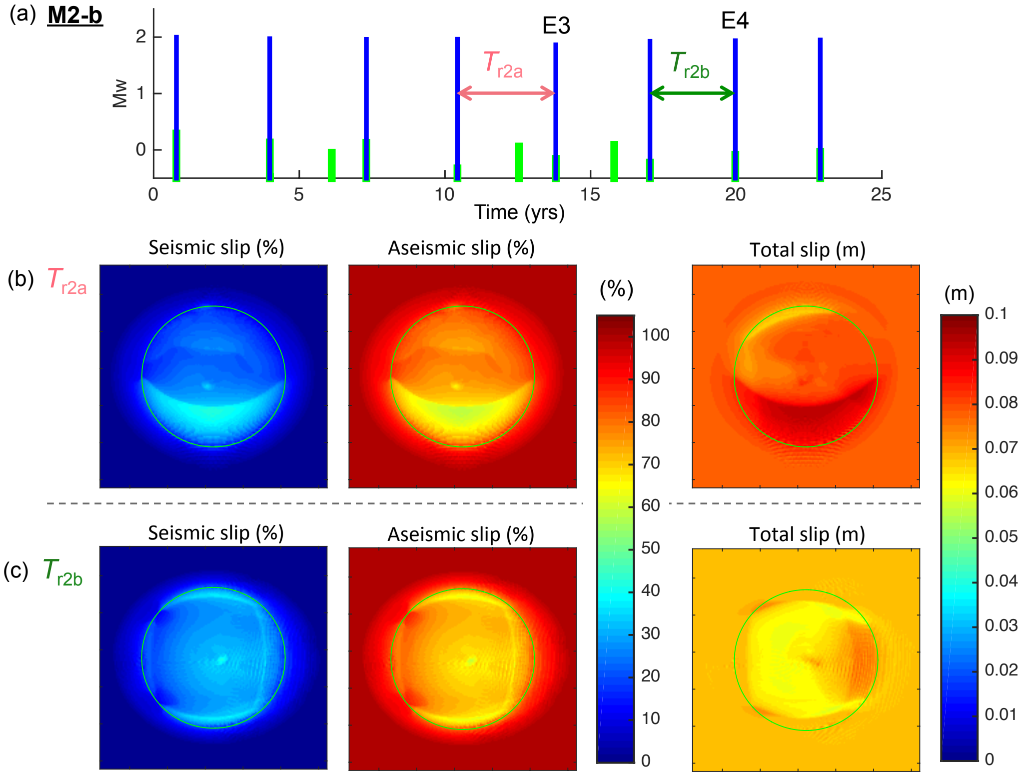

Figure 5.6: *The comparison of the ratio of seismic to aseismic slip in different recurrence periods in M2-b.* (a) M_w-time of events on the VW patch. Blue lines represent the main repeating sequences while green lines are seismic events with much smaller magnitude with M_w 0. The fraction of seismic and aseismic slip of the total slip in recurrence interval T_r2a and T_r2b are displayed in (b) and (c), respectively. The fault dimension shown here is 60 m x 60 m.

$f_o\bar{\sigma}^o_\mathrm{vw}$ (larger blue vertical lines in Figure 5.7c), as expected for this standard rate-and-state model. As a result, the average stresses are closer to the representative slow-rate strength $f_o\bar{\sigma}^o_\mathrm{vw}$ in M2 than M1 for most of the interseismic period, allowing for smaller seismic events in between the main repeaters, interseismic transients and more aseismic slip overall. Note that M2 operates at a much higher level of shear stress because of the higher $\bar{\sigma}^o_\mathrm{vw}$ at 600 MPa (vs $\bar{\sigma}^o_\mathrm{vw}$ = 120 MPa in M1). That is why the absolute magnitude of stress drop in M2 is similar to that in M1, although the stress drop in m2 is significantly smaller in comparison to the representative fault strength $f_o\bar{\sigma}^o_\mathrm{vw}$.

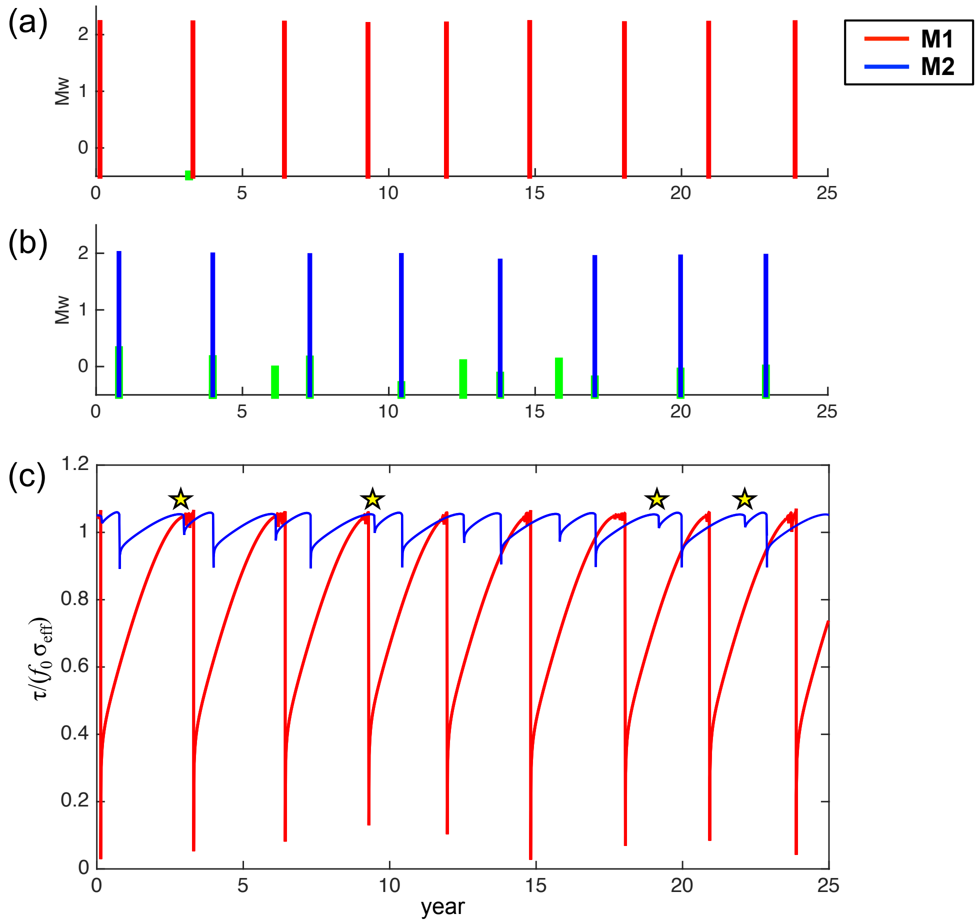

Figure 5.7: *Comparison of the average shear stress on the VW patch in M1 and M2.* (a-b) M_w vs time of seismic events in M1 and M2. (c) Evolution of shear stress relative to the representative rate-and-state fault strength $f_o\bar{\sigma}^o_{\mathrm{vw}}$ in models M1 and M2. In M1, the stress drop of the main repeaters is comparable to $\bar{\sigma}^o_{\mathrm{vw}}$, while the stress drop of the main events in M2 is a much smaller ($\sim$10%) portion of the fault strength. As a result, the shear stress of the patch in M2 remains close to the fault strength and hence additional small seismic events and aseismic transients (yellow stars) can occur.

5.3.5 Scaling relation between T_r and M_o

Nadeau and Johnson, (1998) reported that the repeating earthquakes along the creeping section of the San Andreas fault have an unexpected scaling relation between T_r and M_o: $T_\mathrm{r} \propto M_\mathrm{o}^{1/6}$ (solid black line Figure 5.8). This scaling indicates a weaker dependence of T_r on M_o than the theoretically derived relation $T_\mathrm{r} \propto M_\mathrm{o}^{1/3}$, which assumes the absence of aseismic slip at the location of the repeaters; furthermore, the observed recurrence intervals are much longer (solid light blue line in Figure 5.8) than the standard model assuming a constant 3-MPa stress drop. Chen and Lapusta,

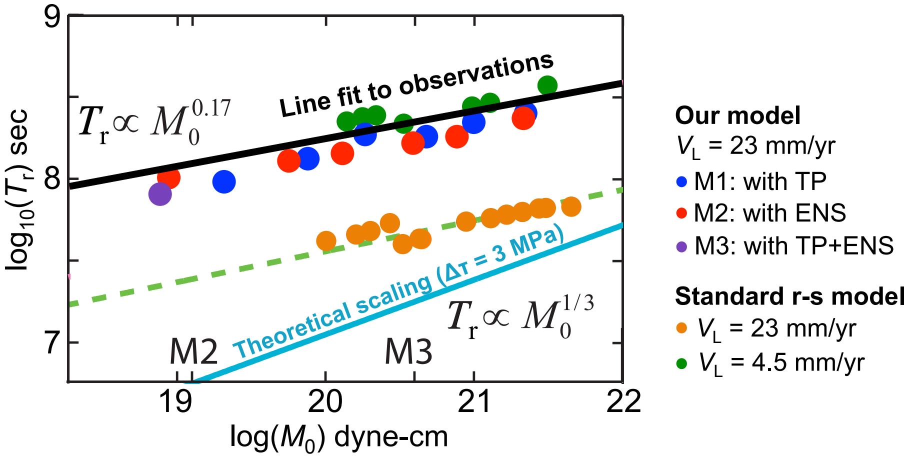

Figure 5.8: *T_r vs M_o for the repeating events in M1 (blue dots), M2 (red dots), and M3 (purple dots).* Results of models M1-M3 fit the T_r-M_o relation as observed in Parkfield (black solid line). The results from the standard rate-and-state fault model of Chen & Lapusta (2009) are indicated as green and orange dots for V_{pl} = 4.5 and 23 mm yr^{-1}, respectively, illustrating that a lower V_{pl} = 4.5 mm yr^{-1} is required for a good fit in that study. The theoretical T_r-M_o relation for the constant stress drops of 3 MPa is shown as light blue line for comparison.

(2009) found that the observed scaling relation can be reproduced with the standard rate-and-state fault model due to the presence of aseismic slip on the patches, if the background slip rate is much lower at 4.5 mm yr^{-1} (green dots in Figure 5.8), which is in agreement with previous studies (Anooshehpoor and Brune, 2001; Beeler et al., 2001). However, the stress drops of these events in Chen & Lapusta study are approximately 7 MPa, which is lower than the inferred values for the LA and SF repeaters.

To check whether models M1 and M2 are capable of reproducing the observed T_r-M_o scaling relation, we vary the patch size to obtain repeating events ranging from M_w 2 to 4 (blue and red dots in Figure 5.8). Note that V_{pl} = 23 mm yr^{-1} in our models. We find that both models indeed reproduce the observed scaling as well as the absolute values of the recurrence times. This is because our events have stress drops around 25 to 35 MPa, ~4-5 times higher than those in Chen and Lapusta, (2009), as discussed in sections 5.3.1 and 5.3.2. That is why they occur less frequently even for loading rate of 23 mm yr^{-1}, something the standard rate-and-state modeling of Chen and Lapusta could not achieve. However, the underlying reason for the different scaling exponent is the same as in Chen and Lapusta, (2009), which is the presence of significant aseismic slip on the patches, the fraction of which decreases as the patch, and hence patch-to-h* ratio, increases. Therefore, one can reproduce the observed scaling in two ways: (1) larger stress drops of ~30 MPa and inferred large-scale creeping rate of V_{pl} = 23 mm yr^{-1} as in our models M1-M3, or (2) more typical stress drops of ~7 MPa based on standard rate-and-state friction and smaller, at least locally, surrounding creeping rate of 4.5 mm yr^{-1} as in Chen and Lapusta, (2009).

5.4 Simulations with two velocity-weakening patches

Following the reproduction of high stress drops of these repeaters and the comparison of the two models, we extend our study to reproducing the interaction of the actual repeating sequences in Parkfield. From 1985 to 2004, the SF and LA patches each ruptured 7 times, with the average magnitude of M_{w} 2.06 and 1.84 respectively (Figure 5.1b). Since the two sequences are 60 - 70 m apart, the two patches should be under the same background loading rate (V_{pl}) of 23 mm yr^{-1}.

In the two-patch simulations, we consider two cases: (I) M1-double, in which both patches are described by model M1 with enhanced coseismic weakening, and (II) M2-double, in which both patches have M2 character of $\bar{\sigma}^{o}_{\mathrm{vw}}$ elevated to 600 MPa. In both cases, the patch diameters of the SF (d_{SF}) and LA (d_{LA}) repeaters are 38 m and 30 m, respectively (Figure 5.9). They share the same rate-and-state frictional properties except for different L, such that d_{SF} = 1.35 h^{*}_{SF} and d_{LA} = 0.9 h^{*}_{LA}. The centers of the two patches are separated by 60 m, which is ~1.8 d_{avg}. For both M1-double and M2-double, we two scenarios with different frictional properties on the VS region, i.e. $(a-b)_{\mathrm{VS}}$ = 0.004 and 0.008.

Both models, M1-double and M2-double, are capable of reproducing the interaction of the two sequences (Figure 5.10). As the SF patch ruptures, it sends a strong postseismic creep propagating to the neighboring LA patch, which triggers a rupture on the LA patch. Both patches become locked afterwards. The SF patch experiences occasional aseismic transients between its repeaters. The LA patch creeps with slip rates oscillating around V_{pl}, unable to nucleate an event due to its subcritical size. The source properties of the resulting repeaters depend on the value of $(a-b)_{\mathrm{VS}}$ and, for $(a-b)_{\mathrm{VS}}$ = 0.004 and 0.008, are close to the observed values (Table 5.5). (The role of frictional properties of the creeping segment is discussed in more detail in section 5.4.2.)

The models reasonably reproduce the source properties of the repeaters. In both

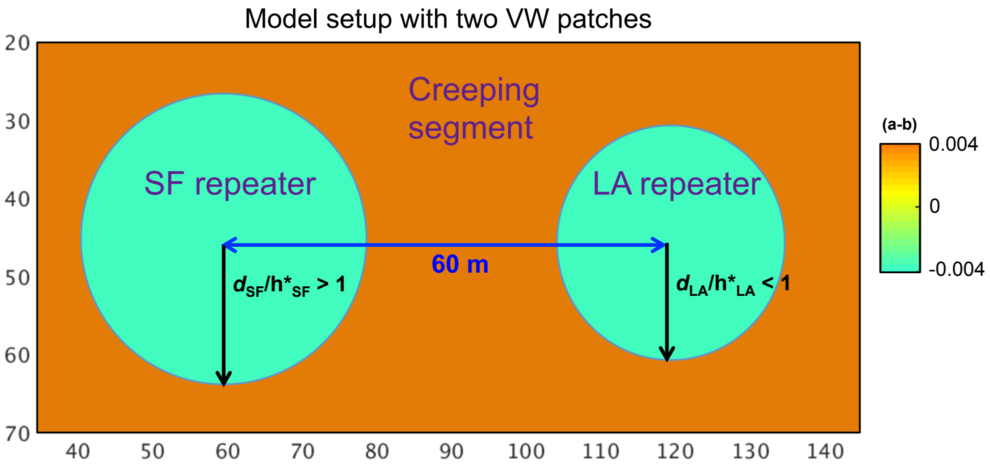

Figure 5.9: *Example of model set up for simulating the SF and LA repeating sequences.* The sequences are represented by two VW patches. The diameter of the SF and LA patches is 38 m and 30 m, respectively. The centers of the two patches are separated by 60 m, i.e. 1.8 d_{avg}. Frictional properties are the same as those in the single-patch cases. The LA patch is slightly below the critical nucleation size such that it can only slip seismically with external stress perturbation.

M1-double and M2-double, the stress drop of the SF sequence lies within the observed range as reported in Abercrombie, (2014), while that of the LA sequence is above that. However, Abercrombie noted that the stress drops resolved for the LA sequence are less reliable due to the spectra of the cluster not being fitted by simple source models, and are probably underestimated. So we do not pursue a better match here; to obtain the lower stress drops of the LA repeater, we would need to reduce the efficiency of TP there for M1-double and reduce $\bar{\sigma}^o_{\text{VW}}$ for M2-double. Most cases result in reasonable values of M_{w}, T_{r}, and triggering time. An example is shown in Figure5.11a. The only outlier is M2-double with $(a-b)_{\text{VS}} = 0.004$, which has a highly variable T_{r} of the LA sequences and hence a larger average T_{r} (Figure 5.11b). In this case, a significant fraction of slip on the LA patch is released either aseismically or through smaller seismic events. Note that the values in M1-double and M2-double can be adjusted slightly by changing the dimensions and properties of the VW patches as well as the properties of the VS area, so that all four cases in Tables 5.5 can likely be made to match the properties more precisely.

5.4.1 Effect of interactions among VW patches

Another interesting result in the model with two patches is that the variability in T_{r} of the SF patch found in the single-patch case (M1-d) is reduced, likely due to

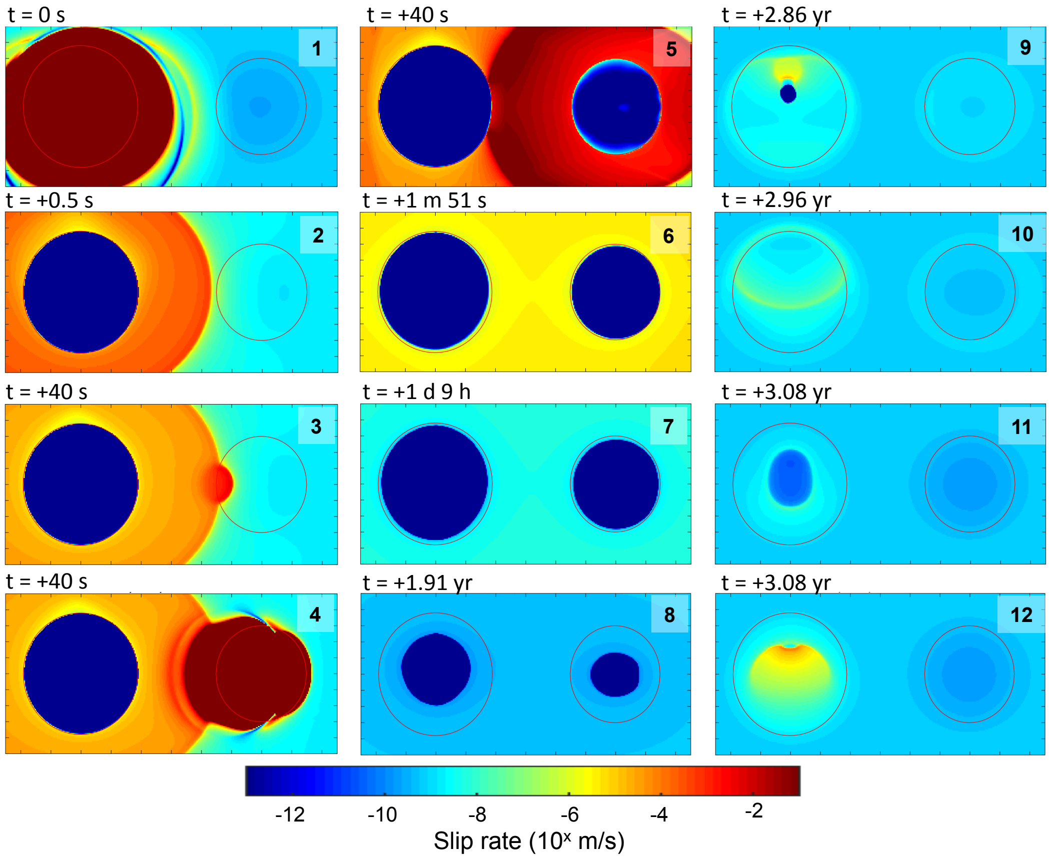

Figure 5.10: *Example of the interaction between the SF and LA events, from M1-double with* $(a - b)_{\mathrm{VS}}$ *= 0.004.* The fault dimension shown in each snapshot is 110 m x 50 m. SF patch ruptures at t = 0s (panel 1), sending a postseismic creeping front to the neighboring LA patch (panels 2 & 3). The creeping front acts as a strong perturbation by increasing the shear stress on the LA patch (Lui and Lapusta, 2016) and hence triggers a seismic rupture there (panels 4 & 5). The rupture of the LA patch is intensified by the enhanced creeping on the VS region between the two patches, but it does not back-trigger the SF patch, whose fault strength is still low after its own event. Both patches become locked after their events, and slip rate of the VS region returns to V_{pl} (panels 6-8). During the interseismic period, an aseismic transient occurs on the SF patch (panels 9 & 10). The SF patch eventually ruptures again (panels 11 & 12).

the interaction with the LA patch. The standard deviation of T_{r} for the SF patch reduces from 0.66 yr in a single-patch case (M1-d) to 0.14 yr in a two-patch case, M2-double (Figure 5.12a and b). This result is surprising, because one would expect the interaction with the additional LA patch to further enhance the variability in T_{r} instead of reducing it. To study the robustness of this result, we considered several other models with slightly different friction properties of the LA patch as well as the

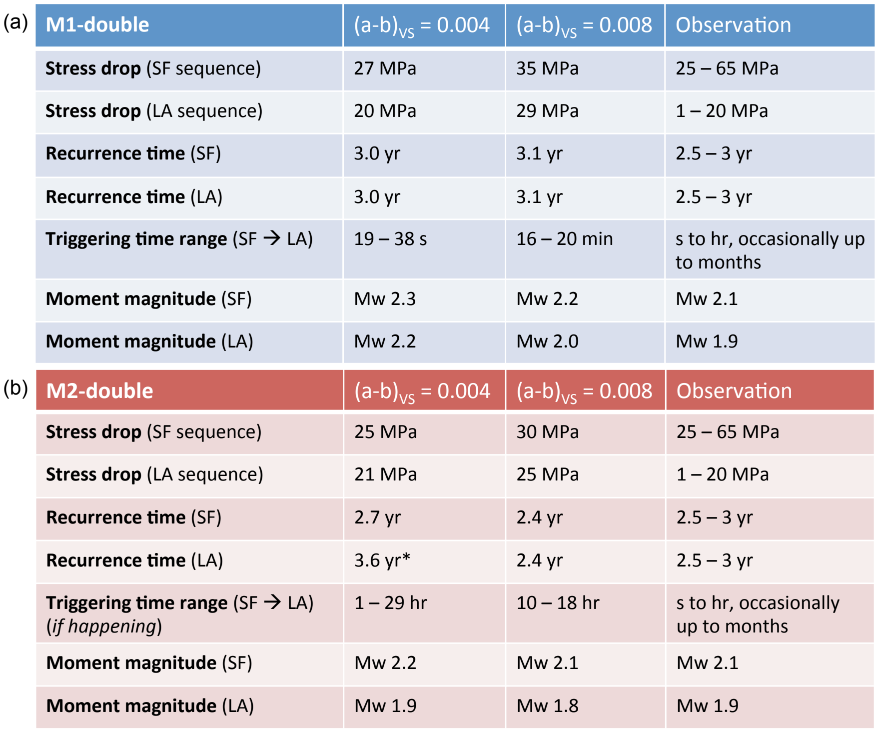

(a)

M1-double	$(a\text{-}b)_{VS}$ = 0.004	$(a\text{-}b)_{VS}$ = 0.008	Observation
Stress drop (SF sequence)	27 MPa	35 MPa	25 – 65 MPa
Stress drop (LA sequence)	20 MPa	29 MPa	1 – 20 MPa
Recurrence time (SF)	3.0 yr	3.1 yr	2.5 – 3 yr
Recurrence time (LA)	3.0 yr	3.1 yr	2.5 – 3 yr
Triggering time range (SF → LA)	19 – 38 s	16 – 20 min	s to hr, occasionally up to months
Moment magnitude (SF)	Mw 2.3	Mw 2.2	Mw 2.1
Moment magnitude (LA)	Mw 2.2	Mw 2.0	Mw 1.9

(b)

M2-double	$(a\text{-}b)_{VS}$ = 0.004	$(a\text{-}b)_{VS}$ = 0.008	Observation
Stress drop (SF sequence)	25 MPa	30 MPa	25 – 65 MPa
Stress drop (LA sequence)	21 MPa	25 MPa	1 – 20 MPa
Recurrence time (SF)	2.7 yr	2.4 yr	2.5 – 3 yr
Recurrence time (LA)	3.6 yr*	2.4 yr	2.5 – 3 yr
Triggering time range (SF → LA) (*if happening*)	1 – 29 hr	10 – 18 hr	s to hr, occasionally up to months
Moment magnitude (SF)	Mw 2.2	Mw 2.1	Mw 2.1
Moment magnitude (LA)	Mw 1.9	Mw 1.8	Mw 1.9

Table 5.5: *Source properties of the seismic sources in models M1-double and M2-double.* * The LA patch has longer average T_r than the SF patch because it is not triggered seismically every time when the SF patch ruptures. For details, see Figure 5.11

VS region. We find that the variability come back in some of them. For example, in a model with a lower patch-to-h* ratio (0.89) of the LA patch, the LA patch exhibits much more irregular seismic and aseismic behavior, and this increased complexity caused more irregularity of the SF patch (Figure 5.12c). Note that the variability of the LA sequence in this case is overshot compared to the observation. A closer match will likely be recovered if the d_{LA}-to-h* ratio is slightly adjusted. Nonetheless, the standard deviation of T_r of the SF patch increases to 0.37 yr in this case, and there is more variability in the seismic moment than even in the one-patch case . This finding shows that irregularity can exists in the two-patch simulations as well.

Note that the variability in LA and SF patch behavior can be due to reasons external to the SF and LA patches. Thus nearby sources of seismic and aseismic perturbation can significantly influence the behavior of SF and LA repeaters and need to be systematically explored. For example, we find that introducing an additional VW patch (called P3 hereafter) to the model dramatically changes the seismic pattern of

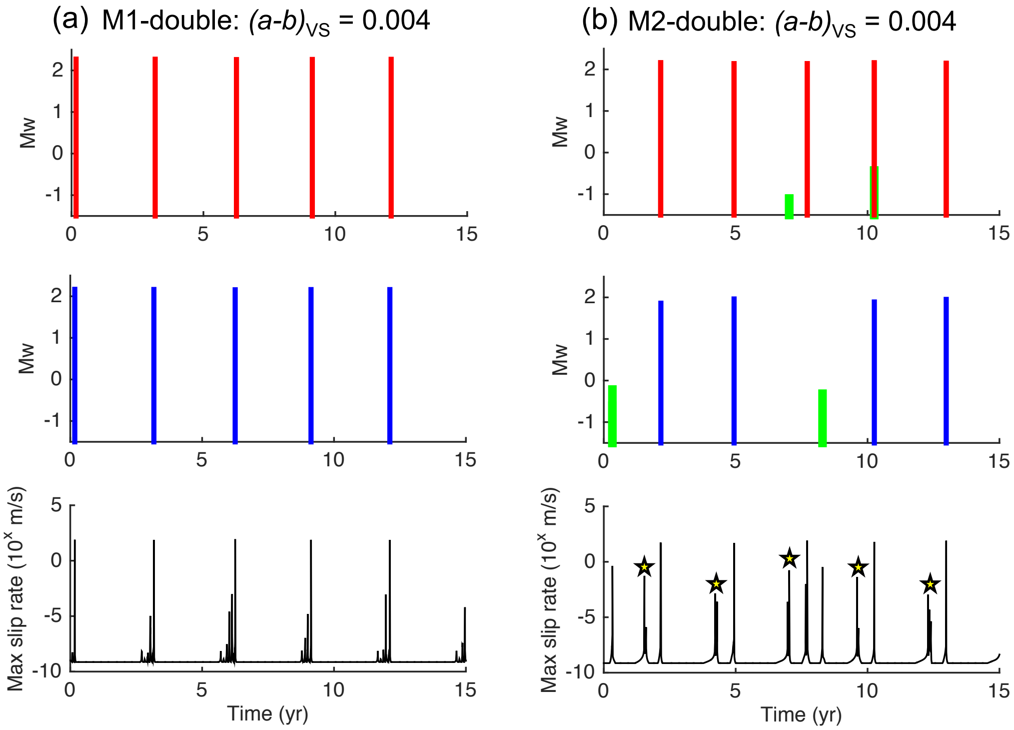

Figure 5.11: *Interactions between the SF and LA patch in models (a) M1-double and (b) M2-double, with* $(a-b)_{\mathrm{VS}}$ *= 0.004.* (first & second row) M_{w} of the seismic events vs time on the SF and LA patch, respectively. (third row) The maximum slip rate on the fault vs time. Yellow stars indicate occasions when the LA patch undergoes asiesmic transients.

the repeaters. If P3 is imposed as a patch in M1-double-$(a-b)_{\mathrm{VS}}$=0.004, with a diameter d_{P3} 16 m > h^*_{P3} (Figure 5.13a), then P3 acts as an independent repeating sequence with a smaller average M_{w} of ~1.37 and a semi-regular T_{r} of ~6 months. Surprisingly, the presence of this additional repeater actually turns off the interaction between the SF and LA patches until much later in the simulation (Figure 5.13b). For instance, in year 3 of the simulation, the SF patch ruptures shortly after an event on P3. However, it only causes an aseismic creep on the LA patch and not a seismic event (Figure 5.13c).

If P3 is moved slightly closer to both the SF and LA repeaters, d_{P3} = 16 m < h^*_{P3}, then throughout most of the simulation time, P3 ruptures together with the SF patch, except for two instances between years 8 and 12 (Figure 5.14b). The combined rupture produces a bigger event, but it does not always trigger a seismic event on the LA patch (Figure 5.14c and d). As a result, there is also obvious disruption of

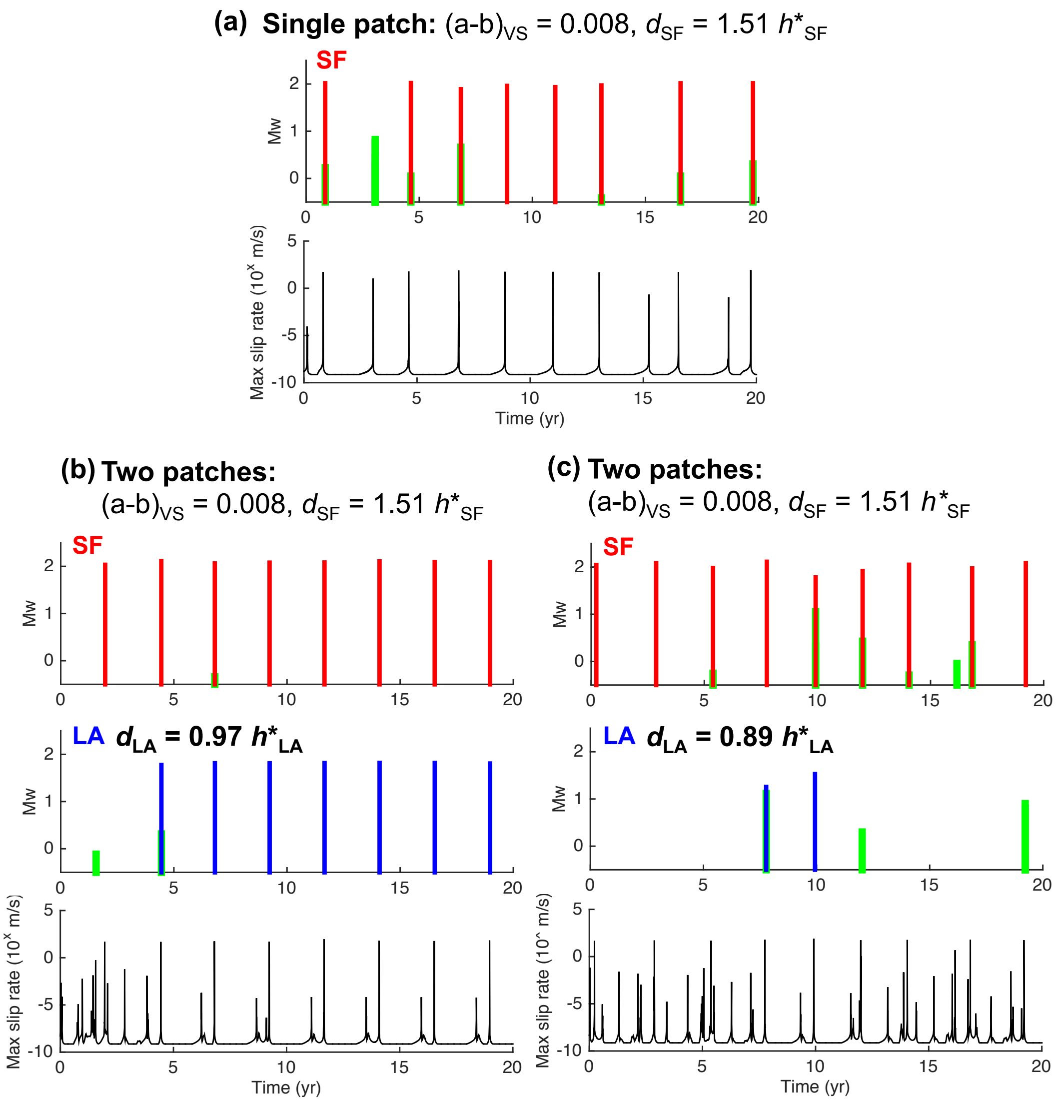

Figure 5.12: *Comparison of the interaction among VW regions between single-patch and double-patch cases.* (a,top) M2-d: M_w of seismic events on the SF patch vs time in a single-patch simulation. (a,bottom) The maximum slip rate on the fault vs time. (b-c, top & middle row) M_w of seismic events on the SF and LA patch, respectively, in M2-double simulations with different frictional properties on the LA patch. (b-c, bottom) The maximum slip rate on the fault vs time. There are some variations in M_w and T_r in (a), but such variability reduces in (b) with the additional LA patch. For a fault with a more stable LA patch, i.e. lower patch-to-h^* ratio, the complex behavior of the LA patch allows some variations in the SF patch to survive.

the SF-LA interaction in this case (Figure 5.14).

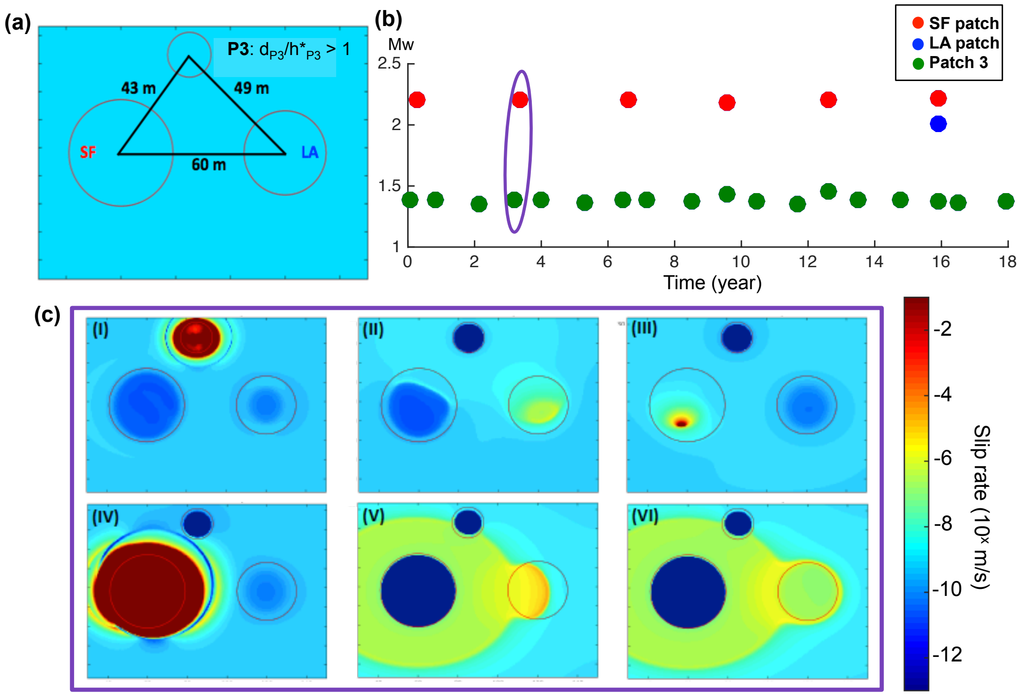

Figure 5.13: *Source properties of the repeaters in models with a larger extent of spatial heterogeneity.* (a) The positions of the 3 VW region on the creeping fault. Patch 3 (P3) can self nucleate and is spatially closer to the SF patch than the LA patch. (b) M_w of the seismic events on the fault vs time. The presence of P3 substantially changes the interaction between the SF and LA sequence. (c) Snapshots of one episode on the fault as circled in (b). P3 ruptures and causes part of the SF patch to slip faster. Eventually the SF patch ruptures, which sends a postseismic creep front to the neighboring LA patch and causes an aseismic transiet there, instead of a main event. The fault dimension shown in each snapshot is 120 m x 90 m.

5.4.2 Effect of frictional properties of the creeping segment

Previous studies have shown that the interaction of earthquake sequences is dependent on or even dominated by stress perturbation caused by postseismic processes (Jiang and Lapusta, 2016; Johanson and Bürgmann, 2010; Lui et al., 2016). As illustrated by Figure 8, the postseismic slip front generated by the SF rupture effectively triggers the LA patch; its domination in the triggering process has been establish in Chapter 4. Here we explore how the creeping front and the main events in the two-patch models are affected by the properties of the velocity-strengthening creeping segments, as well as how, in return, the source and interaction information may be used to constrain the frictional properties of the creeping segment.

The behavior of the postseismic creep is heavily dependent on the frictional properties of the creeping segment. When the creeping region becomes increasingly

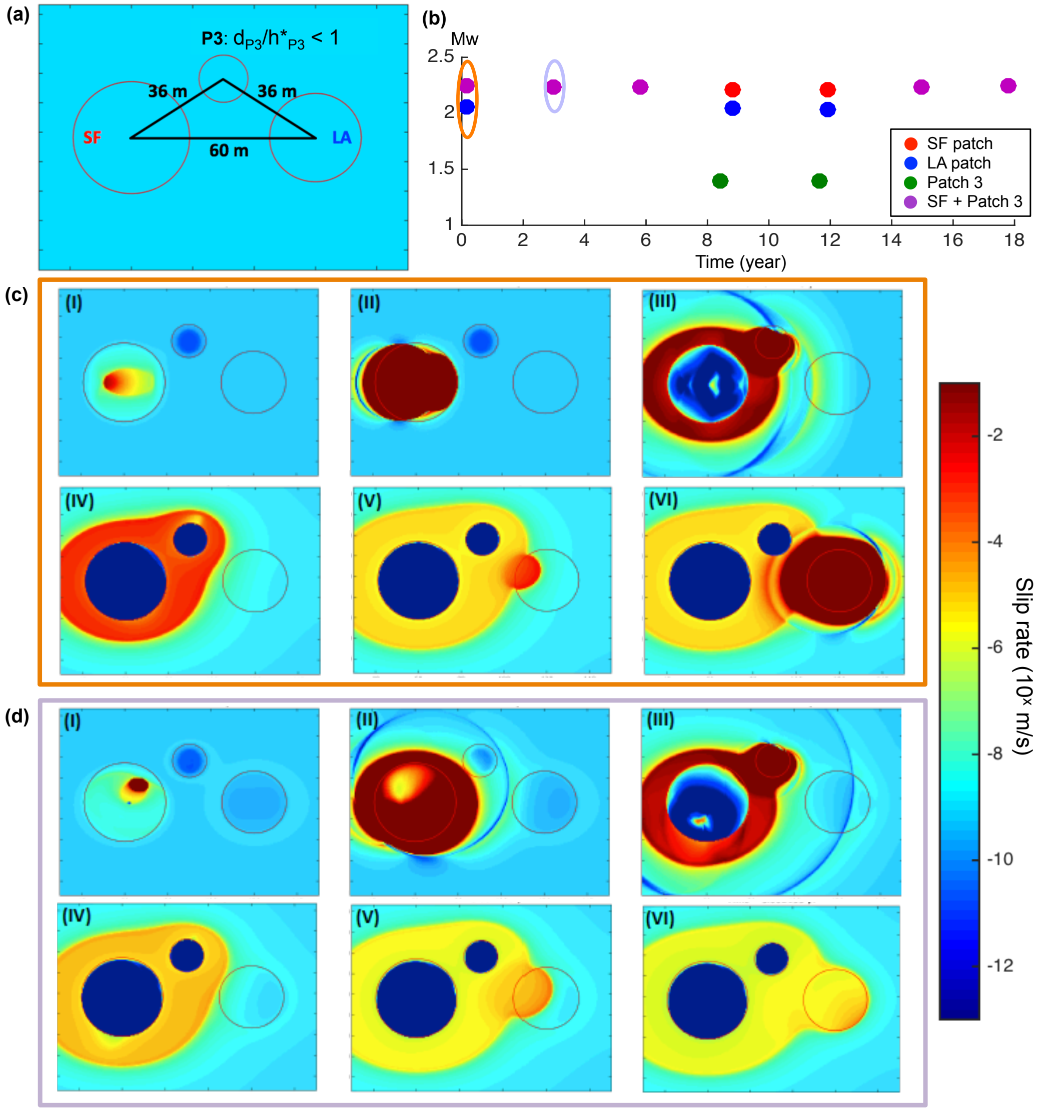

Figure 5.14: *Another example illustrating the effect of spatial heterogeneity on faults.* (a) Model setup: P3 has subcritical patch size and is positioned closer to both the SF and LA patch. (b) M_w of earthquakes on the fault vs time. P3 tends to rupture together with the SF patch (purple markers), resulting in a larger event. Again, the SF-LA interaction is changed significantly, i.e. the LA patch is not always triggered seismically. (c and d) Snapshots of the episodes circled in (b). In both scenarios, the SF patch and P3 rupture together as a single event, but the LA patch responds differently in each case. The fault dimension shown in each snapshot is 120 m x 90 m.

velocity-strengthening, both the velocity of the propagating front and the maximum slip rate of the postseismic creep decrease as it moves away from the ruptured patch (Figure 5.15). In the case of $(a-b)_{\text{VS}} = 0.004$, the creeping front reaches 1.15 d_{SF} within 15 seconds, while it takes up to 10 minutes when $(a-b)_{\text{VS}} = 0.008$ (Fig-

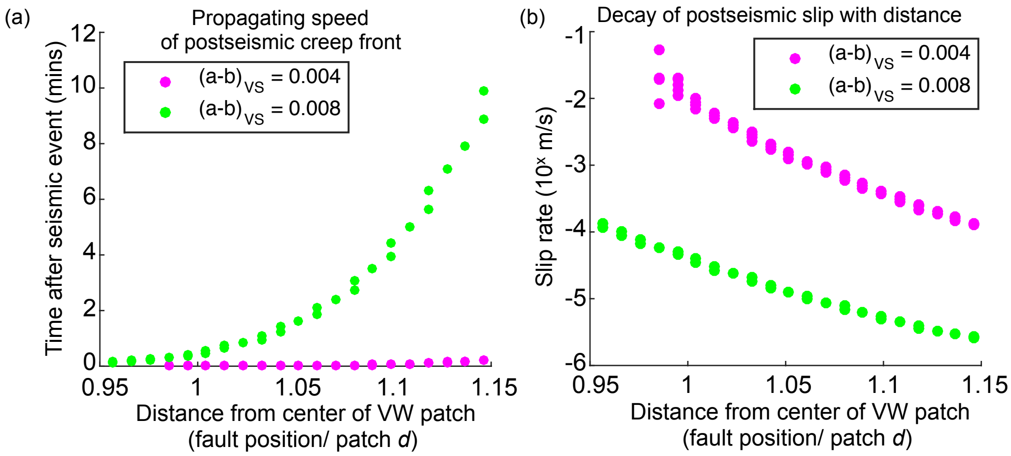

Figure 5.15: *Dependence of the postseismic creep on the frictional properties of the VS region.* (a) Postseismic creeping front propagates faster when the VS region is less velocity-strengthening. (b) The maximum slip rate of the creeping front is significantly smaller when the VS region is more velocity-strengthening. For $(a-b)_{\mathrm{VS}} = 0.004$, postseismic slip rate is in general 2 orders of magnitude larger than that for $(a-b)_{\mathrm{VS}} = 0.008$.

ure 5.15a). Also, when the postseismic slip front is over 1.15 d_{SF} away from the SF patch center, its slip velocity is generally two orders of magnitude smaller for a more velocity-strengthening creeping segment of $(a-b)_{\mathrm{VS}} = 0.008$ (Figure 5.15b). The postseismic creep front almost disappears for a strongly velocity-strengthening creeping segment with $(a-b)_{\mathrm{VS}} = 0.032$ (Figure 5.16). Note that such a value of $(a-b)_{\mathrm{VS}}$ is on the high side of the ones observed experimentally (Blanpied et al., 1991). We use it to show that, on such a velocity-strengthening segment, the postseismic creep front attenuates completely within 1 d_{SF} from the center of the SF patch. It only triggers a mild aseismic transient on the neighboring LA patch 11 hours after the SF event.

In fact, the creeping segment affects not only the postseismic slip on it, but also the seismic sources caused by the VW patches. (Figure 5.17). In M1-double, the case with $(a-b)_{\mathrm{VS}} = 0.004$, the rupture diameter of the SF event is 70 m, which is almost twice of the actual SF patch size of 38 m (Figure 5.17a). For $(a-b)_{\mathrm{VS}} = 0.008$, the stronger creeping region suppresses seismic slip more and d_{rup} is 60 m (Figure 5.17b). Similar effects occur in M2-double. The change in the source dimensions due to $(a-b)_{\mathrm{VS}}$ values leads to different average stress drops. For example, for M1-double, the maximum stress drop in the VW patch is similar, at approximately 70 MPa for both values of $(a-b)_{\mathrm{VS}}$. However, the case with $(a-b)_{\mathrm{VS}}$

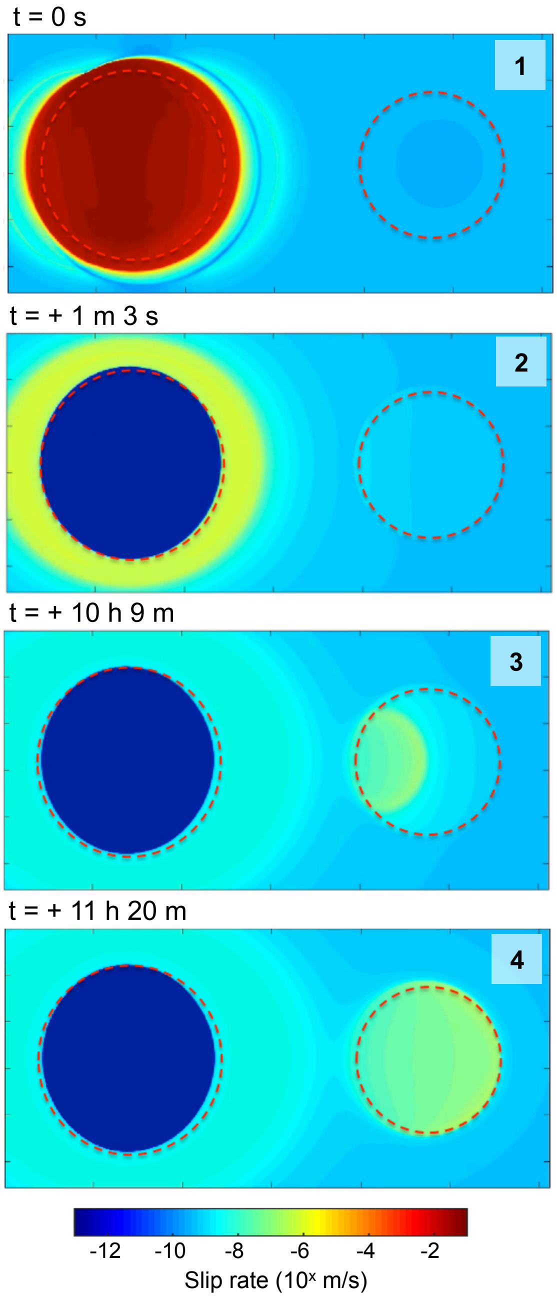

Figure 5.16: *Suppression of the postseismic creep on a strongly velocity-strengthening segment with* $(a-b)_{\mathrm{VS}} = 0.032$*.* The postseismic slip is much weaker compared to $(a-b)_{VS} = 0.008$ (Figure 5.10) It causes only a mild increase in creeping rate upon its arrival on the LA patch, which is not sufficient to trigger a seismic event. The fault dimension shown in each snapshot is 110 m x 50 m.

= 0.008 results in higher stress drop of 35 MPa because of a smaller rupture area, as delineated by the light blue circle (Figure 5.18a and b). Comparing the two models

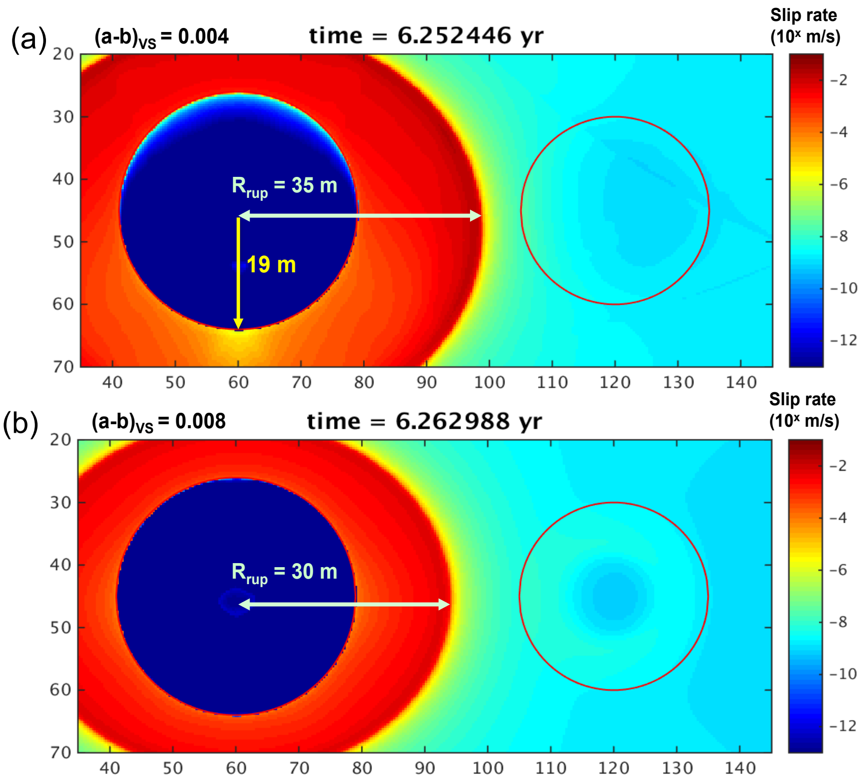

Figure 5.17: *Frictional properties of the creeping segment significantly affect the source properties of the repeaters.* (a-b) Snapshots of slip rate on the fault, with $(a-b)_{\text{VS}} = 0.004$ and 0.008, respectively. $d_{\text{rup}} = 2R_{\text{rup}}$. In both cases, seismic slip of the main event penetrates into the VS region. But the extent of penetration is smaller for larger $(a-b)_{\text{VS}}$.

with the inferred stress drop for one of the SF events by Dreger et al., (2007), the magnitude of stress drop is similar indeed, but the source in real life may have a more complex geometry, which would lead to a more heterogeneous distribution of stress change (Figure 5.18c). Stress change on the SF patch in M1-double is spatially more homogeneous and can be considered as a smoothened version of the observations.

5.5 Conclusion

In this study, we have developed rate-and-state fault models that reproduce the source characteristics and interaction of the SF and LA repeating microearthquakes in the Parkfield creeping segment of the San Andreas Fault. The models are based on rate-and-state friction and incorporate steady-state VW patches embedded into a larger steady-state VS fault region. One of the goals of our modeling is to

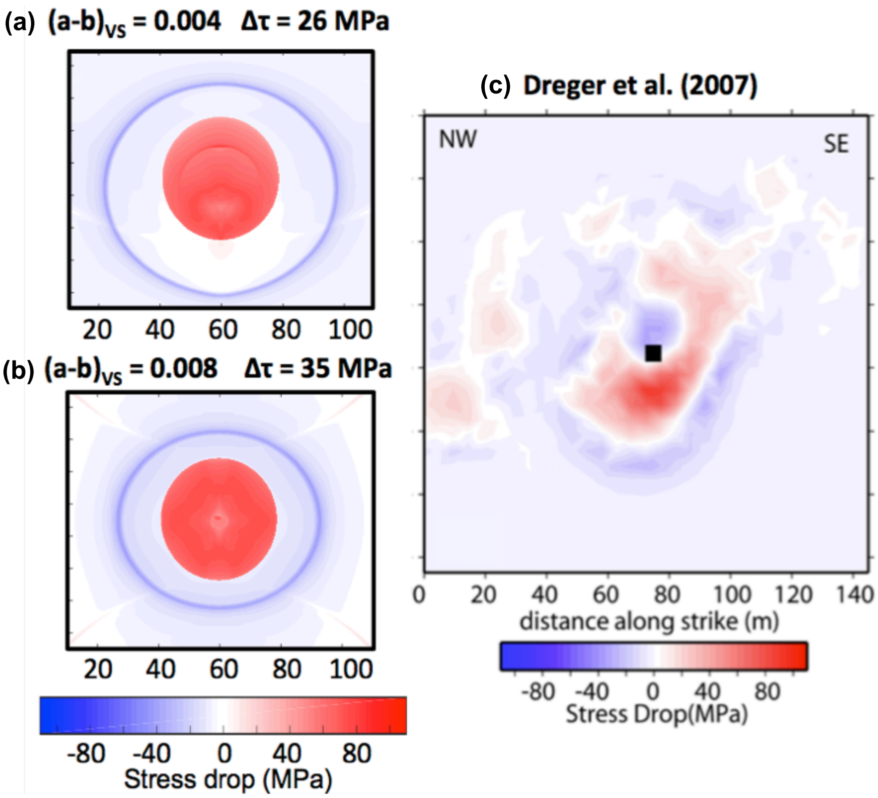

Figure 5.18: *Frictional properties of the creeping region affect the average stress drop of the repeating sources.* (a-b) Spatial distribution of stress change of a patch on a fault with $(a-b)_{\mathrm{VS}}$ = 0.004 and 0.008, respectively. Area with positive stress change (red circle) indicates the VW area. Maximum stress change on the patch reaches 80 MPa. Outside of that, stress change ranges from negative to neutral. The purple ring delineates the actual ruptured area. Event in (b) has higher average stress drop due to a smaller ruptured area. (c) Figure from Dreger et al. (2007): Inferred distribution of stress change in the SF source region. The SF event has similar maximum stress drop in the source region compared to our simulation results.

reproduce the relatively high inferred stress drops of these repeaters (~30 MPa), which correspond to patch sizes consistent with the high degree of interaction of the SF and LA repeaters without overlapping of their sources. To that end, we augment the standard rate-and-state model for the repeaters of Chen and Lapusta, (2009) in two ways: by adding enhanced coseismic weakening in the form of thermal pressurization of pore fluids to the VW patch (M1) and by imposing locally elevated normal stress on the VW patch (M2). We find that both models can reasonably closely reproduce the source properties of the SF and LA repeaters, including the inferred relatively high stress drops, moment magnitude, recurrence interval, and triggering time of the interaction.

Note that the observed average recurrence time and seismic moment of the SF and LA repeaters suggest that a significant fraction of slip at the location of the repeating earthquakes occurs aseismically, as otherwise their stress drop would be unphysically large, ~300 MPa. That is why, in our models, the size of the patches that nucleate the repeaters are chosen to be close to the nucleation size, and the models, as expected, result in significant fraction of aseismic slip on the patches (from ~20-40% in M1 to ~70-80% in M2). Furthermore, both models M1 and M2 reproduce the observed $T_\mathrm{r} \propto M_\mathrm{o}^{1.6}$ scaling of the larger collection of Parkfield repeaters, when events of different moment magnitudes are produced in our models by varying the patch size. In our models, the scaling results are due to the changing fraction of aseismic slip on the VW patches, similar to the study of the standard rate-and-state models of Chen and Lapusta 2009.

While both models M1 and M2 reasonably match the targeted observations, they have important differences. In model M1 with enhanced co-seismic weakening, the stress drop on the VW patches is a substantial fraction, close to 100%, of the representative low-rate fault strength $f_o\bar{\sigma}^o_\mathrm{vw}$, and the average shear stress on the patches are far from that representative low-rate strength for most of the interseismic period between the simulated repeaters. In model M2 with elevated normal stress, the stress drop on the VW patches is similar in the absolute sense but much smaller (10% or so) relative to the representative low-rate fault strength $f_o\bar{\sigma}^o_\mathrm{vw}$ due to much higher $\bar{\sigma}^o_\mathrm{vw}$. Therefore, in a relative sense, the average shear stress on the VW patches is close to the representative low-rate strength for most of the interseismic period between the simulated repeaters. As the result of this difference, model M2 with elevated normal stress has a substantially higher fraction of aseismic slip, for the same patch-to-h* ratio. Furthermore, in model M2, additional smaller seismic events and/or aseismic transients occur on the patch in the interseismic period, on top of the main repeating events.

Interestingly, even in these relatively simple models with uniform properties within each VW patch as well as outside the patches, the recurrence time of the repeaters and their moment exhibit substantial variability, as observed for the actual repeating sequences. This variability is mainly due to varying pre-, post-, and inter-seismic slip, largely aseismic. As the result of this slip between repeaters, the simulated main repeaters exhibit counter-intuitive properties, such as a smaller or unchanged moment magnitude after a longer time period since the previous event. The existence of such aseismic slip explains why Parkfield repeaters are neither time-predictable nor slip predictable, in the sense that they are better matched by the constant recurrence time (Rubinstein et al., 2012) despite significant variability. This is because the notions of the time or slip predictability are based on the assumption that the inter-event time is controlled by the properties of the seismic events themselves, whereas our models show that the inter-event time of the repeaters is significantly influenced by the pre-, post-, and inter-seismic processes.

We find that the properties of the VS region surrounding the repeaters significantly affect the properties of the repeaters themselves, including their average stress drop and seismic moment, since dynamic rupture significantly penetrates from the VW patch into the VS surroundings. The extent of that penetration can add to the seismic moment as well as significantly affect the source dimension and hence the inferred duration and stress drop. Furthermore, the postseismic slip in the VS region between the SF and LA repeaters controls their interaction, as suggested by the simplified 2D study in Chapter 4. For the assumed properties of the VW patches that match the repeaters reasonably well and effective normal stress of 120 MPa, our modeling suggests that the VS region has the rate-and-state property $(a-b)_{\mathrm{VS}}$ in the range of 0.004 to 0.008. This is consistent with other studies in the area (Barbot et al., 2009; Chang et al., 2013).

While some parameters used in this work are well-constrained, many are less certain, and some are simply assumed to explore representative models, as detailed in the previous sections. Additional observations and laboratory constraints are needed to narrow the parameter space of the potential models and identify the most plausible ones. For example, if the effective normal stress is more or less homogeneous in the interseismic period on the scale of several hundred meters, as postulated in M1, then the assumed 120 MPa is a well-constained value based on the SAFOD drilling site (e.g., Lockner et al., 2011). However, the value of 600 MPa in M2 is simply assumed to achieve suitable stress drops in a standard rate-and-state model, in order to study the consequences of such a model. One important question, which is outside the scope of this work, is whether such high effective stresses are physically plausible. However, such high effective stresses may not be needed, since the observed stress drops and other properties can likely be reproduced by a number of models that are in between models M1 and M2, combining some enhanced co-seismic weakening with a more modest increase in the interseismic effective normal stress. We have presented an example of such a model, M3. However, we have focused on the end-member models to identify their similarities and differences; the in-between models are likely to have properties in-between. More detailed exploration of the M3-type combined models would be most useful with more constraints on the stress, poroelastic, and fault properties in the area.

Such constrains can be obtained from drilling through the sources of the SF or LA repeaters, as was intended in the SAFOD project. The drilling may lead to detection of interseismic slip which is an important component of the models presented here, measurements of the stress conditions at the source of repeaters, as well as constraints on a number of other model parameters, such as permeability and shear zone width. Unfortunately, the small aseismic slips observed on the patches in our models, which are of the order of centimeters over patches of the order of tens of meters, cannot be resolved from the surface GPS and strain meter measurements, given the 2.5 km depth of the repeaters.

Despite the uncertainty in fault properties, our study has uncovered a number of robust conclusions. We find that additional factors, on top of the standard rate-and-state friction, are needed to explain the specific observations for the SF and LA repeaters. Both enhanced coseismic weakening and elevated normal stress on the repeater-producing VW patches result in plausible models for the repeaters and their interaction, and these factors may act in combination. Our exploration of the end-member models finds that all considered models are characterized by the occurrence of substantial and variable aseismic slip on the VW patches. This aseismic slip cannot be inferred from the surface observations but, based on our models, it is key to explaining the observed behavior of these repeaters, including variability in their source properties, their sometimes irregular interactions, their atypical T_r-M_o relation, and the fact that they are neither slip nor time-predictable.

5.6 References

Abercrombie, Rachel E. (1995). “Earthquake source scaling relationships from -1 to 5 ML using seismograms recorded at 2.5-km depth”. In: *Journal of Geophysical Research: Solid Earth* 100.B12, pp. 24015–24036. ISSN: 2156-2202. DOI: `10.1029/95JB02397`. URL: `http://dx.doi.org/10.1029/95JB02397`.

– (2014). “Stress drops of repeating earthquakes on the San Andreas Fault at Parkfield”. In: *Geophysical Research Letters* 41.24. 2014GL062079, pp. 8784–8791. ISSN: 1944-8007. DOI: `10.1002/2014GL062079`. URL: `http://dx.doi.org/10.1002/2014GL062079`.

Anooshehpoor, Abdolrasool and James N Brune (2001). “Quasi-static slip-rate shielding by locked and creeping zones as an explanation for small repeating earthquakes at Parkfield”. In: *Bulletin of the Seismological Society of America* 91.2, pp. 401–403. DOI: `10.1785/0120000105`. URL: `http://dx.doi.org/10.1785/0120000105`.

Bakun, WH et al. (2005). “Implications for prediction and hazard assessment from the 2004 Parkfield earthquake”. In: *Nature* 437.7061, pp. 969–974. DOI: `10.1038/nature04067`. URL: `http://dx.doi.org/10.1038/nature04067`.

Bakun, William H. and Thomas V. McEvilly (1984). “Recurrence models and Parkfield, California, earthquakes”. In: *Journal of Geophysical Research: Solid Earth* 89.B5, pp. 3051–3058. ISSN: 2156-2202. DOI: `10.1029/JB089iB05p03051`. URL: `http://dx.doi.org/10.1029/JB089iB05p03051`.

Barbot, Sylvain, Yuri Fialko, and Yehuda Bock (2009). “Postseismic deformation due to the Mw 6.0 2004 Parkfield earthquake: Stress-driven creep on a fault with spatially variable rate-and-state friction parameters”. In: *Journal of Geophysical Research: Solid Earth* 114.B7. B07405, n/a–n/a. ISSN: 2156-2202. DOI: `10.1029/2008JB005748`. URL: `http://dx.doi.org/10.1029/2008JB005748`.

Barbot, Sylvain, Nadia Lapusta, and Jean-Philippe Avouac (2012). “Under the hood of the earthquake machine: Toward predictive modeling of the seismic cycle”. In: *Science* 336.6082, pp. 707–710. DOI: `10.1126/science.1218796`. URL: `http://dx.doi.org/10.1126/science.1218796`.

Beeler, NM, DL Lockner, and SH Hickman (2001). “A simple stick-slip and creep-slip model for repeating earthquakes and its implication for microearthquakes at Parkfield”. In: *Bulletin of the Seismological Society of America* 91.6, pp. 1797–1804. DOI: `10.1785/0120000096`. URL: `http://dx.doi.org/10.1785/0120000096`.

Ben-Zion, Yehuda and James R. Rice (1997). “Dynamic simulations of slip on a smooth fault in an elastic solid”. In: *Journal of Geophysical Research: Solid Earth* 102.B8, pp. 17771–17784. ISSN: 2156-2202. DOI: `10.1029/97JB01341`. URL: `http://dx.doi.org/10.1029/97JB01341`.

Blanpied, ML, DA Lockner, and JD Byerlee (1991). “Fault stability inferred from granite sliding experiments at hydrothermal conditions”. In: *Geophysical Research Letters* 18.4, pp. 609–612.

Brune, James N. (1970). “Tectonic stress and the spectra of seismic shear waves from earthquakes”. In: *Journal of Geophysical Research* 75.26, pp. 4997–5009. ISSN: 2156-2202. DOI: `10.1029/JB075i026p04997`. URL: `http://dx.doi.org/10.1029/JB075i026p04997`.

Chang, Shu-Hao, Jean-Philippe Avouac, Sylvain Barbot, and Jian-Cheng Lee (2013). “Spatially variable fault friction derived from dynamic modeling of aseismic afterslip due to the 2004 Parkfield earthquake”. In: *Journal of Geophysical Research: Solid Earth* 118.7, pp. 3431–3447. ISSN: 2169-9356. DOI: `10.1002/jgrb.50231`. URL: `http://dx.doi.org/10.1002/jgrb.50231`.

Chen, Ting and Nadia Lapusta (2009). “Scaling of small repeating earthquakes explained by interaction of seismic and aseismic slip in a rate and state fault model”. In: *Journal of Geophysical Research: Solid Earth* 114.B1. B01311, n/a–n/a. ISSN: 2156-2202. DOI: `10.1029/2008JB005749`. URL: `http://dx.doi.org/10.1029/2008JB005749`.

Deng, Jishu, Kenneth Hudnut, Michael Gurnis, and Egill Hauksson (1999). “Stress loading from viscous flow in the lower crust and triggering of aftershocks following the 1994 Northridge California, earthquake”. In: *Geophysical Research Letters* 26.21, pp. 3209–3212. DOI: `10.1029/1999GL010496`. URL: `http://dx.doi.org/10.1029/1999GL010496`.

Dieterich, James (1994). “A constitutive law for rate of earthquake production and its application to earthquake clustering”. In: *Journal of Geophysical Research: Solid Earth* 99.B2, pp. 2601–2618. ISSN: 2156-2202. DOI: `10.1029/93JB02581`. URL: `http://dx.doi.org/10.1029/93JB02581`.

Dieterich, James H. (1979). “Modeling of rock friction: 1. Experimental results and constitutive equations”. In: *Journal of Geophysical Research: Solid Earth* 84.B5, pp. 2161–2168. ISSN: 2156-2202. DOI: `10.1029/JB084iB05p02161`. URL: `http://dx.doi.org/10.1029/JB084iB05p02161`.

Dieterich, James H (1981). “Constitutive properties of faults with simulated gouge”. In: *Mechanical behavior of crustal rocks: the Handin volume*, pp. 103–120. DOI: `10.1029/GM024p0103`. URL: `http://dx.doi.org/10.1029/GM024p0103`.

– (1992). “Earthquake nucleation on faults with rate-and state-dependent strength”. In: *Tectonophysics* 211.1-4, pp. 115–134. DOI: `10.1016/0040-1951(92)90055-B`. URL: `http://dx.doi.org/10.1016/0040-1951(92)90055-B`.

Dieterich, JH (2007). “Applications of rate-and state-dependent friction to models of fault slip and earthquake occurrence”. In: *Treatise on Geophysics* 4, pp. 107–129.

Dreger, Douglas, Robert M Nadeau, and Angela Chung (2007). "Repeating earthquake finite source models: Strong asperities revealed on the San Andreas Fault". In: *Geophysical Research Letters* 34.23. DOI: `10.1029/2007GL031353`. URL: `http://dx.doi.org/10.1029/2007GL031353`.

Eshelby, John D (1957). "The determination of the elastic field of an ellipsoidal inclusion, and related problems". In: *Proceedings of the Royal Society of London A: Mathematical, Physical and Engineering Sciences*. Vol. 241. 1226. The Royal Society, pp. 376–396. DOI: `10.1098/rspa.1957.0133`. URL: `http://dx.doi.org/10.1098/rspa.1957.0133`.

Freed, Andrew M and Jian Lin (2001). "Delayed triggering of the 1999 Hector Mine earthquake by viscoelastic stress transfer". In: *Nature* 411.6834, pp. 180–183. DOI: `10.1038/35075548`. URL: `http://dx.doi.org/10.1038/35075548`.

Gomberg, J., N. M. Beeler, M. L. Blanpied, and P. Bodin (1998). "Earthquake triggering by transient and static deformations". In: *Journal of Geophysical Research: Solid Earth* 103.B10, pp. 24411–24426. ISSN: 2156-2202. DOI: `10.1029/98JB01125`. URL: `http://dx.doi.org/10.1029/98JB01125`.

Gomberg, J, PA Reasenberg, P Bodin, and RA Harris (2001). "Earthquake triggering by seismic waves following the Landers and Hector Mine earthquakes". In: *Nature* 411.6836, pp. 462–466. DOI: `10.1038/35078053`. URL: `http://dx.doi.org/10.1038/35078053`.

Hill, DP et al. (1993). "Seismicity remotely triggered by the magnitude 7.3 Landers, California, earthquake". In: *Science* 260.5114, pp. 1617–1623. DOI: `10.1126/science.260.5114.1617`. URL: `http://dx.doi.org/10.1126/science.260.5114.1617`.

Hsu, Ya-Ju et al. (2006). "Frictional afterslip following the 2005 Nias-Simeulue earthquake, Sumatra". In: *Science* 312.5782, pp. 1921–1926. DOI: `10.1126/science.1126960`. URL: `http://dx.doi.org/10.1126/science.1126960`.

Jiang, Junle and Nadia Lapusta (2016). "Deeper penetration of large earthquakes on seismically quiescent faults". In: *Science* 352.6291, pp. 1293–1297. DOI: `10.1126/science.aaf1496`. URL: `http://dx.doi.org/10.1126/science.aaf1496`.

Johanson, I. A. and R. Bürgmann (2010). "Coseismic and postseismic slip from the 2003 San Simeon earthquake and their effects on backthrust slip and the 2004 Parkfield earthquake". In: *Journal of Geophysical Research: Solid Earth* 115.B7. B07411, n/a–n/a. ISSN: 2156-2202. DOI: `10.1029/2009JB006599`. URL: `http://dx.doi.org/10.1029/2009JB006599`.

Kilb, Deborah, Joan Gomberg, and Paul Bodin (2000). "Triggering of earthquake aftershocks by dynamic stresses". In: *Nature* 408.6812, pp. 570–574. DOI: `10.1038/35046046`. URL: `http://dx.doi.org/10.1038/35046046`.

Lachenbruch, Arthur H. (1980). “Frictional heating, fluid pressure, and the resistance to fault motion”. In: *Journal of Geophysical Research: Solid Earth* 85.B11, pp. 6097–6112. ISSN: 2156-2202. DOI: `10.1029/JB085iB11p06097`. URL: `http://dx.doi.org/10.1029/JB085iB11p06097`.

Lapusta, Nadia and Yi Liu (2009). “Three-dimensional boundary integral modeling of spontaneous earthquake sequences and aseismic slip”. In: *Journal of Geophysical Research: Solid Earth* 114.B9. DOI: `10.1029/2008JB005934`. URL: `http://dx.doi.org/10.1029/2008JB005934`.

Lapusta, Nadia and James R. Rice (2003). “Nucleation and early seismic propagation of small and large events in a crustal earthquake model”. In: *Journal of Geophysical Research: Solid Earth* 108.B4. 2205, n/a–n/a. ISSN: 2156-2202. DOI: `10.1029/2001JB000793`. URL: `http://dx.doi.org/10.1029/2001JB000793`.

Lapusta, Nadia, James R Rice, and Gutuan Zheng (2000). “Elastodynamic analysis for slow tectonic loading with spontaneous rupture episodes on faults with rate- and state-dependent friction”. In: *JOURNAL OF GEOPHYSICAL RESEARCH* 105.B10, pp. 23765–23789.

Lisowski, Michael and WH Prescott (1981). “Short-range distance measurements along the San Andreas fault system in central California, 1975 to 1979”. In: *Bulletin of the Seismological Society of America* 71.5, pp. 1607–1624.

Liu, Yajing and James R. Rice (2005). “Aseismic slip transients emerge spontaneously in three-dimensional rate and state modeling of subduction earthquake sequences”. In: *Journal of Geophysical Research: Solid Earth* 110.B8. B08307, n/a–n/a. ISSN: 2156-2202. DOI: `10.1029/2004JB003424`. URL: `http://dx.doi.org/10.1029/2004JB003424`.

Lockner, David A, Carolyn Morrow, Diane Moore, and Stephen Hickman (2011). “Low strength of deep San Andreas fault gouge from SAFOD core”. In: *Nature* 472.7341, pp. 82–85. DOI: `10.1038/nature09927`. URL: `http://dx.doi.org/10.1038/nature09927`.

Lui, Semechah KY, Don Helmberger, Junjie Yu, and Shengji Wei (2016). “Rapid Assessment of Earthquake Source Characteristics”. In: *Bulletin of the Seismological Society of America* 106.6, in press. DOI: `10.1785/0120160112`. URL: `http://dx.doi.org/10.1785/0120160112`.

Madariaga, Raul (1976). “Dynamics of an expanding circular fault”. In: *Bulletin of the Seismological Society of America* 66.3, pp. 639–666.

Marone, Chris (1998). “Laboratory-derived friction laws and their application to seismic faulting”. In: *Annual Review of Earth and Planetary Sciences* 26.1, pp. 643–696. DOI: `10.1146/annurev.earth.26.1.643`. URL: `http://dx.doi.org/10.1146/annurev.earth.26.1.643`.

McLaskey, Gregory C. and Brian D. Kilgore (2013). “Foreshocks during the nucleation of stick-slip instability”. In: *Journal of Geophysical Research: Solid Earth* 118.6, pp. 2982–2997. ISSN: 2169-9356. DOI: `10.1002/jgrb.50232`. URL: `http://dx.doi.org/10.1002/jgrb.50232`.

Miyazaki, Shin’ichi, Paul Segall, Jeffery J. McGuire, Teruyuki Kato, and Yuki Hatanaka (2006). “Spatial and temporal evolution of stress and slip rate during the 2000 Tokai slow earthquake”. In: *Journal of Geophysical Research: Solid Earth* 111.B3. B03409, n/a–n/a. ISSN: 2156-2202. DOI: `10.1029/2004JB003426`. URL: `http://dx.doi.org/10.1029/2004JB003426`.

Murray, J. R., P. Segall, P. Cervelli, W. Prescott, and J. Svarc (2001). “Inversion of GPS data for spatially variable slip-rate on the San Andreas Fault near Parkfield, CA”. In: *Geophysical Research Letters* 28.2, pp. 359–362. ISSN: 1944-8007. DOI: `10.1029/2000GL011933`. URL: `http://dx.doi.org/10.1029/2000GL011933`.

Nadeau, Robert M and Lane R Johnson (1998). “Seismological studies at Parkfield VI: Moment release rates and estimates of source parameters for small repeating earthquakes”. In: *Bulletin of the Seismological Society of America* 88.3, pp. 790–814.

Nadeau, Robert M, Alberto Michelini, Robert A Uhrhammer, David Dolenc, and Thomas V McEvilly (2004). “Detailed kinematics, structure and recurrence of micro-seismicity in the SAFOD target region”. In: *Geophysical Research Letters* 31.12. L12S08, n/a–n/a. ISSN: 1944-8007. DOI: `10.1029/2003GL019409`. URL: `http://dx.doi.org/10.1029/2003GL019409`.

Noda, Hiroyuki and Nadia Lapusta (2010). “Three-dimensional earthquake sequence simulations with evolving temperature and pore pressure due to shear heating: Effect of heterogeneous hydraulic diffusivity”. In: *Journal of Geophysical Research: Solid Earth* 115.B12. B12314, n/a–n/a. ISSN: 2156-2202. DOI: `10.1029/2010JB007780`. URL: `http://dx.doi.org/10.1029/2010JB007780`.

Nur, Amos and John R Booker (1972). “Aftershocks caused by pore fluid flow?” In: *Science* 175.4024, pp. 885–887. DOI: `10.1126/science.175.4024.885`. URL: `http://dx.doi.org/10.1126/science.175.4024.885`.

Perfettini, H. and J.-P. Avouac (2004). “Postseismic relaxation driven by brittle creep: A possible mechanism to reconcile geodetic measurements and the decay rate of aftershocks, application to the Chi-Chi earthquake, Taiwan”. In: *Journal of Geophysical Research: Solid Earth* 109.B2. B02304, n/a–n/a. ISSN: 2156-2202. DOI: `10.1029/2003JB002488`. URL: `http://dx.doi.org/10.1029/2003JB002488`.

Perfettini, H, J Schmittbuhl, and A Cochard (2003). “Shear and normal load perturbations on a two-dimensional continuous fault: 2. Dynamic triggering”. In: *Journal of Geophysical Research: Solid Earth* 108.B9. DOI: `10.1029/2002JB001805`. URL: `http://dx.doi.org/10.1029/2002JB001805`.

Rice, James R. (2006). “Heating and weakening of faults during earthquake slip”. In: *Journal of Geophysical Research: Solid Earth* 111.B5. B05311, n/a–n/a. ISSN: 2156-2202. DOI: `10.1029/2005JB004006`. URL: `http://dx.doi.org/10.1029/2005JB004006`.

Rice, James R, Nadia Lapusta, and K Ranjith (2001). “Rate and state dependent friction and the stability of sliding between elastically deformable solids”. In: *Journal of the Mechanics and Physics of Solids* 49.9, pp. 1865–1898. DOI: `10.1016/S0022-5096(01)00042-4`. URL: `http://dx.doi.org/10.1016/S0022-5096(01)00042-4`.

Rice, JR and AL Ruina (1983). “Stability of steady frictional slipping”. In: *Journal of applied mechanics* 50.2, pp. 343–349. DOI: `10.1115/1.3167042`. URL: `http://dx.doi.org/10.1115/1.3167042`.

Rubin, AM and J-P Ampuero (2005). “Earthquake nucleation on (aging) rate and state faults”. In: *Journal of Geophysical Research: Solid Earth* 110.B11. DOI: `10.1029/2005JB003686`. URL: `http://dx.doi.org/10.1029/2005JB003686`.

Rubinstein, Justin L., William L. Ellsworth, Kate H. Chen, and Naoki Uchida (2012). “Fixed recurrence and slip models better predict earthquake behavior than the time- and slip-predictable models: 1. Repeating earthquakes”. In: *Journal of Geophysical Research: Solid Earth* 117.B2. B02306, n/a–n/a. ISSN: 2156-2202. DOI: `10.1029/2011JB008724`. URL: `http://dx.doi.org/10.1029/2011JB008724`.

Ruina, Andy (1983). “Slip instability and state variable friction laws”. In: *Journal of Geophysical Research: Solid Earth* 88.B12, pp. 10359–10370. ISSN: 2156-2202. DOI: `10.1029/JB088iB12p10359`. URL: `http://dx.doi.org/10.1029/JB088iB12p10359`.

Sammis, Charles G., Robert M. Nadeau, and Lane R. Johnson (1999). “How strong is an asperity?” In: *Journal of Geophysical Research: Solid Earth* 104.B5, pp. 10609–10619. ISSN: 2156-2202. DOI: `10.1029/1999JB900006`. URL: `http://dx.doi.org/10.1029/1999JB900006`.

Titus, Sarah J, Charles DeMets, and Basil Tikoff (2006). “Thirty-five-year creep rates for the creeping segment of the San Andreas fault and the effects of the 2004 Parkfield earthquake: Constraints from alignment arrays, continuous global positioning system, and creepmeters”. In: *Bulletin of the Seismological Society of America* 96.4B, S250–S268. DOI: `10.1785/0120050811`. URL: `http://dx.doi.org/10.1785/0120050811`.

Tullis, Terry E (1996). “Rock friction and its implications for earthquake prediction examined via models of Parkfield earthquakes”. In: *Proceedings of the National Academy of Sciences* 93.9, pp. 3803–3810.

Waldhauser, F., W. L. Ellsworth, D. P. Schaff, and A. Cole (2004). “Streaks, multiplets, and holes: High-resolution spatio-temporal behavior of Parkfield seismicity”. In: *Geophysical Research Letters* 31.18. L18608, n/a–n/a. ISSN: 1944-

8007. DOI: `10.1029/2004GL020649`. URL: `http://dx.doi.org/10.1029/2004GL020649`.

Zoback, Mark, Stephen Hickman, William Ellsworth, et al. (2011). "Scientific drilling into the San Andreas Fault Zone—An overview of SAFOD's first five years". In: *Sci. Drill* 11.1, pp. 14–28. DOI: `10.2204/iodp.sd.11.02.2011`. URL: `http://dx.doi.org/10.2204/iodp.sd.11.02.2011`.

Chapter 6

CONCLUSION

In this thesis, we explore the wealth of information hosted by small to moderate sized earthquakes based on seismic observations and dynamic rupture simulations. Through characterizing the source properties, rupture processes and the physical mechanisms of these earthquakes, we investigate their various implications on topics such as impact of larger earthquakes, local tectonic features, and fault frictional properties, as well as the potential practical applications to hazard mitigation assessment.

6.1 Summary

Part I consists of two observational studies involving the modeling of seismic waves. We discuss in Chapter 2 the source characterization of a group of intraslab events that occurred beneath the rupture region of the 2011 M_w 9.1 Tohoku-Oki earthquake. With the forward modeling of the empirical Green's functions, we are able to constrain the true rupture plane and delineate a long subducted normal fault that is believed to have reactivated after the main shock. The focal mechanisms of these thrust events also agree with the modeled Coulomb stress change from the main shock. Detailed modeling of smaller events in the region helps construct a clearer image of the subduction zone, such as the geometry of the slab, the faults inside it and the heterogeneity of the stress distribution on the fault. These findings are helpful in developing a better understanding of the major earthquakes from the past and in the future, bringing us closer to finding definitive explanations to some of the intriguing phenomena, such as the unique energy radiation patterns of the 2011 M_w 9.1 Tohoku-Oki earthquake.

Building on Chapter 2, we also made progress in developing a framework for the fast characterization of earthquake sources, which can potentially be applied in earthquake early warning systems. Our work in Chapter 3 shows that as an earthquake happens, important parameters such as moment magnitude, focal mechanism and focal depth can be constrained within ten seconds of the incoming P-waves arrivals. Similar to the approach in Chapter 2, directivity of a moderate event can be constrained with as little as the first 3 seconds of the P wave. Furthermore, we show that small events can be used to predict the ground motion of large potential earthquakes in the area. While smaller events may not pose high risk of damage themselves, they are certainly useful tools in hazard assessment.

In addition to investigating the source characteristics of small earthquakes, we also study their physical mechanisms. In Part II, we study the physical mechanisms that drive some of these earthquakes by modeling their behaviors in dynamic rupture simulations. In Chapter 4, we study earthquake triggering between two generic repeating earthquake sequences. Results indicate that stress change from postseismic slip is the dominating factor causing the interactions, instead of stress change caused by coseismic slip. Our findings introduce the possibility to constrain frictional properties of the fault based on earthquake interactions. Extending from this, in Chapter 5, we model the source properties and interactions of two actual repeating microearthquake sequences in Parkfield. We find that, for a fault model governed by the rate-and-state friction, additional factors such as dynamic weakening and locally elevated normal stress can explain the observed high stress drops of these repeaters and their synchronized seismic pattern. Results show that the occurrence of substantial and variable aseismic slip on the velocity-weakening patches is key to explaining the variability of the source properties and the interactions of these repeaters, as well as their observed T_r-M_o scaling and the long recurrence interval.

6.2 Outlook

Our work highlights the mutual benefits of integrating observations with dynamic simulations in studying earthquakes. Accurate constraints of observed sources can translate into realistic model parameters in dynamic simulations. In return, physics-based dynamic simulations allow us to rule out any non-physical inferences from observations and serve as potential tools in predicting future earthquakes. Continuous advancement and integration of research techniques and tools will allow us to keep asking important questions and finding answers. Here are some possible avenues of future work extending from this thesis:

6.2.1 Implications on earthquake scaling

In Chapter 3, we propose the possibility of building an empirical Green's function library with existing small to moderate events and calculating the effects of future big events ahead of their occurrence. Nonetheless, earthquake rupture is known to increase in complexity with earthquake magnitude and further exploration on the scalability of earthquake rupture processes is needed in order to determine the key factors in the parametrization of large earthquake modeling. To this end, one can combine both deterministic and empirical approaches to generate Green's functions.

6.2.2 Spatiotemporal heterogeneity of fault properties

Since complex rupture patterns have been observed for some of the earthquakes occurring on the active Parkfield segment, its fault properties are believed to vary spatially and potentially be evolving over time. In order to better understand the origin of the observed seismicity and the variability in seismic sources, further work can be done to construct fault models with different degrees of spatiotemporal heterogeneity in frictional properties and stress distribution. Eventually, we can also extend our work to developing models of more complex fault systems and to studying the intricate interaction among neighboring faults.